TÉCNICO LISBOA

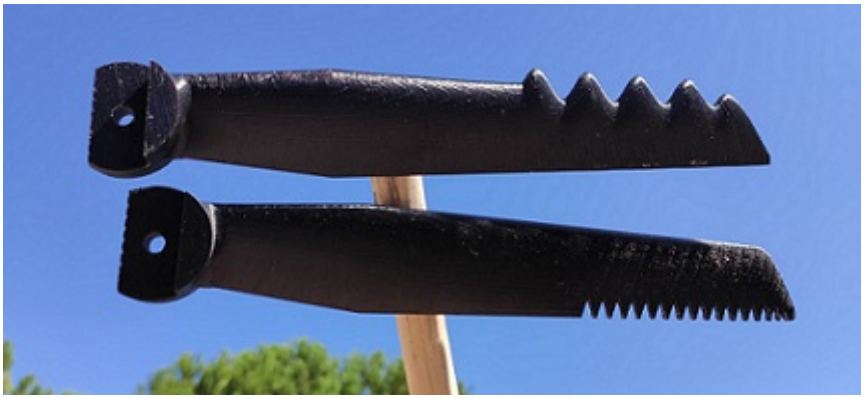

Novel concepts for noise mitigation of small UAV rotors

Pedro Miguel de Barros e Silva Duarte

Thesis to obtain the Master of Science Degree in

Aerospace Engineering

Supervisors: Prof. João Manuel Gonçalves de Sousa Oliveira
Prof. Filipe Szolnoky Ramos Pinto Cunha

Examination Committee

Chairperson: Prof. Fernando José Parracho Lau
Supervisor: Prof. João Manuel Gonçalves de Sousa Oliveira
Member of the Committee: Prof. António Manuel Relógio Ribeiro

October 2020

Acknowledgments

First, I would like to thank my supervisors, Professor Filipe Cunha and Professor João Oliveira for their guidance and support that have made possible the conclusion of this Thesis. I would also like to express my gratitude to Professor Relógio Ribeiro and to Nuno Frutuoso who have helped me immensely with the printing of the blades. Also, I would like to thank Professor Agostinho Fonseca for his advice and support concerning the experimental setup.

To my family and friends, an enormous thank you for keeping my spirits up and focused, not to mention all the occasional joyful distractions that were well worth it.

Lastly, to my brother, who I did not get to be with for months because he was fighting the pandemic, but still always made time to check on my progress and listen to my rants about the most insignificant subjects - Thank you.

Abstract

The objective was to study the noise produced by a small UAV rotor in hover conditions and achieve noise reductions by implementing leading edge and trailing edge modifications. Using additive manufacturing, three leading edge modified rotors and three trailing edge serrated rotors were constructed and then experimentally tested against a baseline. The tests were conducted in the anechoic chamber of the Aeroacoustic Tunnel of Instituto Superior Técnico.

The trailing edge serrations were confirmed to reduce consistently the high frequency noise. Considering the overall noise, the reductions achieved depended on the operating rotation speed. However, this type of serrations showed to degrade the aerodynamic performance of the rotors, generating less thrust and requiring more power than the baseline.

The sinusoidal leading edges implemented proved to be effective in reducing the noise for the frequencies to which the human hearing is most sensitive to. Furthermore, they also showed small reductions in the high frequency noise, although not as much as the trailing edge serrations. These rotors presented either small losses to the aerodynamic performance or, in the case of one of the rotors, an increase in the generated thrust and in the figure of merit.

Keywords

Rotor noise; Blade serrations; Trailing edge serrations; Leading edge modifications.

Resumo

O objectivo passa por estudar o ruído produzido por um rotor duma pequena aeronave não tripulada, a pairar, e conseguir reduzir esse ruído ao implementar modificações no bordo de ataque e no bordo de fuga. Usando manufatura aditiva, foram construídos três rotores com o bordo de ataque modificado e outros três rotores com o bordo de fuga serrilhado, que foram ensaiados experimentalmente e comparados a um modelo de base. Os ensaios ocorreram na câmara anecóica do Túnel Aeroacústico do Instituto Superior Técnico.

Confirmou-se que o bordo de fuga serrilhado reduz o ruído a elevadas frequências consistentemente. Em termos gerais, a redução do ruído por parte destes rotores depende da velocidade de rotação. Contudo, este tipo de modificação mostrou degradar o desempenho aerodinâmico dos rotores, gerando uma força propulsiva menor e necessitando de mais energia que o modelo de base.

Os bordos de ataque sinusoidais implementados provaram ser eficazes na redução do ruído para o intervalo de frequências onde a audição humana é mais sensível. Para além disso, obtiveram também pequenas reduções no ruído de alta frequência, ainda que menores que as reduções obtidas com os bordos de fuga serrilhados. Os rotores com o bordo de ataque modificado apresentaram pequenas perdas no desempenho aerodinâmico, tendo havido ainda o caso de um dos rotores que apresentou um aumento na força propulsiva e na eficiência.

Palavras Chave

Ruído de rotores; Pás modificadas; Bordo de fuga serrilhado; Bordo de ataque modificado.

Contents

List of Figures

List of Tables

Nomenclature

Greek Symbols

α	Angle of attack
Δl	Moment arm
δ	Boundary layer thickness
ϵ_i	Estimated calibration error
Λ	Turbulence integral length-scale
λ	Serration wavelength
Ω	Rotation speed
ϕ	Inflow angle
ρ	Density
σ	Rotor solidity
σ_i	Standard deviation of the fitting
σ_{tot_i}	Total uncertainty
θ	Serration inclination angle
ϑ	pitch angle

Roman Symbols

A	Rotor area
a	Flat tip width
A_p	Blade planform area

$B1$ Full bending bridge for F_x measurement

$B2$ Full bending bridge for M_x measurement

$B3$ Auxiliary full bending bridge for M_x measurement

c Chord

$\boldsymbol{C}'$ First iteration calibration coefficients matrix

$\boldsymbol{C}_1$, $\boldsymbol{C}_2$ and $\boldsymbol{C}_3$ Calibration coefficients matrix

C_d Aerofoil drag coefficient

C_P Power coefficient

C_T Thrust coefficient

$c_{i,j}$ Calibration coefficients

C_{l_α} Derivative of the aerofoil lift coefficient with the angle of attack

C_l Aerofoil lift coefficient

C_{P_I} Ideal power coefficient

D Drag

$\boldsymbol{D}_1$, $\boldsymbol{D}_2$ and $\boldsymbol{D}_3$ Sensitivity coefficients matrix

dD Drag corresponding to an infinitesimal blade element

dF Elemental force

dL Lift corresponding to an infinitesimal blade element

dP Elemental power

dT Elemental thrust

dy Infinitesimal element width

f Frequency

F_x Axial load component in the XX direction

F_y Transversal load component in the YY direction

FM Figure of merit

h Half of the serration amplitude

h' Effective serration amplitude

$\boldsymbol{I}$ Identity matrix

L Lift

m Number of parameters to be fitted

M_x Moment in the XX direction

M'_x Blade bending moment

M_y Moment in the YY direction

Ma Mach number

N Number of sets in a calibration sequence

n Number of calibration sequences

P Power

p Instantaneous sound pressure

P_I Ideal power

p_{ref} Reference sound pressure

p_{rms} Root mean square sound pressure

Q Torque

R Blade radius

$\boldsymbol{R}$ Difference of voltage bridges output matrix

$\boldsymbol{R}'$ Voltage bridges output matrix

r_0 Hub radius

r_1, r_2, r_3 and r_4 Strain gages resistances in a full bridge configuration

$\boldsymbol{R}_{average}$ Average matrix of the registered voltage bridges outputs from the repetition of the calibration procedure

$\boldsymbol{R}_{global}$ Matrix containing the difference in voltage bridges output of the three calibration sequences

$r_{i,j}$ Difference of voltage bridges output

Re Reynolds number

St_δ Strouhal number based on the boundary layer thickness

St_h Strouhal number based on the serration amplitude

T Thrust

t_f Final counting time instant

t_i Initial counting time instant

U Total velocity

U_0 Upstream flow velocity

U_A Full bridge output voltage

U_E Full bridge excitation voltage

u_i Load uncertainty

u_m Mass uncertainty

U_P Velocity perpendicular to the rotation plane

U_R Radial velocity

U_T Transverse velocity

v_i Induced velocity

$\boldsymbol{V}_R$ Variances and covariances matrix

$\boldsymbol{V}_W$ Uncertainties of the calibration procedure matrix

$\boldsymbol{V}_{\hat{y}_i}$ Matrix of the estimated aerodynamic components uncertainties

$\boldsymbol{V}_{p_i}$ Error matrix

V_{tip} Tip velocity

Vc Climb velocity

$\boldsymbol{W}_1$, $\boldsymbol{W}_2$ and $\boldsymbol{W}_3$ Weighting matrices

$\boldsymbol{Y}$ Matrix of the aerodynamic components F_x, F_y and M_x

$\hat{\boldsymbol{Y}}$ Estimated applied loads matrix

y_i Aerodynamic components F_x, F_y and M_x

$\boldsymbol{Y}_{applied}$ Loading matrix

Subscripts

x, y, z Cartesian components

Superscripts

T Transpose

Acronyms

ABS	Acrylonitrile Butadiene Styrene
AoA	Angle of Attack
BET	Blade Element Theory
BPF	Blade Passing Frequency
DAQ	Data Acquisition
FM	Figure of Merit
IST	Instituto Superior Técnico
IT	Instrumented Tube
LAeq	A-weighted Equivalent Continuous Sound Level
LE	Leading Edge
Leq	Equivalent Continuous Sound Level
OASPL	Overall Sound Pressure Level
PLA	Polylactic Acid
PWL	Sound Power Level
PVA	Polyvinyl Alcohol
RPM	Rotations Per Minute
SG	Strain Gage
SPL	Sound Pressure Level
TE	Trailing Edge
UAV	Unmanned Aerial Vehicle

1

Introduction

Contents

Lately, people all over the world are increasingly more conscious and aware of the impact Man has on the environment. This impact has multiple sources, and it ultimately translates into either air, soil, water or noise pollution. As a result, the scientific community has begun shifting their attention towards this issue. However, solving this pollution problem is a quite slow process, in which it is impossible to completely eliminate the human footprint on the planet, but rather to try to minimize it and preserve Nature in a sustainable way.

Noise pollution is a major topic currently being approached. Any noise source can directly disturb the health quality of those around it. Plus, it can have a negative environmental impact. There are different types of noises, as there are different types of injuries caused by a noise and the exposure to it. Therefore, many studies are performed to ensure the safety, for people and the surrounding environment, of certain machines, workshops, factories and even entire business activities.

Noise is produced by machines, engines and all kinds of devices, and all of these are products of engineering. As such, it is possible to study it and, therefore, improve the technology employed in order to minimize noise emissions. From a new shape to the nozzles used in the motors in civil aviation; or a different shape for the blade tip in helicopter rotors; also the modifications to the trailing edge on a wind turbine blade; these are just a few examples of techniques already in practice to reduce the noise emission levels.

The present study focuses on the noise emissions of a small Unmanned Aerial Vehicle (UAV) rotor, how to reduce it and at what costs to the aerodynamic performance. The small UAV rotor is considered because drones have been increasing its influence on our daily lives, performing more and more tasks. They are usually appreciated for the fact of being unmanned and highly adaptable to different kinds of operations, such as missions that require vertical take-off and landing, to hover, to fly at low altitudes, or to be highly controllable as a multi-rotor configuration.

In this chapter, the primary sources of noise in a rotating blade will be introduced, following with a few examples of modified blades that address these sources. Then, the objectives that are expected to be accomplished in this study will be discussed. Lastly, the thesis outline will be presented.

1.1 Topic Overview - The Aerodynamic Noise

In a modern rotating machine there are two main classes of noises, the mechanical noise and the aerodynamic noise. According to M. F. Barone [1], the mechanical noise is present due to vibrations and gear noise. This class of noise can be attenuated, either by using sound absorbing material or employing techniques to dampen vibrations. However, the class of noise that will be of interest in this study will be the aerodynamic noise, which is predominant over the mechanical noise and more complex.

1.1.1 Aerodynamic noise sources

The aerodynamic noise generated by an aerofoil is divided into two types:

- The turbulent inflow noise;
- The aerofoil self-noise.

The turbulent inflow noise occurs during the interaction between the blade's Leading Edge (LE) with the upstream atmospheric turbulence. In a simplistic way, this noise will be greater the greater the size of the eddies, in the incoming flow, interacting with the blade's LE. Therefore, this noise will depend on the atmospheric conditions and on the flow velocity. Throughout this thesis it is considered a rotor in hovering conditions, a case in which the flow velocity depends only on the rotor rotation speed and on the position on the blade.

The aerofoil self-noise is the noise inherent to the blade itself, hypothetically considering that the blade is rotating in an undisturbed flow. This noise divides into different contributions, the most important ones being the blade tip vortex noise and the Trailing Edge (TE) noise. The first one, as the name suggests, is related with the vortex created at the blade tip, which in turn is affected by the blade tip speed. In design projects of rotors, the blade tip speed is one constraint commonly known, for many years, due to the aerodynamic noise produced. As an effect, tip shapes have been tested for quite some time, addressing the blade tip vortex noise. However, this type of noise will not be in the work scope of this project.

Lastly, there is the TE noise, which is related with the development of the boundary layer over the aerofoil. Summarizing, this noise will be louder when the turbulent boundary layer thickness nearing the TE is higher. As such, the vortical structures trailing from the TE will create more powerful noise sources across the TE. This type of noise source will be one of the main focuses in this thesis due to its relevancy. According to Oerlemans and Schepers [2], who studied the blade noise of a $2.3MW$ wind turbine, the TE noise is the dominant aerofoil self-noise source, indicating that the blade's loudest noise sources were near the tip, but not exactly at the tip. This suggests that, unless the tip speed is considerably high, the blade tip vortex noise is not that relevant. Plus, they concluded that the aerodynamic noise sources were much louder than the mechanical noise sources.

Next, some approaches to reduce the aerodynamic noise, adopted by different authors, will be presented. These approaches will be separated into two groups: the ones focusing on the TE; and the ones that tackle the turbulent inflow noise by modifying the LE.

1.1.2 Approaches to reduce the aerodynamic noise

The aerodynamic noise has been studied for some decades now, at least dating back to the seventies with Amiet [3, 4], when he developed analytical methods for calculating the far field noise produced by

an aerofoil in a subsonic turbulent stream. Amiet even extended his studies by reaching a theoretical method to calculate the TE noise from an aerofoil in an incident turbulent flow. Later, in the late eighties and early nineties, Howe [5,6] analysed analytically the diffraction problem on a flat plate with a serrated TE. Howe also predicted, numerically, the noise reduction levels for different TE serrations and analysed different wavelength-to-amplitude serration ratios, concluding that the optimal attenuation should be obtained with the sawtooth type of serration. Recently, other analytical and numerical studies have been performed, for both LE and TE modifications, as the ones by Sinayoko, Azarpeyvand and Lyu [7,8].

1.1.2.1 Trailing Edge Serrations

The TE modifications tested are usually serrations, that is cuts into the wing or blade itself to achieve a desired shape, for example as a sawtooth or a sinusoidal TE. Concerning serrations, it is generally considered that the serration is periodic, having a wavelength λ and an amplitude $2h$, as it is shown in Figure 1.1, and most of these studies perform a parametric analysis around those two variables.

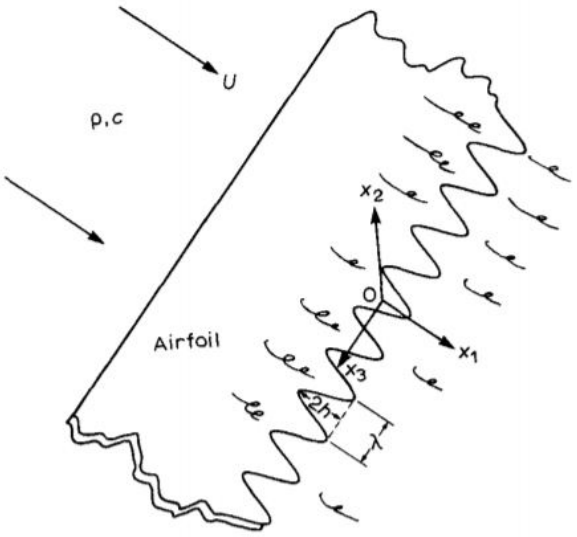

Figure 1.1: Aerofoil with serrated TE. Figure taken from [5].

Gruber [9] tested 30 different serrated TEs on a wing, comparing with Howe's predictions for the noise reductions of a sawtooth TE configuration, and concluded several important notions. The first one states that the noise frequency f up to which there is noise reduction is determined by the Strouhal number $St_\delta = f.\delta/U_0$ based on the boundary layer thickness δ, where U_0 is the upstream flow velocity. For Strouhal numbers $f.\delta/U_0 > 1$ there is a noise increase for the given frequencies, whereas for $f.\delta/U_0 < 1$ the noise is reduced and the level of its reduction depends on the ratios h/δ and h/λ. The second notion is that for $h/\delta < 0.5$, the noise reduction attained is insignificant across the entire frequency range. In this case, the serration amplitude h is clearly shorter than the length of the eddies,

making these pass over the serrations unperturbed just as if there was no TE serration. Finally, it was concluded that the serration amplitude should be greater than the wavelength and that increasing h/λ would increase the noise reduction.

Naturally, each modification has its advantages and disadvantages, which are always related with the level of noise reduction and the aerodynamic performance, meaning that the overall lift and drag are affected. In order to better understand those correlations, experimental studies have been made assessing the boundary layer development on serrated flat plates, such as the one by Moreau and Doolan [10]. They tested the sawtooth TE serration, reaching a $3dB$ reduction on the broadband noise at low frequency and a maximum of $13dB$ at high frequency, stating that noise reduction depends on the boundary layer thickness Strouhal number St_δ and on the serration wavelength. In another study, performed by Chong and Vathylakis [11], the velocity and thermal properties of the turbulent boundary layer on a sawtooth serrated flat plate were investigated. Also, the near field sound waves are characterized using a 34 microphones set-up embedded on the TE, relating it with the flow's thermal behavior.

In an earlier study, Chong *et al.* [12] performed a parametric analysis on the sawtooth serration wavelength-to-amplitude ratio λ/h, on a NACA-0012 aerofoil body, reaching a noise reduction between $2dB$ and $8dB$ in the broadband self-noise. However, the experimental results showed that the serration parameters were not as influential as the existing theory predicted, with a noise increase due to the bluntness near the serration roots. In hopes of reducing the vortex shedding generated near these roots, a woven wire mesh was used, and it indeed lessened the low frequency narrowband as the broadband self-noise, but at the cost of increasing the high frequency noise.

Beyond the typical sawtooth serrations, there are other types of modifications that address the TE noise, such as the poro-serrated profiles, that fill the space cut with a porous material, studied by Vathylakis *et al.* [13] and Chong *et al.* [14]. The typical sawtooth configuration degrades the aerodynamic properties, specially reducing the lift produced. However, with the porous material, a greater part of the lift is restored, and adding to the aeroacoustic component of the noise reduction, the poro-serrated profiles make for an interesting option.

León *et al.* [15–17] investigated the flow topology and the acoustic emissions past a NACA-0018 aerofoil body, with a sawtooth serrated TE attached and functioning as a flap. Using particle image velocimetry, different inclination angles and flap angles were tested, confirming that when the body is aligned with the flow (both angles are null) the mean flow and turbulence statistics do not exhibit significant changes but still achieve considerable noise reduction. However, when the flow is slightly misaligned with the body (by changing the Angle of Attack (AoA) and the flap angle) the flow presents significant changes in its mean values and turbulence statistic measures, resulting in an increase to the noise measured at high frequencies. The correlation between the different flow topology and the increased noise is deepened, concluding that there exists a frequency beyond which the noise level

is found to be higher, and this crossover frequency depends directly on the Strouhal number for the boundary layer thickness and the free stream velocity, which is the same conclusion reached by Gruber.

There are also numerical studies that evaluate the utility of TE serrations, as the one from Avallone *et al.* [18], that compares the far field noise reduction between a sawtooth serration and a curved sawtooth one (shaped like an iron for ironing clothes). The iron-shape presented a $2dB$ reduction in the far field broadband noise compared to the typical sawtooth, for it mitigated the scattered noise at the root of the serration. Another example is the numerical study performed by Halimi *et al.* [19], that investigated the use of sawtooth serrations in the LE and in the TE on propellers. The first ones were effective on reducing the high frequency noise emitted, whereas the TE ones reduced the low to mid frequencies noise while increasing for high frequencies. These results contradict what was to be expected by each serration relative to the frequency range on where they would act beneficially.

Continuing with rotors, which are the case study of this thesis, there are fewer studies for them than for wings. Even so, there are two studies worth mentioning, for both address the aeroacoustic noise and the aerodynamic performance for a relatively small rotor. The first one, performed by Lee *et al.* [20], measured the Sound Pressure Level (SPL) and the thrust generated by four different rotors: a baseline; a sawtooth serrated TE on half of the blade span; a sawtooth serrated TE on a quarter of the blade span; and a rectangular serrated TE. It was concluded that the effectiveness of the serrations vary with the rotation speed, with the half-span serrated rotor performing better (in terms of noise reduction) at certain speeds while the quarter-span serrated rotor performs better on others. Overall, for these two rotors, as the rotation speed increases, the percentage of thrust lost (compared with the baseline) increases. The second study, performed by Li *et al.* [21], compares a sinusoidal TE serrated propeller with a relatively small serration amplitude $2h$ to a baseline. The SPL, lift, drag and torque were measured for hover and forward flight conditions. Although the serration amplitude was small, the noise reduction obtained was considerably good, opposing Howe's conclusion about small serration angles. In addition, it was concluded that for hovering conditions, the noise reduction is greater the lower it is the rotation speed, whereas for forward flight conditions it is the opposite, which means the higher the rotation speed the greater is the noise reduction obtained.

All the studies mentioned so far have approached the aeroacoustic noise thematic in subsonic and incompressible conditions. However, there are studies that cover other flow conditions, such as the one from Nies *et al.* [22] that evaluated, experimentally, the influence of TE serrations on pressure wave amplitude, in transonic conditions. With the use of serrations, the generation of vortexes is disturbed, which also influences the upstream moving waves by reducing their strength, therefore forming a steadier flow.

1.1.2.2 Leading Edge Modifications

Scientists have noted that owls are one of the birds that make the least noise while flying. Bachmann *et al.* [23] performed a systematic analysis on the wing morphology, comparing a barn owl with a pigeon. The goal was to shed some light on the features and mechanisms of the owl's silent flight, so those could be employed in future wing designs. One important observation that explains why this bird's flight is so unique was that the barn owl presents a curved type serration on the LE of the wing, with fringes at the edges of each feather. These characteristics are visible in Figure 1.2.

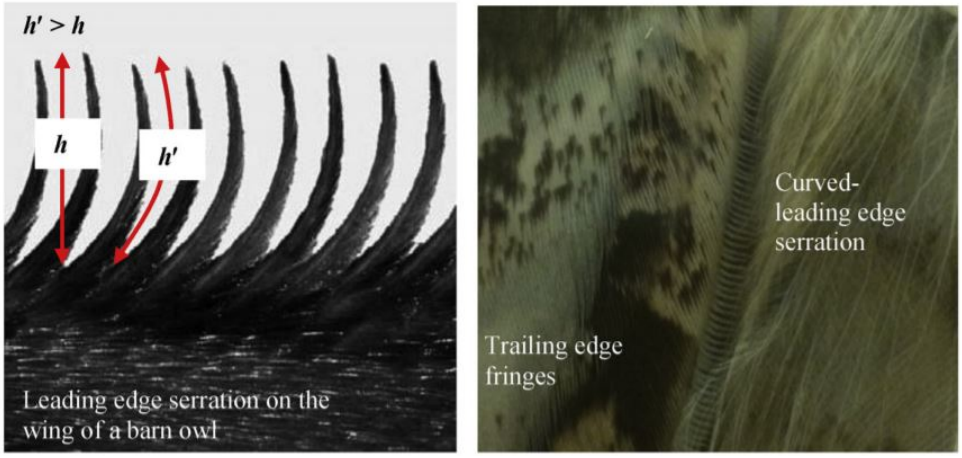

Figure 1.2: Curved LE serrations on owl wings. Figure taken from [24].

Following Bachmann's study, other researchers tried to implement some modifications on wings to imitate those predatory birds, as was the case of Juknevicius and Chong [24], who attached serrated strips to the LE of a NACA-0008 aerofoil. They analysed the aeroacoustic noise and the aerodynamic efficiency for different serration parameters, comparing the curved serration to the sawtooth one. Generally, the best noise reduction is associated with a small serration wavelength λ and a high amplitude h, because these characteristics allow an early breakup of the turbulence eddies by the serration itself. Concerning the curved serration, it has a higher effective serration amplitude h' than a sawtooth one with the same amplitude h, as it can be observed in the picture on the left in Figure 1.2, therefore increasing the serration wetted area and granting a better noise reduction. Other studies that follow the owl morphology are, for example, the one by Shinichiro [25] who applied a jigsaw serrated strip to the LE of a NACA63-414 aerofoil, or even the one by Liang *et al.* [26] who studied the noise reduction of a fan blade with curved serrations on the TE.

Serrated strips on the LE have also been tested with the purpose of improving the aerodynamic coefficients of a wing. Collins [27] studied the use of sawtooth serrated strips, attached to the lower surface near the LE, on two different wings (one a NACA-0015 and the other a NACA-2412), concluding several interesting notions. The first, that the slope of the lift coefficient curve, $C_l \; vs \; \alpha$, increases, without

changing the stall angle. Then, that the drag coefficient C_d was not affected, contrary to what could be expected, while the pitching moment for the cambered aerofoil decreased. Later, Collins tested the influence of sound on the boundary layer control with the use of a loudspeaker, stating that sound did not cause premature transition, instead it could be used to cause partial reattachment of the flow.

Hersh and Hayden [28] addressed the sound radiation from both wings and rotors, affirming that loud tones radiate from these lifting surfaces, generated by vortexes being shed into the aerofoil and propeller wake at a periodic rate. However, with the use of well positioned LE serrated strips it was possible to remove these tones. Soderman also studied the use of serrated strips on the LE, initially the aerodynamic effects caused by them [29], and then the noise reduction effects on low speed rotors [30]. With a $1.52m$ diameter rotor, working between 480 and 1440 Rotations Per Minute (RPM), Soderman concluded that the serrations were definitely more effective in reducing the noise at low tip speeds rather than at high tip speeds. Furthermore, the high frequency noise was the one that decreased the most, considering that the noise reductions ranged from 4 to $8dB$ Overall Sound Pressure Level (OASPL), with reductions of 3 to $17dB$ in the high octave bands. Later, Hersh, Soderman and Hayden [31] continued the investigation on the use of serrated strips both on wings as on small rotors. The rotor tested had $0.36m$ diameter and worked from 2000 to 4000 RPM. They stated that the dominant region of noise generation was the outer one-quarter of the blade radius, finding that the serrations had a clear effect on reducing the broadband noise. This reduction was attributed to a serration vortex generation that mitigated the wake-induced aerofoil noise. Plus, the serrations would also cause a faster dissipation to the tip vortexes, diminishing the tip vortex noise generation.

Considering the modifications to the LE, they do not consist only on serrated strips. There are also serrations on the body itself, but not exactly like the TE serrations, since these are cutouts. In the LE it is important to maintain a smooth and continuous surface, so these serrations preserve the 2D profile and aerodynamic characteristics, changing the profile dimensions along the span. For that reason, the most common LE serration is the sinusoidal one, although there are also some studies which approach sawtooth serrations as well.

Narayanan *et al.* [32, 33] conducted experimental tests on flat plates to assess the importance of the serration variables, λ and h, on the noise reduction achieved. They concluded that the noise reduction increases with greater serration amplitudes, but that the noise reduction is much less sensitive to the serration wavelength. Plus, after performing the parametric analysis with flat plates, they studied the effects on a wing with a NACA-65 aerofoil and noticed that the noise reduction evidenced is generally greater for flat plates than for the wing.

Chong *et al.* [34] performed a parametric analysis on the serration's amplitude and wavelength, evaluating also their influence on the aerodynamic characteristics. They reached the following conclusions:

1. Increasing h benefits the noise reduction but would decrease the lift coefficient and the lift curve

slope.

2. Increasing λ delays the stall angles, but the lift coefficient at pre-stall conditions becomes lower compared to the baseline.

3. The largest noise reduction peak occurs with the highest λ and h. However, these values would increase significantly the high frequency noise.

4. For the best reduction of the OASPL, large h and small λ are advisable.

5. To improve the aerodynamic lift, small h and large λ are advisable.

Following Chaitanya's *et al.* research [35], the origin of the turbulent inflow noise becomes more clear, stating that maximum noise reductions can be achieved when the turbulence integral length-scale Λ equals one half of the serration wavelength. Plus, it shows that the noise reductions normally increase with increasing frequency up until the frequency where the aerofoil self-noise becomes predominant. Furthermore, it implies that the total noise radiated is dominated by the turbulent inflow noise (generated in the LE) at low frequencies, whereas the TE noise dominates at high frequencies. As such, the effectiveness of LE serrations is limited by the dominance of aerofoil self-noise, which can be approached with the use of TE serrations. In this study, the authors present the notion of an optimum serration inclination angle, which achieves maximum noise reductions to low frequency noise in the approximated range of $0.2 * U_0/h < f < U_0/h$. However, in a more recent study [36], they defend that rather than an optimum angle, there exists an optimum serration wavelength. In this optimum condition, adjacent noise sources are excited only just incoherently and the sound power radiated varies inversely proportional to the Strouhal number based on the serration amplitude $St_h = f.h/U_0$.

Roger *et al.* [37] studied the turbulence impingement noise reduction with the use of a wavy LE serration (or tubercles, as the authors name them) and a porous serrated TE, on a NACA-0012 aerofoil. They state that a properly shaped serration on the LE has beneficial effects aerodynamically and acoustically, because these serrations prevent the flow from separating and delay the onset of stall. With the LE serrated aerofoil, the maximum noise reduction achieved was $10dB$, whereas with the porous serrated one the maximum was $5dB$.

Obviously, the noise sources on a lifting surface do not depend only on its geometry, but also on the flow properties. As so, Biedermann *et al.* [38] tested sinusoidal LE serrations on a NACA65(12)-10 aerofoil and developed a statistical-empirical model that predicted the sound pressure level and the noise reduction. The main factors taken into account were: the Reynolds number Re; the turbulence intensity; the serration amplitude h; the serration wavelength λ; and the AoA α. It was deduced that the main contributors to the broadband noise emissions were the Reynolds number and the freestream flow turbulence intensity, whereas the serration amplitude, the Reynolds number and the serration wavelength were the main factors to contribute to the broadband noise reduction, in that order. However,

although the serration amplitude was more influential than the wavelength, it was the relation between the turbulence intensity and the serration wavelength that determined the broadband noise reduction capability.

There are also studies that target rather specific applications, as is the one performed by Clair *et al.* [39], who tested LE sinusoidal serrations with the objective of reducing the turbofan interaction noise. For all tested flow speeds, a 3 to $4dB$ reduction to the Sound Power Level (PWL) was obtained without deteriorating the aerodynamic characteristics.

So far, only experimental studies addressing LE serrations have been presented, but there have also been some numerical studies worth mentioning. Haeri *et al.* [40] investigated the turbulence interaction noise for flat plates with wavy LE serrations. The deformation of the vortexes near the LE is the cause for the noise reduction, and it was known that increasing the serration amplitude leads to greater noise reduction. However, the authors concluded that there exists a maximum serration amplitude beyond which, by increasing it, there is no improvement to the noise reduction. In a later study [41], the same authors affirm that for a wavy LE, the geometric obliqueness provoked a noise cutoff effect mainly between the peak and the hill centre of the geometry of the serration, which in turn resulted in noise reduction in the mid to high frequency range. Another interesting numerical study is the one performed by Aguilera *et al.* [42], who focuses on the interaction of anisotropic turbulence with wavy LE serrations, and its influence on noise radiation. It is stated that the noise reduction is connected to the length scales of vortical disturbances and that small variations may lead to considerable changes to the noise sources. In addition, the anisotropic turbulence spectra characterizes the frequency content of the noise sources, with high frequency noise being affected by a stretching of the turbulent structures in the spanwise direction and the low frequency being affected by changes in the chordwise direction.

One interesting configuration is the slitted LE serration, approached by Chaitanya, Joseph and Narayanan [43, 44]. Slits are cut in the chordwise direction, forming two different noise sources at either end of the slit. The purpose of the slit is to have a determined length that will make the two different noise sources be out of phase with each other, cancelling out the noise produced by both. This configuration presented very good levels of noise reduction for flat plates and wings, but for rotating blades it became a difficult challenge to design such blade.

1.2 Objectives

An experimental study will be performed on three different configurations of rotating blades: First, a blade with a sawtooth TE serration with flat tips. Of this type of blade, three different blades will be tested, with the serration implemented on 20% of the span, 40% and 60%. This way it is possible to study the influence of the serration in different sections of the blade; Second, a blade with a sinusoidal LE serration.

Of this type, another three different blades will be tested, and also with the serration implemented on 20%, 40% and 60% of the span; Third, a baseline, which is a typical blade with unaltered LE and TE. The two previous configurations will be compared to the baseline to assess the noise reduction and the aerodynamic performance degradation obtained. So, in total, seven different rotors will be tested.

With the seven different blades, the objectives of the experimental tests are:

- To measure the SPL obtained with each blade for different rotation speeds. This way, for each speed, it is possible to compare the frequency varying SPL of the blades to assess the noise reduction effects of the serrations on different frequency intervals;
- To compare, for both the TE and the LE serrated blades, the effectiveness of the percentage of the span that is serrated;
- To compare the Equivalent Continuous Sound Level (Leq) of each rotor, as an overall measure of the noise produced by each rotor;
- To appraise the aerodynamic performance by comparing the thrust and the power obtained between the baseline and the other different blades.

1.3 Thesis Outline

This thesis will follow the following structure:

- Chapter 1 introduces the aerodynamic noise problem and work developed in this thesis;
- Chapter 2 addresses the blades that were designed and printed;
- Chapter 3 overviews the experimental setup and the Data Acquisition (DAQ) system employed;
- Chapter 4 presents the experimental results obtained and the respective assessment.
- Chapter 5 concludes the thesis.

2

Design of the Blades

Contents

2.1 Blade Geometry

The objective was to test small UAV rotors. First, a research was made about the size of small rotors and their respective rotation speed. It was concluded that the smaller rotors operate at higher rotation speeds, which is logical since the blade tip speed is a design constraint, so the smaller the blade's span means that higher rotation speeds can be employed, and higher rotation speeds lead to higher thrust. From Inês Amado [45], who performed a study on coaxial rotors at Instituto Superior Técnico (IST), there was extensive information about the equipment that would be used. Amado performed tests on relatively small rotors that reached a maximum of 10000 RPM. However, in the present study, it was not initially intended to evaluate such high rotation speeds because the research previously made showed that even for the smaller UAV rotors they normally did not reach those values. At those speeds the centrifugal force plays a considerable role, and from the start of this project it was intended to use 3D printing to produce the blades. With 3D printing, although there is a wide range of materials that can be used, the first choice was the cheapest and most widely used plastic filament in 3D printing, which is the Polylactic Acid (PLA). The PLA presented interesting mechanical characteristics, but, to ensure the safety of the experiment, smaller rotation speeds than 10000 RPM were targeted. In addition, a structural analysis of the main forces involved on the rotor was performed, which will be presented further on in this Chapter.

H. M. Lee *et al.* [20], who performed an acoustic study on TE serrated rotors, tested blades with $22.5cm$ of radius for rotation speeds ranging from 1500 to 3000 RPM. However, the workbench used by Amado used a beam, where the motor and rotor would be installed, and it was not much taller than those blades. So, smaller blades than those used by H. M. Lee needed to be designed. In addition to the constraint imposed by the workbench, the 3D printer used, an Ultimaker 3, had a limited available space for printing each part.

At first, the blades designed had $11.85cm$ of radius, as are shown in Figure 2.1. These blades presented several flaws related with the printing process, which will be addressed in the "3D Printing" section. The solution found, along with other printing characteristics, was to increase the blade size. However, to comply with the limited space available for printing, every rotor hub was divided in half and each blade was printed as a separate part. In the end, the drawings were scaled proportionally with a factor of 1.5, reaching a blade radius of $R = 17.78cm$ with a chord varying from $2.25cm$ to $3cm$ (not counting with the blade tip).

The NACA-0018 aerofoil was chosen, for it is one of the most studied aerofoils and it has a relatively high thickness, as opposed to the thickness of the NACA-0012 aerofoil. The NACA-0012 aerofoil was not considered because, due to its small thickness, it was more difficult to manufacture the blades with a satisfactory surface quality in the TE using the 3D printer available. The selected aerofoil does not have camber because, although it is of interest to evaluate the thrust between the baseline and the different

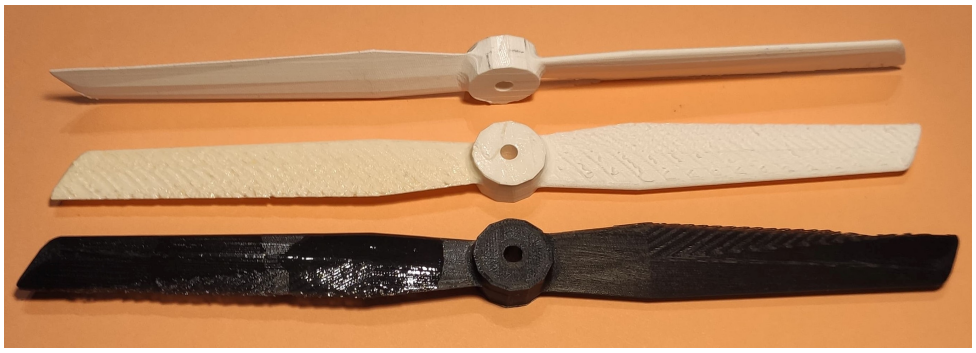

Figure 2.1: First 3D printed rotors.

serrated blades, it is not an objective to optimize the thrust. However, to generate thrust, the blade has a linear varying twist that starts at the root with $12°$ and ends at the tip with $2°$. The twist at the root was chosen to be a high value, as is typically used in helicopter blades, but still a value where it can be considered that the lift coefficient varies linearly with the angle of attack. The twist at the tip was chosen to be a low value, that had in account the negative effect of the induced velocity to the effective angle of attack.

With the use of Solid Edge, a CAD software, seven different rotors were designed and printed, to finally be tested. They are enumerated in Table 2.1, and they are all shown in Figure 2.2. Next, the dimensions of the TE and LE serrations will be presented.

Table 2.1: The different rotors studied.

	Rotor type	Percentage of serrated span
Baseline	Baseline	-
TE60	TE serration	60%
TE40	TE serration	40%
TE20	TE serration	20%
LE60	LE serration	60%
LE40	LE serration	40%
LE20	LE serration	20%

2.1.1 Trailing Edge Serrations

Figure 2.3 shows one of the sawtooth serrated blades. These TE serrations simulate cuts that are made to the blade itself, extracting material. In Figure 2.4 it is presented the serration parameters, where $2h$ is the serration amplitude, λ is the wavelength, θ is the angle between the serration edge and the mean flow direction and a is the flat tip width.

Howe stated, through his numerical predictions [5], that a wavelength-to-amplitude ratio such that $\lambda/h \geq 10$ would result in a noise attenuation of $1dB$, whereas with the ratio $\lambda/h = 1$ resulted in approximately $8dB$ of attenuation. Howe then concluded that to obtain optimal attenuation, one should use

Figure 2.2: All tested rotors.

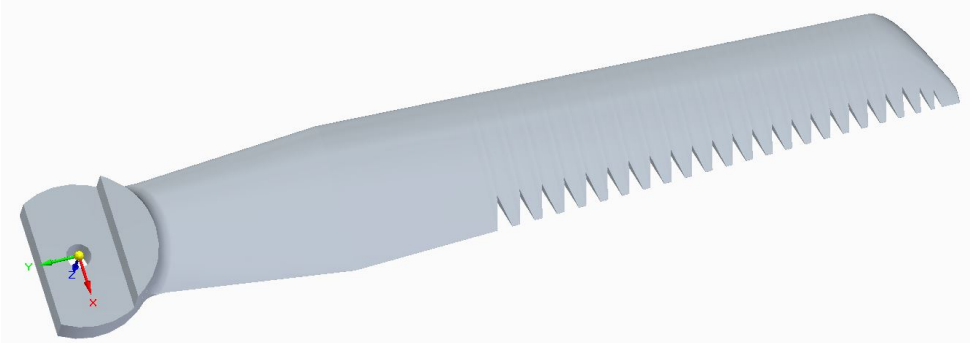

Figure 2.3: Sawtooth TE design.

sawtooth serrations, as opposed to TE sinusoidal serrations, with the edges inclined at less than $45°$ to the mean flow. So, considering Howe's findings, Lee's experimental study and keeping in mind Gruber's conclusions [9], that were mentioned in Chapter 1, the sawtooth serration parameters were defined as the following:

- The amplitude $2h$ varies along the span and equals to 1/4 of the blade chord;
- The wavelength λ is defined by the ratio $\lambda/h = 0.9$, the same followed by Lee;
- The angle θ is automatically defined by the two previous parameters, and it is equal to $13°$;
- The flat tip width a was chosen to be 1/2 of the serration wavelength.

The flat tips increase the effective surface area, therefore helping not to lose some of the lift that is lost with the serrations. Concerning the width, no relevant information was found, so it was chosen to be

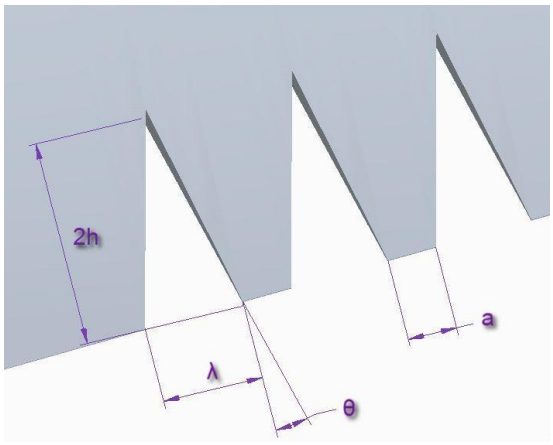

Figure 2.4: Sawtooth dimensions.

equal to $\lambda/2$ because it seemed reasonable and it varied linearly along the span, as the amplitude and the wavelength.

2.1.2 Leading Edge Serrations

In the case of the LE serrations approached in this thesis, there is no material extraction, but instead a deformation to the blade geometry that provides a continuous surface to the blade. These serrations consist in a sinusoidal smooth surface, without edges, in order to be an efficient aerodynamic body. Figure 2.5(a) shows a 3D drawing of one of the LE serrated blades, where it is clear the smooth surface all throughout the blade. The cross section is, also, always the NACA-0018 aerofoil in the serrated part, where the chord results from the sum of two equations: the baseline chord that varies linearly with the span; and the sinusoidal equation characterized by the amplitude $2h$ and the wavelength λ. These serration parameters are presented in Figure 2.5(b), as also the serration inclination angle θ, and the turbulence integral length-scale Λ that is referenced in Chapter 1, concerning the investigation performed by Chaitanya *et al.* [35].

In the bibliographic research performed, there were no studies found concerning LE serrations applied to rotating blades. In that way, this thesis is probably one of the first studies to evaluate such kind of configuration. Therefore, to design these serrated blades, the information gathered for flat plates and wings was reviewed and adapted to the case of a rotating body. Following Chong's conclusions [34], presented in Chapter 1, a high amplitude and small wavelength would be the best to reduce the OASPL. However, to a rotating blade, this would disrupt the flow at a large scale, and probably worsen the aerodynamic and aeroacoustic characteristics. On the other hand, to enhance the aerodynamic characteristics, it was advisable to implement a small amplitude with a large wavelength. In this sense, it was opted to implement a relatively medium-small serration amplitude, and a relatively medium-high wavelength. The

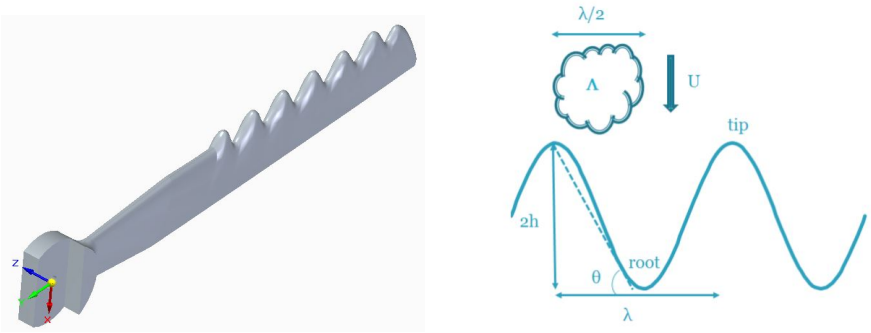

(a) LE serrated blade

(b) Serration dimensions (taken from [35])

Figure 2.5: LE serrated blades design.

dimensions are presented next:

- The amplitude $2h$ varies along the span and equals to 1/3 of the local chord;
- The wavelength λ is constant and equal to $1.5\ cm$.

2.2 Thrust, Power and Bending Moment Assessment

2.2.1 The Blade Element Theory

In this section is presented a simple method to calculate the thrust T, the power P and the bending moment M'_x. The objective of this analysis is not to evaluate aerodynamic behaviors with great detail, but rather to predict these variables' values with a sufficiently good precision and assess their order of magnitude. In the next section these results are applied to perform a structural analysis, in order to ensure that the blades do not break and that the experiment is done safely.

The method follows the Blade Element Theory (BET), proposed by Stefan Drzewiecki and described by Leishman [46], and consists on dividing the blade in several small sections and assuming that each section acts as a bidimensional aerofoil. The forces and moments can be calculated in each blade element, and by integration the total forces, moments and power of the entire rotor are obtained. This method takes into account the dimensions of the blades and the characteristics of the profile, whereas the major approximation is assuming that the flow behaves as bidimensional in each blade element.

Figure 2.6 demonstrates how the position of each element is considered, introducing the velocities existing in the rotor plane, as the radial velocity U_R, the transverse velocity U_T and the total velocity U projected on the plane. Choosing a Cartesian referential centered on the rotation center, with the XX axis following a chordwise direction, the YY axis a spanwise direction and the ZZ axis pointing

upwards, the element dy is at y distance from the center of rotation. The hub radius is r_0 and, again, R is the blade radius. As is characteristic in a rotor, the transverse velocity varies linearly along the span, since it is given by the rotation speed Ω and the position of the element, as is expressed in equation 2.1.

$$U_T = \Omega.y \tag{2.1}$$

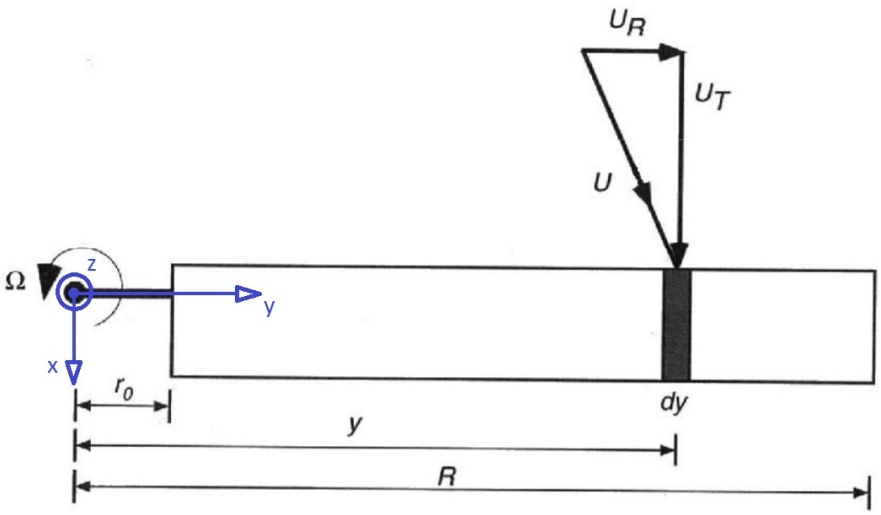

Figure 2.6: The blade element characterisation used in the BET. Figure adapted from [46].

Figure 2.7 shows the aerofoil of a blade element and the forces and moment acting on it. Again, the velocities existing on this section view are represented, with U being the total velocity and U_P the velocity perpendicular to the rotor plane. U_P is expressed in equation 2.2, where V_C is the rotor climb velocity and v_i is the induced velocity generated by the functioning of the rotor. Since the experiments will only operate in hover conditions, V_C will be taken as null.

$$U_P = V_C + v_i \Rightarrow U_P = v_i \tag{2.2}$$

Assuming that the problem is bidimensional, the radial velocity will be neglected. Therefore, the total velocity is given by the sum of its components, as is expressed in equation 2.3.

$$U = \sqrt{U_P^2 + U_T^2} \tag{2.3}$$

The elemental thrust dT for one blade element will correspond to the elemental force in the ZZ direction dF_Z. Similarly, the elemental power dP required will need to compensate the elemental force parallel to the rotor plane, in the XX direction, which is dF_x. These forces can be broken down into the two aerodynamic forces, the elemental lift dL and the elemental drag dD, shown by the following

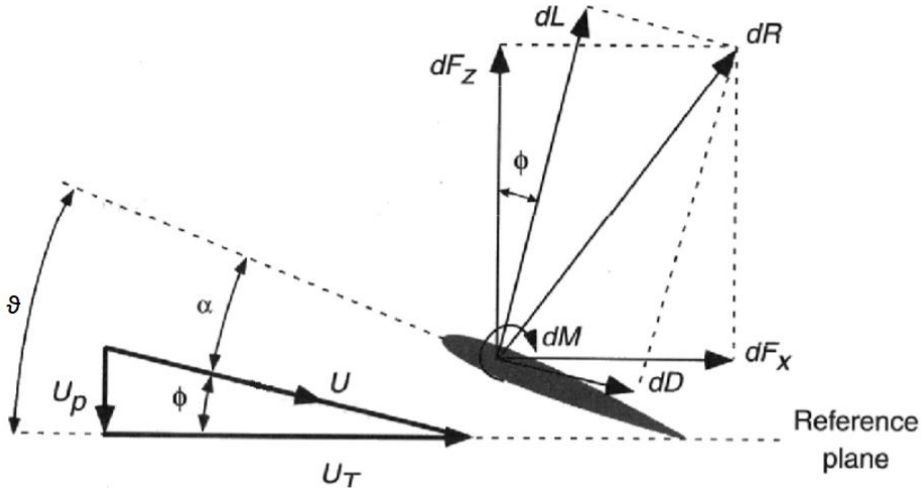

Figure 2.7: Bidimensional characterisation used in the BET. Figure taken from [46].

equations 2.4 and 2.5.

$$dT = dF_z = dL.cos\phi - dD.sin\phi \tag{2.4}$$

$$dF_x = dL.sin\phi + dD.cos\phi \tag{2.5}$$

The elemental thrust is directly defined in equation 2.4, whereas the power is still undefined. Power relates to a force times a velocity acting in the same direction. Therefore, the power is given by the resistance force in the rotor plane and the transverse velocity, resulting in the following equation 2.6.

$$dP = dF_x.\Omega.y \tag{2.6}$$

From the Figure 2.7, it is possible to notice that the inflow angle ϕ is the angle between the total velocity and the transverse velocity, and is given by the trigonometric relation $\phi = tan^{-1}(U_P/U_T)$. However, assuming that the transverse velocity is much larger than the induced velocity, $U_T \gg v_i$, ϕ will be very small ($\phi \approx 0$), therefore making it possible to make the following simplifications.

$$\begin{cases} U \approx U_T \\ \phi \approx \dfrac{v_i}{U_T} \\ sin\phi \approx \phi \\ cos\phi \approx 1 \end{cases} \tag{2.7}$$

These simplifications can be directly applied to equations 2.4 and 2.5. On another note, noting that the elemental lift is considerably higher than the elemental drag, $dL >> dD$, and also that ϕ is very small, the second term in equation 2.4 is residual in comparison to the first term, and, therefore, it can

be neglected, resulting in equation 2.8.

$$dT = dL \tag{2.8}$$

In turn, the elemental power results in equation 2.9.

$$dP = dF_x.\Omega.y = (dL.\phi + dD)\Omega.y \tag{2.9}$$

The elemental lift and drag, which are given as a force per unit of length, can be expressed through the aerofoil coefficients C_l and C_d, as follows:

$$\begin{cases} dL = \frac{1}{2}\rho.U^2.c.C_l.dy \\ dD = \frac{1}{2}\rho.U^2.c.C_d.dy \end{cases} \tag{2.10}$$

In equations 2.10, ρ stands for the flow density and c for the chord. Although the dimensions vary along the blade's span, the aerofoil used is always a NACA-0018, so the knowledge available about this aerofoil can be used [47]. The lift coefficient varies linearly with the effective angle of attack α for small angles, while the drag coefficient varies with α according to a quadratic function. Both relations are expressed in equations 2.11.

$$\begin{cases} C_l = C_{l_\alpha}.\alpha \\ C_d = 7.097 \times 10^{-5}\alpha^2 + 6.863 \times 10^{-3} \end{cases} \tag{2.11}$$

At last, the total thrust generated by one blade and the power to overcome the aerodynamic resistance are achieved in equations 2.12 and 2.13 by integrating the quantities produced by each blade element along the blade.

$$T = \int dL.dy = \frac{1}{2}\int \rho.U^2.c.C_{l_\alpha}.\alpha.dy \tag{2.12}$$

$$P = \int (dL.\phi + dD)\Omega.y.dy = \frac{1}{2}\int \left(\rho.U^2.c.C_{l_\alpha}.\alpha.\phi + \rho.U^2.c.C_d(\alpha)\right)\Omega.y.dy \tag{2.13}$$

In the same way, it is possible to obtain the bending moment M'_x:

$$M'_x = \int dL.y.dy = \frac{1}{2}\int \rho.U^2.c.C_{l_\alpha}.\alpha.y.dy \tag{2.14}$$

2.2.2 Thrust and Power Calculation

For the calculations, only the baseline blade will be considered. On one hand, the thrust produced by the TE serrated blades cannot be calculated with the BET because the part itself suffers cuts, therefore the information known for the NACA-0018 aerofoil, specifically the aerodynamic coefficients, is not applicable. On the other hand, in spite of the LE serrated blades following fully the NACA-0018 aerofoil,

there is no information to ensure that it is reasonable to consider the flow behavior to be bidimensional in each blade element, and as such, the results that would be achieved might not have a real meaning. However, as the studies mentioned in Chapter 1 suggest, both the TE serrated blades as the LE serrated blades should produce a slightly lower thrust than the baseline. Plus, as mentioned in the beginning of this section, the objective is to predict the force in order to perform a structural analysis, and doing so for the baseline does serve this goal.

The first task is to identify which terms are constant in equation 2.12. Considering that the rotor is expected to work from 2000 to 5000 RPM, the maximum tip velocity, that is the tip velocity for the highest rotation speed, is $V_{tip} = \Omega.R = 92.9\ m/s$. This velocity relates to a Mach number lower than 0.3, thus the flow can be considered incompressible and ρ is taken as constant. Aside from the density, only the derivative of the lift over the angle of attack C_{l_α} can be taken as constant, because it will only be used for small angles of attack. As for the rest of the terms, they all vary with y.

The total velocity will be approximated as shown in equations 2.7, and it will be written as the following equation 2.15.

$$U = \Omega.y \tag{2.15}$$

The variation of the chord with the span is a design parameter, which was chosen upon while drawing the blades. This variation is described by equations 2.16.

$$c(y) = \begin{cases} 0.0225 + 0.2(y - 0.015), & if \ \ 0.015 \leq y \leq 0.0525 \\ 0.03 - \dfrac{1}{15}(y - 0.0525), & if \ \ 0.0525 \leq y \leq 0.165 \\ -129.67y^2 + 42.917y - 3.5285, & if \ \ 0.165 \leq y \leq 0.1778 \end{cases} \quad [m] \tag{2.16}$$

The last term is the effective angle of attack. In Figure 2.7 this angle is displayed as the difference between the pitch angle ϑ and the inflow angle. As only hovering conditions will be considered, the rotor is considered leveled in its plane and the pitch angle equals the twist of the blade. In turn, ϕ is given by equation 2.7. So, α results in equation 2.17

$$\alpha = \vartheta - \phi = \begin{cases} \left[12 - \dfrac{200}{3}(y - 0.015)\right] - \dfrac{v_i}{\Omega.y}, & if \ \ 0.015 \leq y \leq 0.165 \\ 2 - \dfrac{v_i}{\Omega.y}, & if \ \ 0.165 \leq y \leq 0.1778 \end{cases} \quad [^\circ] \tag{2.17}$$

Developing equation 2.12, the total thrust for a two bladed rotor presents as follows:

$$T = \int_{0.015}^{0.0525} \rho.\Omega^2.y^2.\left[0.0225 + 0.2(y - 0.015)\right].C_{l_\alpha}.\left[12 - \frac{200}{3}(y - 0.015) - \frac{v_i}{\Omega.y}.\frac{180}{\pi}\right]dy+$$
$$\int_{0.0525}^{0.165} \rho.\Omega^2.y^2.\left[0.03 - \frac{1}{15}(y - 0.0525)\right].C_{l_\alpha}.\left[12 - \frac{200}{3}(y - 0.015) - \frac{v_i}{\Omega.y}.\frac{180}{\pi}\right]dy+ \quad (2.18)$$
$$\int_{0.165}^{0.1778} \rho.\Omega^2.y^2.\left[-129.67y^2 + 42.917y - 3.5285\right].C_{l_\alpha}.\left[2 - \frac{v_i}{\Omega.y}.\frac{180}{\pi}\right]dy$$

The third term in equation 2.18 refers to the blade tip. This term could be neglected if the blade tip losses were taken into account. However, to be on the safe side, it was chosen to keep this term, resulting in an over-prediction of the thrust.

The only parameter missing to obtain T is the variation of the induced velocity v_i along the span. A common approximation used is to consider the induced velocity to be constant and equal to the result given by the Momentum Theory, also described by Leishman [46], which is indicated in equation 2.19, where A stands for the rotor area. Although the thrust equation presents the variable T on both sides, it still produces numerical results.

$$v_i = \sqrt{\frac{T}{2A.\rho}} \quad (2.19)$$

The same procedure is applied to reach the power for a two bladed rotor, and developing equation 2.13 it results in the following:

$$P = \int_{0.015}^{0.0525} \rho.\Omega^3.y^3.\left[0.0225 + 0.2(y - 0.015)\right] \times \left(C_{l_\alpha}.\left[12 - \frac{200}{3}(y - 0.015) - \frac{v_i}{\Omega.y}.\frac{180}{\pi}\right].\frac{v_i}{\Omega.y}+\right.$$
$$\left. 7.097 \times 10^{-5}\left[12 - \frac{200}{3}(y - 0.015) - \frac{v_i}{\Omega.y}.\frac{180}{\pi}\right]^2 + 6.863 \times 10^{-3}\right)dy+$$
$$\int_{0.0525}^{0.165} \rho.\Omega^3.y^3.\left[0.03 - \frac{1}{15}(y - 0.0525)\right] \times \left(C_{l_\alpha}.\left[12 - \frac{200}{3}(y - 0.015) - \frac{v_i}{\Omega.y}.\frac{180}{\pi}\right].\frac{v_i}{\Omega.y}+\right.$$
$$\left. 7.097 \times 10^{-5}\left[12 - \frac{200}{3}(y - 0.015) - \frac{v_i}{\Omega.y}.\frac{180}{\pi}\right]^2 + 6.863 \times 10^{-3}\right)dy+ \quad (2.20)$$
$$\frac{1}{2}\int_{0.165}^{0.1778} \rho.\Omega^3.y^3.\left[-129.67y^2 + 42.917y - 3.5285\right] \times$$
$$\left(C_{l_\alpha}.\left[2 - \frac{v_i}{\Omega.y}.\frac{180}{\pi}\right].\frac{v_i}{\Omega.y} + 7.097 \times 10^{-5}\left[2 - \frac{v_i}{\Omega.y}.\frac{180}{\pi}\right]^2 + 6.863 \times 10^{-3}\right)dy$$

Regarding the constants that were assumed, the atmospheric properties are considered to follow the standard sea-level conditions, and therefore the density has a value of $\rho = 1.225\ kg/m^3$. The derivative of the lift coefficient over the angle of attack is considered $C_{l_\alpha} = 0.1075\ /^\circ$, provided by Airfoil Tools [47] for a NACA-0018 aerofoil, because only small angles are used. Calculating for the different tested rotation speeds, the thrust and the power of a two bladed rotor is given in Table 2.2.

Table 2.2: Thrust generated by a single blade for different rotation speeds.

RPM	2000	2500	3000	3500	4000	4500	5000
T [N]	0.379	0.592	0.853	1.161	1.516	1.919	2.369
P [W]	0.919	1.792	3.097	4.919	7.343	10.455	14.341

The thrust obtained here is close to the values obtained from the experiment (which will be presented in Chapter 4), noting that, in theory, the thrust is directly proportional to the square of the rotation speed. Relatively to the power, it will be interesting to compare those values to the ones from the experiment because it is expected to have a higher power than the theoretical one. Since the BET does not account with 3D effects, and the experiment deals with small rotors with very high rotation speeds, there are in fact a lot of 3D effects related to the turbulence and vortex shedding that will cause the drag to be significantly higher than the one computed, therefore increasing the power experienced.

With the thrust and the power computed, the Figure of Merit (FM) can also be estimated. The FM is an indicator of the rotor efficiency which compares the ideal power required for hovering, P_I, with the power actually consumed to hover, P. Equation 2.21 [46] expresses the calculation of the FM, where the ideal power coefficient is given by the Momentum Theory as $C_{P_I} = \frac{C_T^{3/2}}{\sqrt{2}}$.

$$FM = \frac{P_I}{P} = \frac{C_{P_I}}{C_P} = \frac{C_T^{3/2}}{\sqrt{2}C_P} \tag{2.21}$$

Knowing that the thrust and power coefficients, C_T and C_P, are defined as presented in equation 2.22, the FM is finally computed, reaching a value of $FM = 0.515$ for all different rotation speeds.

$$\begin{cases} C_T = \dfrac{T}{\rho.A.\Omega^2.R^2} \\ C_P = \dfrac{P}{\rho.A.\Omega^3.R^3} \end{cases} \tag{2.22}$$

2.2.3 Bending Moment Calculation

Continuing with equation 2.14 and developing in the same way as with the thrust calculation, the bending moment experienced at the root for a single blade presents as follows:

$$M'_x = \frac{1}{2}\int_{0.015}^{0.0525} \rho.\Omega^2.y^3.\left[0.0225 + 0.2(y-0.015)\right].C_{l_\alpha}.\left[12 - \frac{200}{3}(y-0.015) - \frac{v_i}{\Omega.y}.\frac{180}{\pi}\right]dy+$$
$$\frac{1}{2}\int_{0.0525}^{0.165} \rho.\Omega^2.y^3.\left[0.03 - \frac{1}{15}(y-0.0525)\right].C_{l_\alpha}.\left[12 - \frac{200}{3}(y-0.015) - \frac{v_i}{\Omega.y}.\frac{180}{\pi}\right]dy+ \quad (2.23)$$
$$\frac{1}{2}\int_{0.165}^{0.1778} \rho.\Omega^2.y^3.\left[-129.67y^2 + 42.917y - 3.5285\right].C_{l_\alpha}.\left[2 - \frac{v_i}{\Omega.y}.\frac{180}{\pi}\right]dy$$

The structural analysis will be performed in the most critical condition, that is for the highest rotation speed. In the same way, the bending moment will only be of interest in this condition. So, calculating for 5000 RPM, the bending moment experienced at the root of a single blade results in $M'_x = 0.125\ N.m$.

2.3 Structural Analysis

The structural analysis presented in this section was performed using the simulation by finite elements software included in Solid Edge. The blades were designed in the same program, and it was necessary to define the material used and to apply the forces, rotation speed and the constraints to the object of study.

The material chosen was the PLA plastic, which is one of the most commonly used materials in 3D printing. The choice of the material is further explained in the next section concerning the 3D printing. Then, it is applied the lift calculated along the blade for the highest rotation speed to be tested, 5000 RPM. Beforehand, it was expected that the lift would produce a maximum bending moment to the root of the blade, and this area would be where the stresses were greater. In addition, the rotation of the rotor produces a centrifugal force that could not be neglected considering the high rotation speeds used.

Running the simulation, the higher stresses occur in the root as expected, specially on the TE since the profile thickness is lower there. The highest stress is estimated to be $13.3\ MPa$, whereas the yield stress of the material in bulk is $59\ MPa$. Therefore, the safety factor for the rotor, in the considered conditions, is 4.43

The highest deformation occurs at the area that is farthest from the center, and it is caused both by the centrifugal force and the aerodynamic forces. The centrifugal force elongates the blade spanwise, making the elements dislocate radially, while the aerodynamic forces, mainly the lift, acting on the blade will bend the blade at the root, dislocating the elements upwards. However, in the simulated conditions,

the blade maximum deformation is reached at the tip with 0.41 millimeters, which is a relatively small deformation.

The structural analysis presented in this section was for the most extreme conditions that were supposed to be carried out at the experiments, however several other simulations for higher rotation speeds were also performed. In an initial phase of this thesis, it was intended to experiment the different rotors with a maximum rotation speed of 8000 RPM, but the simulations showed that the stresses and the deformation would increase greatly from those that were presented, and reaching a safety factor lower than 2, which could be compromising when performing the experiment. So, as the designs were perfected, these simulations helped establish the range of rotation speeds to test in the experiments.

2.4 3D Printing

Having performed the structural analysis, it was time to start printing. The printing was carried out in the Laboratório para Desenvolvimento do Produto (that translates to Laboratory for the Product Development) in the IST campus. After a long process to perfect the printing method, it was possible to print all blades with a good surface quality and with a rigorous detail. In this section it will be presented some of the difficulties that were found relative to the printing process, and the respective solutions that enabled to get the final parts with a satisfactory quality.

2.4.1 Choosing the Material

With the 3D models designed, the material to print it with had to be selected. In fact, the first choice of the material was made when the structural analysis was being performed, because it was necessary to know the material properties to estimate the stresses. However, only after printing and testing a few rotors was it possible to be certain about the material chosen.

First, a market search of the materials available was made. The most important characteristics were: Strength; Young's Modulus; Stiffness; Price and Printability. After evaluating several materials, the choices came down to three: Acrylonitrile Butadiene Styrene (ABS); PLA and Carbon Fiber Reinforced Polymer. To better compare these materials, it is presented Table 2.3, which is adapted from [48]. To evaluate the strength it is presented the Ultimate Stress which is the maximum stress that the material can withstand before breaking. The Stiffness and Printability parameters are shown as comparative parameters.

The PLA was the chosen material, for it presents a high Ultimate Stress and is the cheapest one, along with ABS. Plus, it is the one with highest Printability, which classifies materials on how easy they are to print with based on factors like oozing, warping, clogging and other difficulties.

Table 2.3: Printing materials and their characteristics.

	Ultimate Stress [MPa]	Young's Modulus [GPa]	Stiffness	Price per kg	Printability
ABS	40	2.6 - 3.1	5/10	10 - 20 €	8/10
PLA	59	3.75	7.5/10	10 - 20 €	9/10
Carbon Fiber RP	45 - 48	220 - 240	10/10	30 - 70 €	8/10

2.4.2 Printing Techniques

In order to print, the software Ultimaker Cura was used. This software used the 3D drawings created in Solid Edge, making it possible to configure how the printing was to proceed. For example, it allowed to configure the material extrusion thickness, the part infill, the support and its material, infill, position and pattern, the part printing position and many other more detailed options.

As it was mentioned earlier in this Chapter, at first the rotors were designed with $11.85cm$ of radius, as the ones in Figure 2.1. The first one was the dark one, which was printed with an extrusion thickness of $0.1mm$. This rotor presented an awful quality in the lower surfaces of the blades due to the contact with the support created, and a terrible finishing in both trailing edges. To correct these flaws, the next rotors were printed from there on with an extrusion thickness of $0.06mm$. The two white rotors were next and they were printed as they stand, one with the support touching the leading edge on one of the blades and the trailing edge on the other blade (the rotor on top) and the other with the support on the lower surfaces of the blades (the one in the middle of Figure 2.1). The white one on top improved considerably, but still had a bad finishing on the edges in contact with the support. The white one in the middle still had the issue of having a very bad quality in the lower surfaces.

To correct these issues, it was decided to change three things. First, the support used would be from a different material, Polyvinyl Alcohol (PVA), which is a soluble material and it does not meld with the PLA part. Second, in order to have less errors due to small details, the blades would be made bigger, so all drawings were scaled with a factor of 1.5. Last, each blade would be printed separately, with the hub divided in two in such a way that each pair of blades would fit in together when attached to the motor, during the experiment. Figure 2.8 presents the corrective measures taken, with the PVA support shown in 2.8(a) and the divided hub in 2.8(b).

After these changes, the quality of the parts got significantly better. However, no part should be printed with the lower surface of the blade in touch with the support, otherwise the lower surface would get a bit rough and distorted at the tip. So, to circumvent this problem, the blades were printed with the LE facing down and in touch with the soluble support, as is presented in Figure 2.9(a). The baseline blades and the TE serrated blades were printed this way. On the other hand, the LE serrated blades could not be printed like this because the support would only touch the blade in specific points, instead of touching along the whole edge. So, in the case of the LE serrated blades, these were printed in a standing position, as it is shown in Figure 2.9(b). The support touches only the hub, leaving the blade

itself with no irregularities or flaws due to the support.

(a) PVA support

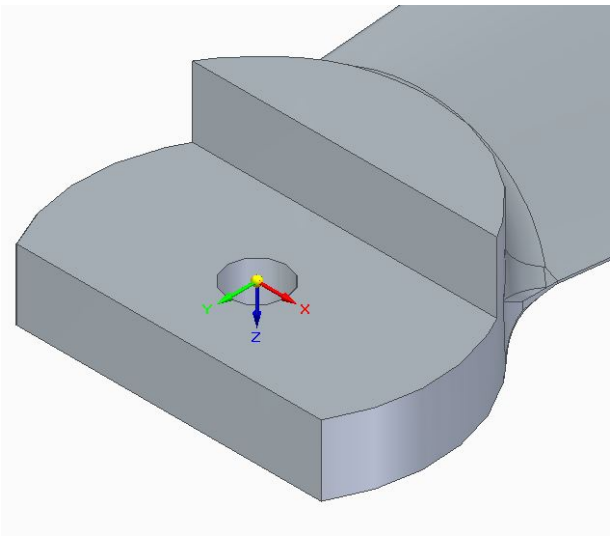

(b) The divided hub at the end of each blade.

Figure 2.8: Corrective measures to the printing process.

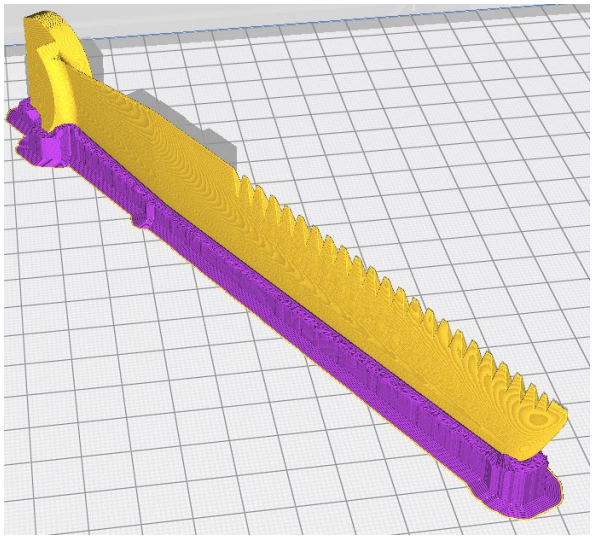

(a) TE serrated blade with PVA support

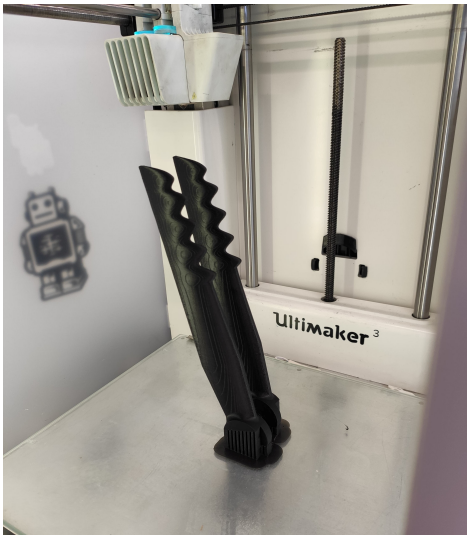

(b) LE serrated blades printed in a standing position

Figure 2.9: Final printing techniques.

2.4.3 Post Processing

Even after refining the printing technique, the printed parts are not exactly perfect. Plus, being the part in question a rotor blade, the detail of the surface is extremely important. So, to perfect the blades, there are techniques that could be applied.

First, to smoothen the surface, a sandpaper was used. However, since this technique removes material, and it is not desired to alter the shape of the blade, a fine-grained sandpaper was used and applied, with the utmost care, and light pressure, only on local flaws and imperfections. This way, the shape of the blade remains true to the 3D drawings. And after sanding, the part needed to be polished. Following the suggestion from Professor Fátima Vaz, two different varnishes for hardwood were tried. They were both applied on the first blades printed shown in Figure 2.1, but none of those brought satisfactory results. Then, acrylic wax was tried, which brought good results for the blade's finishing, and so it was applied on every part.

3

Experimental Setup and the Data Acquisition System

Contents

3.1 Experimental Setup

In this section the experimental setup used to proceed with the experiments is introduced. First, a description of the equipment involved is made, then the connections and the wiring layout are explained.

The experiment is performed inside the Aeroacoustic Wind Tunnel located in the Aerospace Engineering Laboratory of IST, presented in Figure 3.1.

Figure 3.1: Aeroacoustic Wind Tunnel present at the Aerospace Engineering Laboratory.

3.1.1 Equipment

The workbench used is the one mounted and tested by Amado [45], and it is shown in Figure 3.2(a). Amado studied coaxial rotors configurations, and, as such, this workbench has two Instrumented Tube (IT),1 and 2. For the present thesis, only one of the ITs will be needed, since each rotor will be tested separately. The IT measures the thrust and the torque produced by the rotor, which in turn is attached to the motor at the end of the tube, as is present in Figure 3.2(b).

For the experiment, the following equipment was used, where the citations refer to the components' datasheet and/or the user manual:

- **Computer** - A desktop computer with LabVIEW (the software used to run the tests and collect the data) installed and the necessary tool kits. It has $8GB$ of RAM and a processor Intel core i5 with $3.5GHz$ of maximum working frequency.
- **NI USB DAQ board NI9237** - A USB interface DAQ board with four channels of $24bit$ half/full-bridge analog input each. It reads in the range of $\pm 25mV/V$, with a maximum internal excitation up to $10V$. [49]

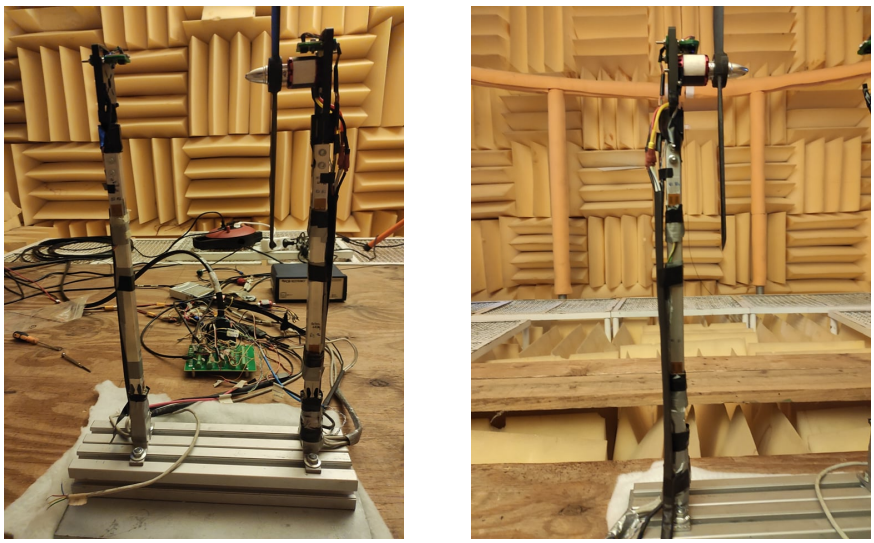

(a) The workbench.

(b) IT with the baseline rotor attached to the motor.

Figure 3.2: Workbench and the IT used.

- **DAQ board NI PCIe-6353** - The second DAQ device included in the setup. It has 16 differential or 32 single ended channels, offering analog I/O, digital I/O, four $32bit$ counters/timers for PWM, encoder, frequency, event counting, and more. This DAQ device is connected directly to the computer through a computer bus. [50]

- **Connector block NI CB-68LP board** - An auxiliary connection board that allowed to make the physical connections to the system. This board is an unshielded I/O accessory with 68 screw terminals. [51]

- **PCB Piezotronics 482C15 ICP Sensor Signal Conditioner** - The signal conditioner used to power the pre-polarized microphones. It has four channels (although only 3 are used in this case), and it amplifies the signal from the sensors, connecting them to the connector block. [52]

- **Power Supply** - A $2000W$ power supply, with an input of $220 - 240V$ and an output of $12 - 30V$ DC.

- **Cable Connector** - A 10 meters long NI custom shielded cable model SHC68-C68-D4, used for high-speed digital devices, which links the connector block to the PCIe-6353 DAQ board in the computer.

- **BLDC motor EMP N2830/13** - The motor used to attach and rotate the rotors. It has a maximum power of $300W$.

- **Sensors** -
  - Load transducers - The load transducers used are the Strain Gage (SG) 1-LY13-6/350, with a nominal resistance of 350Ω and a maximum effective bridge excitation voltage of $14V$.
  - Voltage sensor - The Pitlab voltage sensor, which also measures current, providing two analog voltage outputs: one for the current signal and the other for the voltage signal. [53]
  - Current sensor - The LTSR 25-NP current sensor. [54]
  - Temperature sensor - The LM35DZ sensor is positioned in order to monitor the temperature of the motors during the experiments. It has $5V$ of suitable supply voltage and a low absolute error. [55]
  - RPM sensor - The CNY70 is a reflective sensor which includes an infrared emitter and phototransistor output, that changes with the intensity of the reflected light. The rotation speed of the motor is read by the phototransistor, which detects the variation from the black and white tape taped around the motor. [56]
  - Microphones - 3 pre-polarized microphones from Brüel & Kjær - type 4958. These microphones have an excellent amplitude- and phase-matching for a wide range of temperature and humidity. [57]

Figure 3.3 presents most of the equipment just mentioned.

Following the introduction of the equipment used, the load transducers and the microphones are further described. To conclude this section, before introducing the DAQ system, the wiring layout is explained.

3.1.2 Load Transducers

A SG functions as a resistance that varies its value linearly with the elastic deformation experienced. However, a single SG has the disadvantage of being dependent on the surrounding temperature, changing the measuring grid electrical resistance when the temperature varies. So, to overcome this problem, the SGs are applied in a full bridge circuit configuration (or Wheatstone bridge).

A full bridge circuit uses four SGs, connected as a square wherein each side represents one SG. This type of circuit not only solves the temperature dependence of the SG but also increases the sensitivity and the accuracy of the measurements. Naming r_1 to r_4 the resistance of each SG in a full bridge, the bridge is excited by an excitation voltage U_E and has an output voltage U_A that varies with the SGs resistances according to equation 3.1

$$\frac{U_A}{U_E} = \frac{r_1 r_3 - r_2 r_4}{(r_1 + r_2)(r_3 + r_4)} \tag{3.1}$$

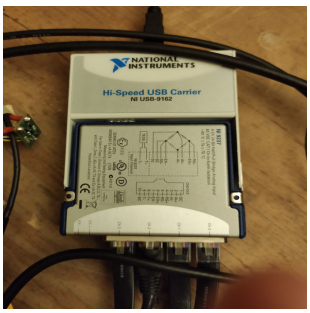

(a) USB DAQ board NI9237.

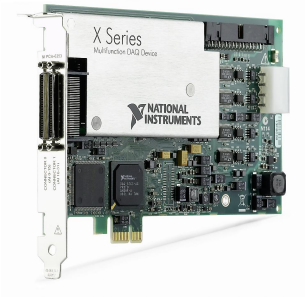

(b) DAQ board NI PCIe-6353.

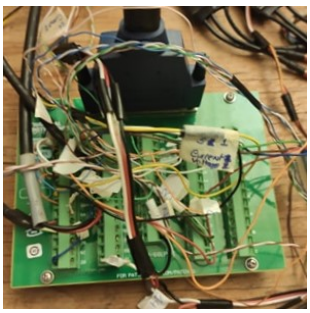

(c) Connector block.

(d) Signal conditioner.

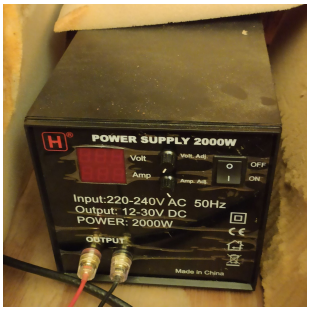

(e) Power supply.

(f) Motor.

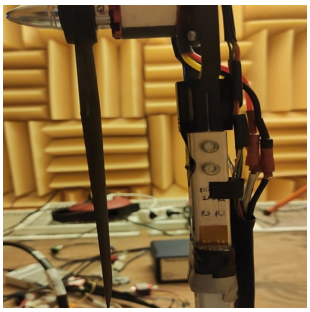

(g) Strain Gage.

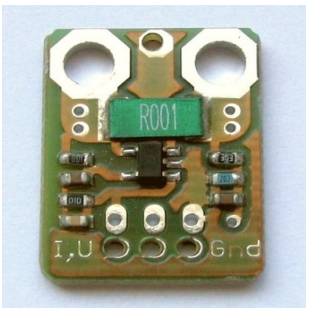

(h) Pitlab voltage sensor.

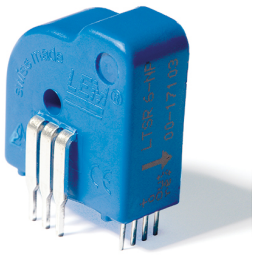

(i) Current sensor.

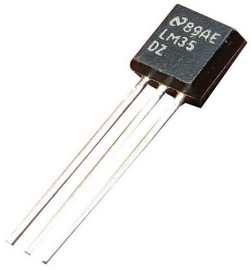

(j) Temperature sensor.

(k) RPM sensor.

(l) Brüel & Kjær - type 4958 microphone.

Figure 3.3: Equipment used during the experiment tests.

As was already mentioned, the workbench was mounted by Amado. The implementation of the full bridges on the IT was also done by Amado, and this implementation will now be explained.

The IT is a squared tube and it has 3 full bridges applied, which are represented in Figure 3.4. Considering the coordinate system shown in the figure, the rotor is expected to create a force and a torque in the XX direction, F_x and M_x.

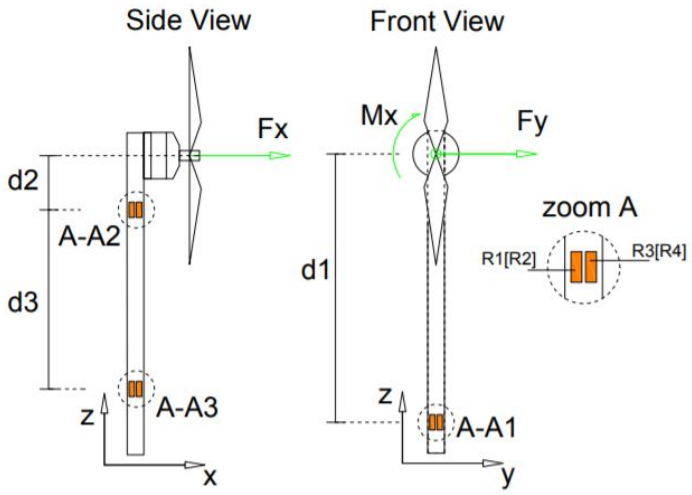

Figure 3.4: Scheme of the full bridges application points. Taken from [45].

F_x produces a bending moment M_y to the IT, while M_x produces bending to the faces of the tube which the normal is aligned with the YY direction. This latter bending can also be caused by a lateral force F_y due to misalignments in the structure. This means that to measure F_x only one full bridge is needed, $B1$, installed at the corresponding bending faces in the position A1. In turn, to measure the torque M_x, the bending produced by F_y must be decoupled from the bending produced by M_x. This decoupling is achieved by implementing two full bridges, $B2$ and $B3$, at the different positions A2 and A3, on the tube's faces that bend accordingly. This way, after performing the calibration, the F_x, F_y and M_x will be obtained independently.

3.1.3 Microphones

The Brüel & Kjær - type 4958 microphones are 1/4" pre-polarized, suitable for beamforming arrays requiring a large number of microphones. They have an excellent amplitude- and phase-matching, with an operating temperature range of -10 to $+55°C$ and an operating humidity range of 0% to $90\%RH$ without condensation. Their sensitivity is $11.2\ mV/Pa$, with an upper limit of dynamic range of $140\ dB$ and a maximum output voltage swing of $14\ V_{pp}$.

These microphones have a SMB coaxial plug as an output socket. Therefore, they are accompanied with BNC to SMB cables to link the microphones to the signal conditioners.

These microphones are good for free-field measurement conditions, where sound waves are free to expand forever from the source, without reflections or reverberations. Those conditions are obtained at large open areas free of reflective surfaces. For this reason, the microphones work best at the anechoic chamber, which is designed to cancel all sound reflections and reverberations, simulating a free-field. That way, the microphones measure sound pressure as it existed before they were introduced into the sound field.

3.1.4 Wiring Layout

In this wiring system there are two different DAQ boards being used: the USB NI9237 and the NI PCIe-6353. The USB NI9237 has four channels of $24bit$ full bridge analog input and it is connected to read the three voltage bridges output of the full bending bridges $B1$, $B2$ and $B3$ from the IT 1.

Apart from the bridges signals, all the other signals are received/transmitted by the NI PCIe-6353 DAQ board. The physical connections are made through the NI CB-68LP connector block, which in turn is linked to the NI PCIe-6353 by the cable connector SHC68-C68-D4. Figure 3.5(a) presents a diagram of the connector block, in which is shown the screw terminals and the 68-Pin I/O to where the cable connector is attached . Figure 3.5(b) shows all the wiring connections between the connector block and the other components. The signals are all in differential mode, where the input signals (in red and yellow) are all coming from the sensors and the single output signal (in green and black) is sent to control the motor. The RPM sensor, the temperature sensor and the current sensor LTRS are powered by the power supply (blue links). The brown links represent the wires used to short-circuiting.

Table 3.1 provides a more detailed description of where to link each wire.

Table 3.1: Connections between sensors and the PCIe-6353/CB-68LP terminals.

Input/Output Signal		
Ch0	Voltage VS	CH+ 68/white wire; CH- 34/black wire
Ch1	Temperature TS	CH+ 33/blue wire; CH- 66 or 34/white-orange wire; +5V 8/white-blue wire
Ch2	Current VS	CH+ 65/yellow wire; CH- 31 or 34/black wire
Ch3	Microphone 0	CH+ 30/red wire; CH- 63/white wire
Ch4	RPM RS	CH+ 28/blue wire (E1) output; CH- 61/red+orange wires (E2/K); +5V 14/green (A) and white-brown (C)
Ch5	Microphone 2	CH+ 60/red wire; CH- 26/white wire
Ch6	Current IS	CH+ 25/green(V_{Out}); CH- 58/white-orange wire; +5V 8/orange wire
Ch7	Microphone 1	CH+ 57/red wire; CH- 23/black wire
ESC	PWM output	a1 21/white wire; 54GND/black wire

Table 3.2 presents the connections made between the microphones, the signal conditioner and the connector block. Each microphone is accompanied by a SMB to BNC cable to connect it to one of the four channels of the signal conditioner. The microphone signal is amplified inside the signal conditioner and transmitted to the connector block through a RG-58 coaxial cable. The signal conditioner is set to amplify the microphone signal 100x, as is both recommended by the microphones manual [57] and

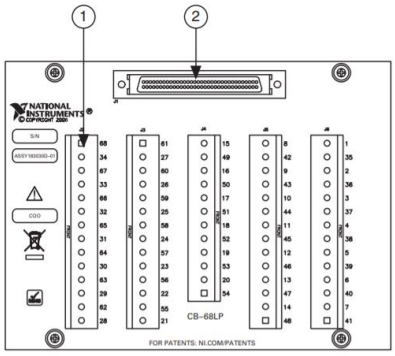

(a) NI CB-68LP parts locator diagram. **1** - Screw terminals; **2** - 68-Pin I/O Connector. Taken from [51].

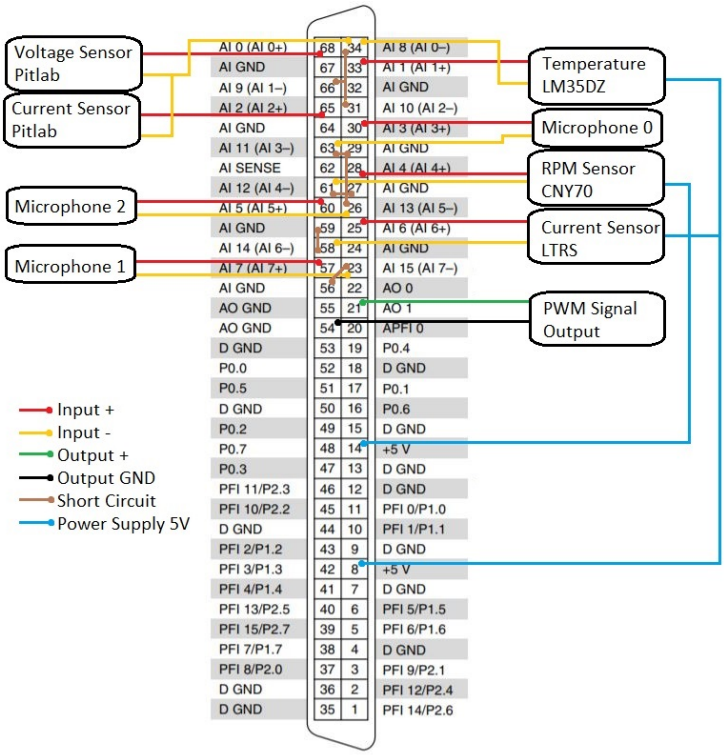

(b) Wiring connections to the PCIe-6353/CB-68LP terminals. **AI** - Analog Inputs; **AO** - Analog Outputs; **+5V terminal**- supply voltage to the sensors. **PFI lines** - Programmable Function Interface (Digital). Adapted from [50].

Figure 3.5: Schematic of the CB-68LP connector block and the NI PCIe-6353 pinout.

Francisco Pereira [58], the first student to implement a sound measuring system in the aeroacoustic wind tunnel of IST. The procedure to operate with the signal conditioner is described in Appendix B.

Table 3.2: Connections between the microphones, the signal conditioner and the connector block.

Microphone	Signal Conditioner [Channel]	Pinout connections
Mic0	Channel 2	(+) 30 [AI 3 (AI 3 +)] (-) 63 [AI 11 (AI 3 -)]
Mic1	Channel 3	(+) 57 [AI 7 (AI 7 +)] (-) 23 [AI 15 (AI 7 -)]
Mic2	Channel 4	(+) 60 [AI 5 (AI 5 +)] (-) 26 [AI 13 (AI 5 -)]

3.2 Data Acquisition System - LabVIEW

The present section presents the LabVIEW programs used to measure and record the data.

3.2.1 Noise Measurement system

The microphones read the sound waves, turning them into an electric signal. This signal is amplified in the signal conditioner and reaches the computer through one of the DAQ devices. The computer, by using the LabVIEW software, reads, records and processes the microphones signal. The LabVIEW program used to evaluate the noise in this thesis was adapted from the one created by Pereira [58].

This program was first created to evaluate the sound inside the wind tunnel. The microphones would be placed as in a beamforming array, the wind tunnel would be functioning and the sound produced by the flow would be analyzed. However, to study the sound from a rotor attached to the workbench, the program cannot only read the signals coming from the microphones, but it also needs to interact with the workbench, in particular with the motor and with the RPM sensor. So, the initial program was adapted and it was included a throttle control to the motor to vary the rotation speed. Furthermore, it was added a system to clear the previous data collected and restart all acoustic operations to allow changing the rotation speed between tests. Summarily, the acoustic operations performed to the data collected from each microphone are listed in the following:

- A Fast Fourier Transform to convert the results from a time domain to a frequency domain, providing the variation of SPL with frequency;
- A One-third Octave bands grouping of the SPL;
- A calculation of the Leq;
- A calculation of the total band power.

The voltage signal produced in the microphones varies in frequency and amplitude over time. So, the voltage needs to be converted to pressure units, in this case to $Pascal$, and the acoustic operations mentioned will all depend on how the signal is analysed.

According to Nyquist's sampling theorem [59], the sampling rate must be higher than at least two times the maximum frequency intended to record. Following the interval of frequencies captured by human hearing, which is from $20Hz$ to $20000Hz$, the sampling rate must be higher than $40000Hz$. However, the recommended value is five times the maximum frequency, so the sampling rate was set to $100000Hz$. The number of samples was set to 50000, with a collection time of 30 seconds per test.

The Fast Fourier Transform was applied using a Hanning window, with a number of averages of 1000, RMS averaging mode and linear weighting. It converts the data to SPL over frequency, enabling to study

and compare the noise from the rotors for different frequencies. The SPL is related to the pressure of the sound waves according to equation 3.2, where the reference pressure is $p_{ref} = 2 \times 10^{-5} Pa$.

$$SPL = 20 \log_{10} \left(\frac{p_{rms}}{p_{ref}} \right) \ [dB] \tag{3.2}$$

The one-third octave bands group the SPL in bands of frequency similar to how the human hearing distinguishes frequencies. This grouping is easier to interpret than the graphs showing the SPL, making it an important tool to compare the noise from many different rotors.

The Leq gives the steady sound level which has the same total energy of a fluctuating noise over a period of time. It is an important concept to assess the sound energy during a time interval, and it is calculated by equation 3.3.

$$Leq = 10 \log_{10} \left(\frac{1}{t_f - t_i} \int_{t_i}^{t_f} \left(\frac{p}{p_{ref}} \right)^2 dt \right) \ [dB] \tag{3.3}$$

The total band power provides an overall value of the SPL, which may be interesting to compare between rotors.

An important option available in the LabVIEW program used is to apply a weighting filter, as A-weighting, B-weighting, C-weighting or no weighting filter. The A-weighting filter was used in the tests, for it highlights the frequencies to which the human hearing is more sensitive to.

3.2.2 Loads Measurement system

The LabVIEW program used to measure and record the loads was the one created and used by Amado. In her case, to study the coaxial configuration she used both ITs from the workbench, collecting simultaneously the bridges output, thrust, torque, figure of merit, motor temperature and rotation speed. In the present thesis only one IT is used, so the data collected is the same but just for that IT. Although the program calculated instantly the forces, the torque and the figure of merit, it was decided to only record the bridges output data and to calculate those quantities separately outside the LabVIEW environment.

Just as in the noise measurement system, a throttle control to the motor is included to vary the rotation speed as intended. Figure 3.6 displays the control panel of the program used, where the sampling rate is $10000 Hz$ and the number of samples to average is 1000.

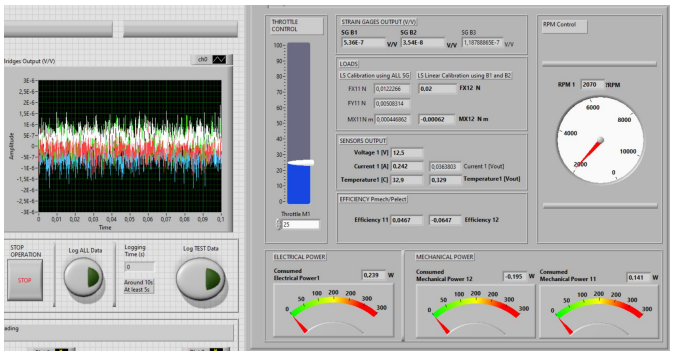

Figure 3.6: Control panel of the loads LabVIEW program.

3.3 Calibration

Before proceeding with the experiment, the sensors need to be calibrated to ensure the results taken are trustworthy. So, the present section presents the microphones and the load transducers calibration procedure.

3.3.1 Microphones Correction

Starting off with the microphones, these are not calibrated in the true meaning of the word, for a microphone calibrator is not used upon them. Instead, the microphones suffer a correction to the results they provide in the LabView program. By changing slightly the gain of each microphone, it was possible to approximate their sensitivity to the same noises emitted.

As it was already mentioned, the experiments take place in the Aeroacoustic Wind Tunnel at the Aerospace Engineering Laboratory, with a built-in Anechoic Chamber. Figure 3.7(a) shows one side of the anechoic chamber, marking the position of the three microphones used in relation to the IT and the rotor installed. Figure 3.7(b) represents a top view schematic of the chamber. Each microphone distances $2.3\ m$ from the rotor, with Microphone 0 angled $45°$ from the rotor plane to the wake side, Microphone 1 aligned with the rotor plane and Microphone 2 angled $45°$ from the rotor plane to the suction side.

To perform the microphones corrections, first it was emitted pure tone noise signals to check what was read. Using an App on the cellphone, with it working as a loud speaker, it was possible to select a single frequency to produce the pure tone noise.

Four different tests were run, each for one of the pure tones used: $500Hz$, $1000Hz$, $2500Hz$ and $5000Hz$. Figure 3.8 shows the intensity graphs obtained from these tests, confirming that the microphones were reading the intended frequencies correctly. Apart from the brighter blue line, there are a few less visible blue lines in the first three graphs. These lines correspond to frequencies that are multiple of the pure tone emitted, for example in Figure 3.8(c) the intended frequency perfectly matches

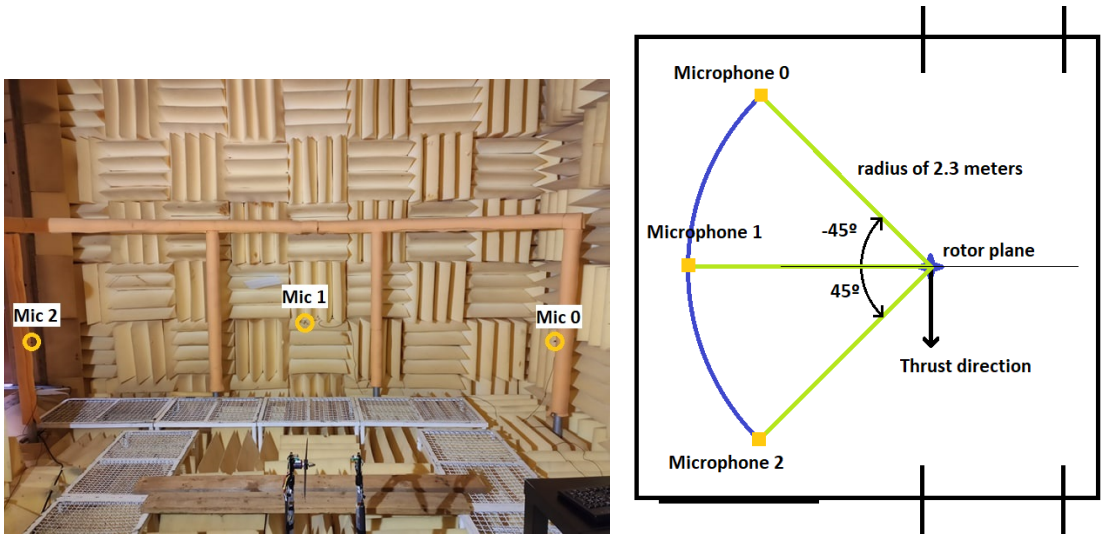

(a) Microphones positioning. **(b)** Top view schematic.

Figure 3.7: The microphones positions in the anechoic chamber.

the bright blue line at $2500Hz$, but then there is a second blue line, much less visible, at the frequency of $5000Hz$. This means that the cellphone and App used as a speaker also emitted noise with frequencies that are multiple of the pure tones, with much less intensity, but enough for the microphones to pick up.

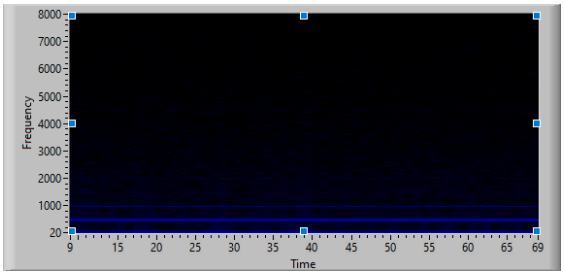

(a) Pure tone of 500 Hz.

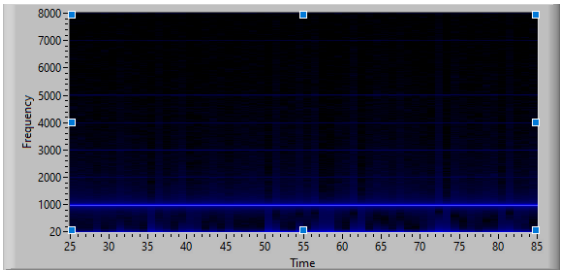

(b) Pure tone of 1000 Hz.

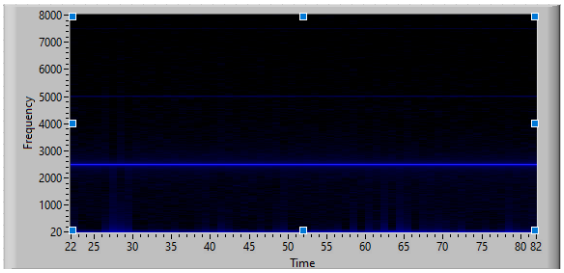

(c) Pure tone of 2500 Hz.

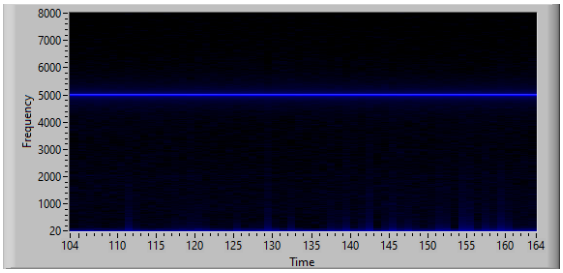

(d) Pure tone of 5000 Hz.

Figure 3.8: Intensity graphs relative to the different frequencies of the noise emitted.

Figure 3.9 presents the measured SPL, by the three microphones, for each of the pure tone tests. In these graphs is also noticeable that the microphones read clearly the intended frequencies, and with smaller SPL the frequencies multiple of the pure tone ones. However, the microphones do not read the exact same SPL values in the peaks, indicating that the microphones sensitivity is not exactly the same and that it should be properly adjusted. Noise results from different microphones can only be compared, to study the noise directionality, if they are equally sensible to begin with.

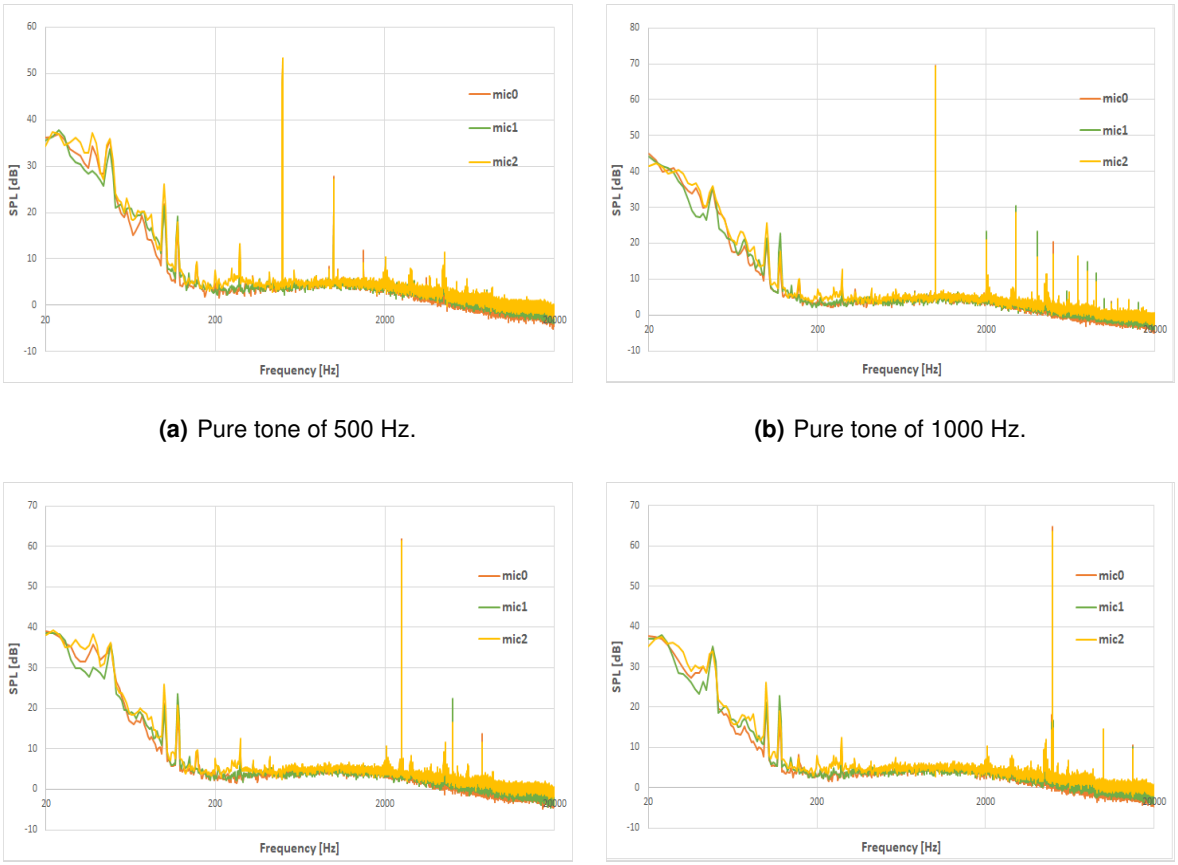

(a) Pure tone of 500 Hz.

(b) Pure tone of 1000 Hz.

(c) Pure tone of 2500 Hz.

(d) Pure tone of 5000 Hz.

Figure 3.9: SPL measured by the three different microphones during the pure tone tests.

Figure 3.10(a) demonstrates the difference in readings between the three microphones, where the Leq value is shown for the four pure tone tests. To correct the microphones readings, an average of the Leq values was calculated, and the gain to the microphones signal was adjusted to meet that average value. The averaged Leq taken into consideration was the one from the $1000Hz$ pure tone test. After adjusting the gain the first time, this procedure was repeated two more times in order to further approximate the microphones readings.

Figure 3.10(b) shows the Leq values obtained in the pure tone tests repeated after adjusting the gain

values. Apart from the $500Hz$ test, the microphone readings became all much closer together.

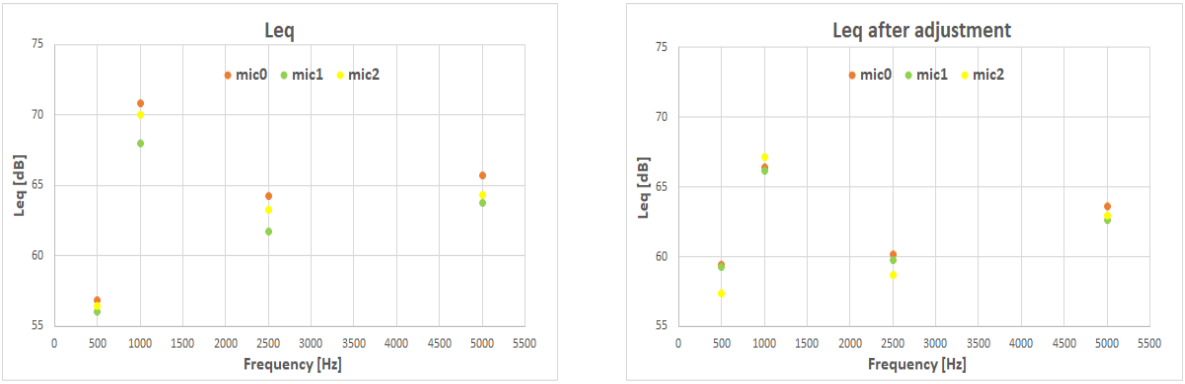

(a) Before the corrections.

(b) After the corrections.

Figure 3.10: Leq of the different microphones, in the pure tone tests, before and after the microphones corrections.

In the LabView program, the initial pregain setting is set to $40\ dB$, as is the recommended default. After the microphones corrections, the pregain values used are the ones presented in Table 3.3

Table 3.3: Microphones pregain values.

	Inital pregain	Final pregain
Mic0	40.0 dB	40.1 dB
Mic1	40.0 dB	39.9 dB
Mic2	40.0 dB	40.6 dB

3.3.2 Load Transducers Calibration

3.3.2.1 Calibration Configurations

The load transducers calibration was performed by manually applying a set of known weights to the IT. Then, by checking the voltage the SG bridges were reading, a correlation between the forces applied and the readings was made. This method was also used by Amado, where the mathematical model is fully described by Leung and Link [60].

The application of the weights was done in sequences of static sets of loading, and then unloading, weights, done in both the positive and negative directions of the forces and moment intended to study. In this case, and continuing with the coordinate system shown in Figure 3.4, they are the forces in the XX (normal force) and YY (lateral force) directions, and the moment in the XX direction. So, there are 3 parameters to calibrate.

In this calibration procedure, pure loads were applied to each of the parameters of interest. A pure load is a load (either force or torque) perfectly aligned with the axis or direction intended to study. That

way, the pure load will only load in that direction, without any load component in any other direction. By using pure loads, the forces are decoupled, and, although F_y and M_x are inherently coupled, the algebraic operations, that will be explained later in this section, are simpler to solve and produce better results. In the end there will be a coefficient matrix for each of the calibrated parameters, and this way each matrix will be more accurate towards the parameter that it is calibrated to.

The loading process was accomplished by turning the workbench, with the help of a small table and some clamps, checking the IT level with a bubble level, and attaching the weights with a string (and a pulley when needed), making sure that everything is perfectly aligned as intended. Figure 3.11 demonstrates how the loading occurred for F_x, F_y and M_x, described in the following points:

- In loading in the XX direction, the IT was positioned horizontally with the motor screw pointing downwards. A string was tied around the screw and, in case of the negative loading, a pulley was used.

- In loading in the YY direction, the IT was positioned horizontally with the motor facing sideways. Again, a string was tied to the screw, and, in the positive loading, a pulley was used.

- In the moment M_x loading, with the workbench on the ground, the motor was detached and in its place was fixed a small bar with holes. With the center of the bar aligned with the center of the motor position, the holes would distance $5\ cm$ from the IT center, acting as a moment arm when loading vertically one of the holes.

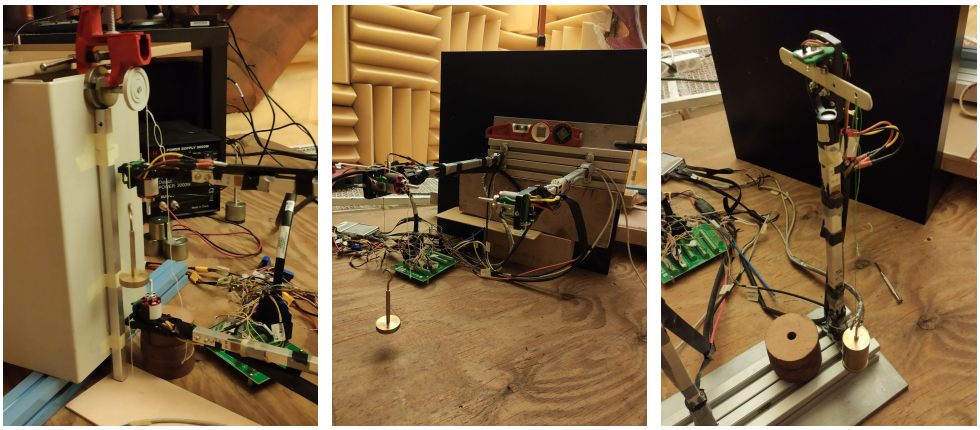

(a) Loading in the XX direction.

(b) Loading in the YY direction.

(c) Pure moment M_x loading.

Figure 3.11: F_x, F_y and M_x calibration.

3.3.2.2 Loading Process

The weights were chosen in order to include and overestimate the test load ranges expected from the experimental tests. Therefore, the forces F_x and F_y were calibrated with loads up to a maximum of $14N$, whereas the torque M_x was calibrated with a moment up to $0.3N.m$. To sum up, each calibration sequence has a number of sets $N = 154$, consisting of loading and unloading of weight in the negative and positive XX and YY directions, and loading and unloading of pure moment in the negative and positive XX direction. Table 3.4 presents the loading order used in each calibration sequence, thus forming the loading matrix $\boldsymbol{Y}_{applied}$. The sets 1 to 58 represent the loading in the XX direction, then from 59 to 116 the loading in the YY direction, and the last sets from 117 to 154 the pure moment in the XX direction.

Table 3.4: The total loading matrix $\boldsymbol{Y}_{applied}$ [$N \times m$], containing the calibration loads applied.

Set No.	F_x $[10^{-3}N]$	F_y $[10^{-3}N]$	M_x $[10^{-3}N.m]$	**Set No.**	F_x $[10^{-3}N]$	F_y $[10^{-3}N]$	M_x $[10^{-3}N.m]$	**Set No.**	F_x $[10^{-3}N]$	F_y $[10^{-3}N]$	M_x $[10^{-3}N.m]$
1	0	0	0	**59**	0	0	0	**117**	0	0	0
2	-99.05	0	0	**60**	0	-99.05	0	**118**	0	0	-4.952
...	⋮	⋮	⋮	**...**	⋮	⋮	⋮	**...**	⋮	⋮	⋮
15	-14133.4	0	0	**73**	0	-14133.4	0	**126**	0	0	-310.04
...	⋮	⋮	⋮	**...**	⋮	⋮	⋮	**...**	⋮	⋮	⋮
31	99.05	0	0	**89**	0	99.05	0	**137**	0	0	4.952
...	⋮	⋮	⋮	**...**	⋮	⋮	⋮	**...**	⋮	⋮	⋮

The loading matrix is dimensioned [$N \times m$], considering $m = 3$ the number of parameters to be fitted, and the number of calibration sequences performed is $n = 3$.

The masses of the weights used were measured with a precision balance with a resolution of $0.01g$ and an accuracy of $\pm 0.05g$, being $g = 9.80665m/s^2$ the acceleration due to gravity. The uncertainties regarding the normal and lateral forces are accounted as $u_F = g \times u_{mass}$, where u_{mass} is the uncertainty regarding the mass measurement that has a base value of $0.00001Kg$ (which is associated with the balance resolution). The uncertainty regarding the moment is estimated using the propagation law of uncertainty $u_M = \sqrt{\Delta l^2 u_{M_x}^2 + M_x^2 u_{\Delta l}^2}$, where Δl is the moment arm, $u_{\Delta l} = 0.001m$ is the uncertainty due to the arm distance and u_{M_x} is the uncertainty of the applied M_x. In the present study, the uncertainty regarding the acceleration due to gravity was neglected.

3.3.2.3 Strain Gages Readings

From applying a calibration sequence, the results from the voltage outputs at the bridges are taken. Table 3.5 presents those values, as R_i', for the second calibration sequence performed. R_1' is respective to the full bending bridge for F_x $B1$, while R_2' is to the full bending bridge for M_x $B2$ and $R'3$ is to the auxiliary full bending bridge for M_x $B3$.

Table 3.5: The voltage bridges output, as R'_i, and the respective difference, as R_i.

Set No.	R'_1 $[mV]$	R'_2 $[mV]$	R'_3 $[mV]$	R_1 $[mV]$	R_2 $[mV]$	R_3 $[mV]$
1	0.208641	0.0630883	-0.0347455	0	0	0
2	0.204381	0.063061	-0.034787	-0.00425964	-2.72481E-5	-4.14676E-5
3	0.196116	0.063028	-0.0349064	-0.0125255	-6.03229E-5	-1.60935E-4
4	0.153983	0.0631413	-0.0352793	-0.0546579	5.30368E-5	-5.33842E-4
5	0.110764	0.0632182	-0.0356444	-0.0978772	1.29918E-4	-8.98913E-4
⋮	⋮	⋮	⋮	⋮	⋮	⋮
154	0.133162	0.0574015	-0.0413267	-1.72433E-4	2.47473E-4	1.44497E-4

These values of R'_i are directly connected to the strain experienced by the SGs, which may not be that accurate considering that in the calibration configurations the IT is in different positions in comparison to the natural one, the motor is taken out in the M_x loading, and even the room temperature may vary with time. All these are examples of factors that influence the strain in the SG. So, to overcome these factors and reach a more accurate calibration, instead of using the voltage bridges output, it was used the difference between the voltage bridges output and the voltage bridges output recorded at the beginning of every test, presented as R_i in the table. For instance, the sets related with the F_x loading are subtracted the voltage bridges output values recorded at the beginning of the loading in the XX direction, then the sets related with the F_y loading are subtracted the voltage bridges output values recorded at the beginning of the loading in the YY direction, and so on for the M_x. This way, the variation of the strain is calibrated rather than the strain itself. Figure 3.12 shows the values of R for the bridges $B1$, $B2$ and $B3$ when loading and unloading in the negative way (-) and in the positive way(+).

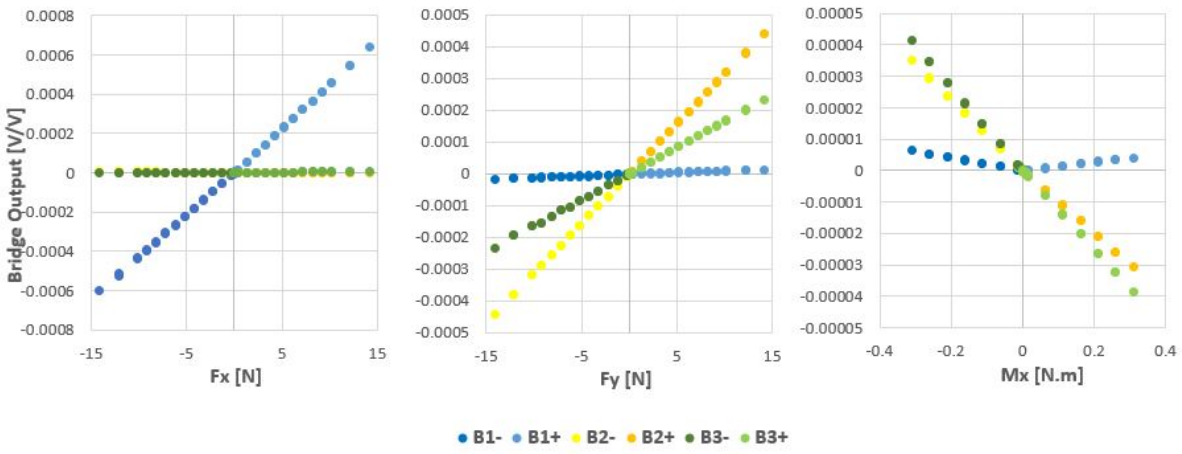

Figure 3.12: Output bridge voltage difference values, for the $\pm F_x$, $\pm F_y$ and $\pm M_x$ loading and unloading sets.

In the F_x loading sets, $B1$ is the only bridge evidencing variation, proving that F_x is decoupled from F_y and M_x. From the F_y and M_x loading sets, $B2$ and $B3$ vary significantly, showing that the lateral force and the moment in the rotor plane are coupled. However, in the M_x loading sets, the order of

magnitude of the variation of voltage bridges output is at least 10 times smaller than the R recorded in the two other types of loading sets. For that reason, in the M_x graph a small variation of the R recorded in bridge $B1$ is noticeable.

3.3.2.4 Calibration - The Weighted Least Squares Method

The method used for the calibration is the Weighted Least Squares one, which is simplified in the diagram of Figure 3.13. This method is further explained following the figure.

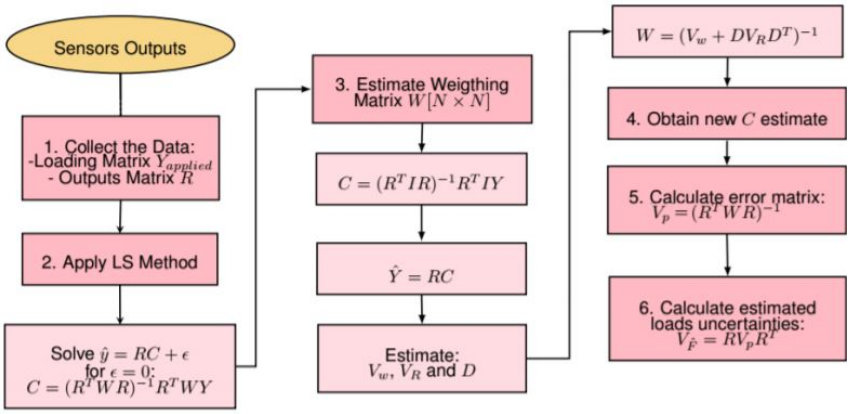

Figure 3.13: Diagram sequence of the calibration method. Taken from [45].

Collecting the Data - Three calibration sequences are performed, collecting the voltage bridges output $\{R'_1; R'_2; R'_3\}$ in every set and converting them to $\{R_1; R_2; R_3\}$, thus forming one matrix $\boldsymbol{R}$ $[N \times m]$ per calibration sequence. The average of the three matrices is then calculated in $\boldsymbol{R}_{average}$ $[N \times m]$. All the while, the loading combinations are known for each set, so the loading matrix $\boldsymbol{Y}_{applied}$ $[N \times m]$ is also known.

Applying the Least Squares Method - The objective of the calibration is to be able to solve the system presented in equation 3.4, where $\boldsymbol{Y}$ is the matrix of the aerodynamic forces and moment, $\boldsymbol{C}$ is the calibration coefficients matrix and $\boldsymbol{\epsilon}$ is the estimated calibration error. In this case, the rows of each matrix simply correspond to different loading conditions.

$$\boldsymbol{Y} = \boldsymbol{RC} + \boldsymbol{\epsilon} \tag{3.4}$$

By executing the calibration loading procedure, N sets of conditions are created wherein the $\boldsymbol{Y}$ and the $\boldsymbol{R}$ are known.

As a first iteration, the calibration error $\boldsymbol{\epsilon}$ is neglected and the calibration procedure is considered ideal in the terms that there are no uncertainties regarding the loading and reading parts. Therefore, a

first estimation of the calibration coefficients matrix $\boldsymbol{C'}$ is obtained through equation 3.5, where $\boldsymbol{I}$ is the identity matrix.

$$\boldsymbol{C'} = \left(\boldsymbol{R}_{average}^{T}\boldsymbol{I}\boldsymbol{R}_{average}\right)^{-1}\boldsymbol{R}_{average}^{T}\boldsymbol{I}\boldsymbol{Y}_{applied} \tag{3.5}$$

Weighting Estimation - The first iteration is an important step because it approaches the calibration to satisfying results. However, the calibration matrix can, and should, be further improved. So, with that objective in mind, a weighting estimation is applied. The results are associated with uncertainties due to random errors in the manual procedure, and those uncertainties introduce variability in the information gathered, which will now be accounted. This step improves the statistical assessment of the data, making the results more reliable.

Equation 3.6 introduces the weighting matrix $\boldsymbol{W}_i$, said matrix that accounts with the uncertainties concerning the applied loads and other errors in the measurement procedure, such as the alignment of the loads and the uncertainties in the bridges outputs. One weighting matrix is estimated per parameter to be calibrated (F_x, F_y and M_x), thus having an index $i = 1, 2, 3$.

$$\boldsymbol{W}_i = \left(\boldsymbol{V}_W + \boldsymbol{D}_i\boldsymbol{V}_R\boldsymbol{D}_i^{T}\right)^{-1} \tag{3.6}$$

The calculation of $\boldsymbol{W}_i$ requires the calculation of three other matrices, which will now be addressed one by one. The matrix $\boldsymbol{V}_W$ accounts with the errors of the loading procedure in the calibration sequences. After calculating the first iteration, the estimated loading matrix $\hat{\boldsymbol{Y}}$ can be obtained by solving the initial system $\hat{\boldsymbol{Y}} = \boldsymbol{R}_{average}\boldsymbol{C'}$. With it, the standard deviation of the fitting σ_i is calculated through equation 3.7.

$$\sigma_i^2 = \frac{1}{N-m}\sum_{p=1}^{N}\left(y_{applied_{p,i}} - \hat{y}_{p,i}\right)^2 \tag{3.7}$$

Having the standard deviation of the fitting, the total uncertainty σ_{tot_i} is then calculated for each of the parameters to be fitted. This σ_{tot_i} accounts with two different parcels: the first from the estimation of errors due to cable misalignments and other human errors - considered to be equal to the standard deviation of the fitting; the second from the uncertainty of the weights, already approached in the present section. Therefore, $\sigma_{tot_i} = \sqrt{\sigma_i^2 + u_i^2}$, and for each of the parameters to be fitted it follows as: $\sigma_{tot_1} = \sqrt{\sigma_1^2 + u_{F_x}^2}$; $\sigma_{tot_2} = \sqrt{\sigma_2^2 + u_{F_y}^2}$; $\sigma_{tot_3} = \sqrt{\sigma_3^2 + u_{M_x}^2}$.

After the total uncertainty of the loading procedure is estimated, $\boldsymbol{V}_W$ can be calculated, presented in equation 3.8. $\boldsymbol{V_W}$ is a diagonal matrix [$N \times N$] composed by smaller diagonal matrices, each one corresponding to each parameter to be fitted and of dimensions equal to the number of calibration sets relative to that parameter.

$$\boldsymbol{V_W} = \begin{bmatrix} \begin{bmatrix} \sigma^2_{tot_1} & & \\ & \ddots & \\ & & \sigma^2_{tot_1} \end{bmatrix} & & & \\ & \begin{bmatrix} \sigma^2_{tot_2} & & \\ & \ddots & \\ & & \sigma^2_{tot_2} \end{bmatrix} & & \\ & & \begin{bmatrix} \sigma^2_{tot_3} & & \\ & \ddots & \\ & & \sigma^2_{tot_3} \end{bmatrix} & \\ & & & \end{bmatrix}_{[N \times N]} \tag{3.8}$$

The matrix $\boldsymbol{V_R}$ is related to the uncertainties in the bridge readings. This matrix takes into account the values obtained from the repetition of the calibration sequences, performed under the same conditions and over a short period of time, thus being dimensioned $[3N \times 3N]$. The off-diagonal elements correspond to the covariances between the readings of the load transducers, and the diagonal ones correspond to the variances between the readings of the load transducers.

$$\boldsymbol{V}_R = \begin{bmatrix} u(r_{1,1}, r_{1,1}) & u(r_{1,1}, r_{2,1}) & \cdots & u(r_{1,1}, r_{N,1}) & u(r_{1,1}, r_{1,2}) & \cdots & u(r_{1,1}, r_{N,3}) \\ u(r_{2,1}, r_{1,1}) & u(r_{2,1}, r_{2,1}) & \cdots & u(r_{2,1}, r_{N,1}) & u(r_{2,1}, r_{1,2}) & \cdots & u(r_{2,1}, r_{N,3}) \\ \vdots & \vdots & \ddots & \vdots & \vdots & \ddots & \vdots \\ u(r_{N,1}, r_{1,1}) & u(r_{N,1}, r_{2,1}) & \cdots & u(r_{N,1}, r_{N,1}) & u(r_{N,1}, r_{1,2}) & \cdots & u(r_{N,1}, r_{N,3}) \\ u(r_{1,2}, r_{1,1}) & u(r_{1,2}, r_{2,1}) & \cdots & u(r_{1,2}, r_{N,1}) & u(r_{1,2}, r_{1,2}) & \cdots & u(r_{1,2}, r_{N,3}) \\ \vdots & \vdots & \ddots & \vdots & \vdots & \ddots & \vdots \\ u(r_{N,3}, r_{1,1}) & u(r_{N,3}, r_{2,1}) & \cdots & u(r_{N,3}, r_{N,1}) & u(r_{N,3}, r_{1,2}) & \cdots & u(r_{N,3}, r_{N,3}) \end{bmatrix}_{[3N \times 3N]} \tag{3.9}$$

The covariances and variances are computed using another matrix, named $\boldsymbol{R}_{global}$, which is presented in equation 3.10. This matrix is dimensioned $[3N \times n]$, where n corresponds to the number of calibration sequences performed. The first column is obtained by rearranging the matrix $\boldsymbol{R}$ measured in the first calibration sequence by stacking its three different columns (corresponding to $B1$, $B2$ and $B3$) one on top of the other. The second and third columns of $\boldsymbol{R}_{global}$ are obtained in the same way as the first, but using the $\boldsymbol{R}$ matrices from the second and third calibration sequences, respectively.

$$\boldsymbol{R}_{global} = \begin{bmatrix} 1 & \rightarrow & n \\ \begin{Bmatrix} 1 \\ \vdots \\ N \end{Bmatrix} & R_1 & \\ \begin{Bmatrix} 1 \\ \vdots \\ N \end{Bmatrix} & R_2 & \\ \begin{Bmatrix} 1 \\ \vdots \\ N \end{Bmatrix} & R_3 & \end{bmatrix}_{[3N \times n]} \tag{3.10}$$

The final matrices needed to finish the calculation of the weighting matrix are the sensitivity coefficients matrices $\boldsymbol{D}_i$, dimensioned $[N \times 3N]$, whose elements correspond to the calibration coefficients in $\boldsymbol{C}'$ calculated in the first iteration. By presenting equation 3.4 in an indicial notation, it follows as: $y_i = \sum_{j=1}^{n} r_j c_{j,i} + \epsilon_i$. As such, $\boldsymbol{D}_i$ are calculated as in equation 3.11.

$$\boldsymbol{D}_i = \begin{bmatrix} \frac{\partial y_{1,i}}{\partial r_{1,1}} & \frac{\partial y_{1,i}}{\partial r_{2,1}} & \cdots & \frac{\partial y_{1,i}}{\partial r_{N,1}} & \frac{\partial y_{1,i}}{\partial r_{1,2}} & \cdots & \frac{\partial y_{1,i}}{\partial r_{N,3}} \\ \frac{\partial y_{2,i}}{\partial r_{1,1}} & \frac{\partial y_{2,i}}{\partial r_{2,1}} & \cdots & \frac{\partial y_{2,i}}{\partial r_{N,1}} & \frac{\partial y_{2,i}}{\partial r_{1,2}} & \cdots & \frac{\partial y_{2,i}}{\partial r_{N,3}} \\ \vdots & \vdots & \ddots & \vdots & \vdots & \ddots & \vdots \\ \frac{\partial y_{N-1,i}}{\partial r_{1,1}} & \frac{\partial y_{N-1,i}}{\partial r_{2,1}} & \cdots & \frac{\partial y_{N-1,i}}{\partial r_{N,1}} & \frac{\partial y_{N-1,i}}{\partial r_{1,2}} & \cdots & \frac{\partial y_{N-1,i}}{\partial r_{N,3}} \\ \frac{\partial y_{N,i}}{\partial r_{1,1}} & \frac{\partial y_{N,i}}{\partial r_{2,1}} & \cdots & \frac{\partial y_{N,i}}{\partial r_{N,1}} & \frac{\partial y_{N,i}}{\partial r_{1,2}} & \cdots & \frac{\partial y_{N,i}}{\partial r_{N,3}} \end{bmatrix}_{[N \times 3N]} \tag{3.11}$$

Noting that only the sensitivity coefficients whose second subscripts match correspond to the same loading conditions, all other elements are equal to zero, and therefore the matrix is reduced as in equation 3.12.

$$\boldsymbol{D}_i = \begin{bmatrix} \frac{\partial y_{1,i}}{\partial r_{1,1}} & 0 & \cdots & 0 & \frac{\partial y_{1,i}}{\partial r_{1,2}} & \cdots & 0 \\ 0 & \frac{\partial y_{2,i}}{\partial r_{2,1}} & \cdots & 0 & 0 & \cdots & 0 \\ \vdots & \vdots & \ddots & \vdots & \vdots & \ddots & \vdots \\ 0 & 0 & \cdots & 0 & 0 & \cdots & 0 \\ 0 & 0 & \cdots & \frac{\partial y_{N,i}}{\partial r_{N,1}} & 0 & \cdots & \frac{\partial y_{N,i}}{\partial r_{N,3}} \end{bmatrix}_{[N \times 3N]} \tag{3.12}$$

Final Calibration Coefficient Matrices - Having the weighting matrices computed, the final calibration coefficients matrices $\boldsymbol{C}_i$ can finally be obtained. These are calculated through the second iteration, presented in equation 3.13.

$$\boldsymbol{C}_i = \left(\boldsymbol{R}_{average}^T \boldsymbol{W}_i \boldsymbol{R}_{average}\right)^{-1} \boldsymbol{R}_{average}^T \boldsymbol{W}_i \boldsymbol{Y}_{applied} \tag{3.13}$$

The calibration is complete and the fitted parameters are calculated as the system of equations 3.14 demonstrates. In the end, there are three different calibration coefficients matrices, each responsible for the respective fitted parameter.

$$\begin{cases} y_1 = F_x = c_{1,1}R_1 + c_{2,1}R_2 + c_{3,1}R_3 \; with \; c \; from \; \boldsymbol{C}_1 \\ y_2 = F_y = c_{1,2}R_1 + c_{2,2}R_2 + c_{3,2}R_3 \; with \; c \; from \; \boldsymbol{C}_2 \\ y_3 = M_x = c_{1,3}R_1 + c_{2,3}R_2 + c_{3,3}R_3 \; with \; c \; from \; \boldsymbol{C}_3 \end{cases} \tag{3.14}$$

As a final verification, the loads applied, as $\boldsymbol{Y}$, are calculated using these calibration matrices, and then compared to the loading applied in the calibration sets. Figure 3.14 shows the loading values and the forces and torque estimated through the calibrated system of equations. Remembering that

one calibration sequence has 154 sets, from which 58 correspond to F_x loading, another 58 sets to F_y loading and the final 38 sets to M_x loading, the estimated results match very well the loading applied for the three parameters.

Concerning the torque calculation, there are some perturbations corresponding to the sets where there was F_y loading. This happens because F_y and M_x are coupled and any of those two will originate bending in the IT that will mainly affect both bridges $B2$ and $B3$. As it was already mentioned, the F_y force is originated due to misalignments in the tube and the motor/forces application point, which in an ideal case is null. However, the functioning of the motor and the rotor produces always a torque, so the calculation of M_x is correct despite the perturbations in the F_y sets because of the following reasons: first, the F_y calculation is made correctly for the sets that have only a F_y applied and for the sets that have only a M_x applied; second, the M_x is calculated correctly when there is a torque applied; third, the M_x is not calculated correctly in the only case that does not occur in the experiments, that is, when there is F_y but the M_x is null. For these reasons, it is guaranteed that the calculation of F_y and M_x is correct when both are present and when only M_x is.

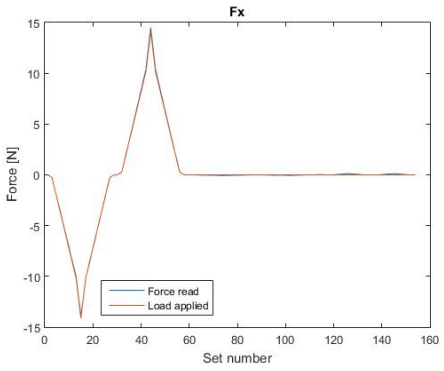

(a) F_x loading.

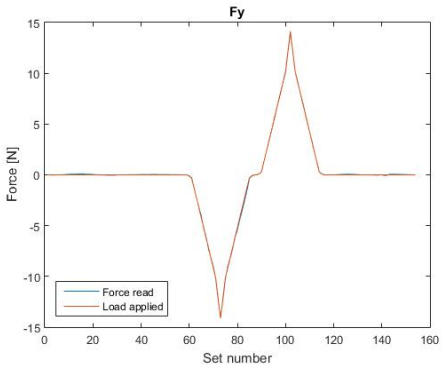

(b) F_y loading.

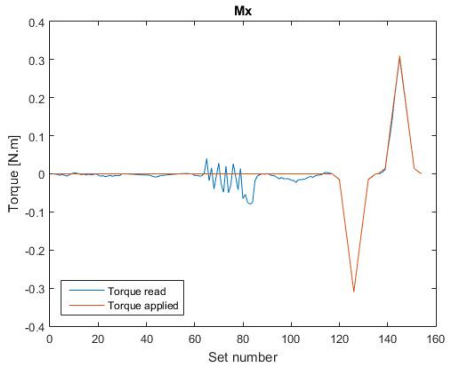

(c) M_x loading.

Figure 3.14: Comparison between the loads applied and the force/torque measured.

Error and Uncertainty Assessment - The coefficients from the calibration matrices have some uncertainties associated, which can be assessed by first calculating the error matrix, present in equation 3.15. Its diagonal elements are the variances of the fitted parameters, and therefore they are the squared uncertainties, whereas the off-diagonal ones are the covariances. So, to obtain the uncertainties of the coefficients, one simply needs to calculate the square root of the diagonal elements.

$$\boldsymbol{V}_{p_i} = \left(\boldsymbol{R}^T \boldsymbol{W}_i \boldsymbol{R}\right)^{-1} \tag{3.15}$$

Following the same logic, to estimate the aerodynamic components uncertainties, the matrix of the estimated aerodynamic components uncertainties is first estimated, through equation 3.16, and then the square root of its diagonal elements are calculated.

$$\boldsymbol{V}_{\hat{y}_i} = \boldsymbol{R}\left(\boldsymbol{R}^T \boldsymbol{W}_i \boldsymbol{R}\right)^{-1} \boldsymbol{R}^T \tag{3.16}$$

3.4 Facility Characterization: The Anechoic Chamber

An anechoic chamber is an echoless room, ideally without any sound reflection from its walls, floor or ceiling. In practice, an anechoic chamber is an enclosure with a sound absorption of 99% or more through the walls, or a reflection 10% or less. These rooms are designed not only to eliminate the echo within, but also to isolate totally from any external sound, which allows to study sound sources within for its intensity and frequency content.

For the experiments, the anechoic chamber situated in the Aerospace Engineering Laboratory of IST is used, which has a usable volume approximately of $4.3 \times 3.2 \times 2.7$ meters ($Length \times Width \times Height$). The chamber has a grid floor installed to permit walking within.

The anechoic chamber is characterized by its insulating properties, and therefore by the sound-absorbing materials used. The chamber is covered in acoustic foam straight wedges, with a tip-to-base dimension of $0.285m$, providing a cut-off frequency of $200Hz$. This means that, for higher frequencies, the chamber has a sound energy absortion above 99% or that the reflected SPL is lower than 10%.

In order to place the workbench and the rest of the equipment used, it was placed a single wooden board covering part of the floor, positioned the farthest away from the microphones as possible. To minimize reflections from the wooden board, the workbench was placed at the edge closer to the microphones. In addition, any equipment that produced noised was covered with foam wedges and placed away from the microphones.

Figure 3.15 presents the background noise measured by each microphone. From the graphs, the cut-off frequency corresponds clearly to the estimated one of $200Hz$, noting that for lower frequencies the existence of sound reflection is perceptible. As for the frequencies above the cut-off one, the background

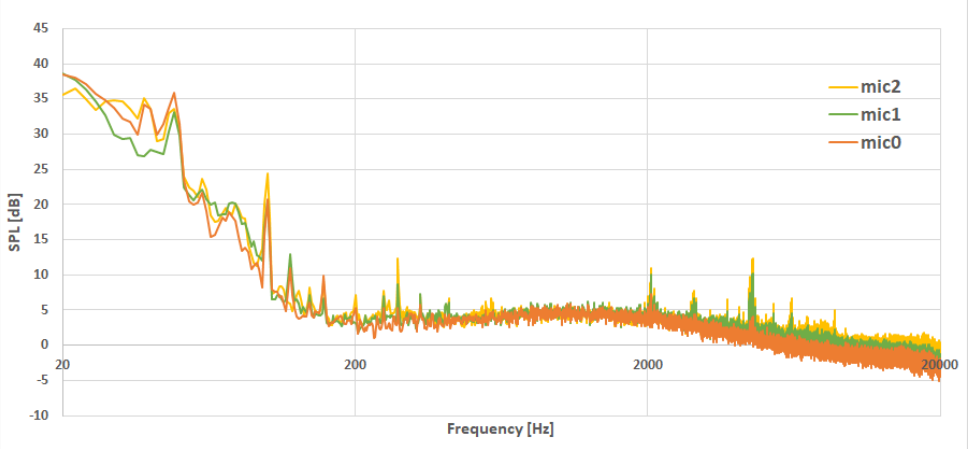

Figure 3.15: The background noise present at the anechoic chamber.

noise is rather low as expected, and desired to perform the experiments, with three peaks that surpass the $10dB$ mark, which are fairly acceptable considering the SPL values obtained by the aerodynamic noise of the rotors.

4

Experimental Results and Discussion

Contents

4.1 Noise Assessment

The noise was collected from the three microphones, which from now on will be referred to as Mic0 (angled $45°$ from the rotor plane to the wake side), Mic1 (aligned with the rotor plane) and Mic2 (angled $45°$ from the rotor plane to the suction side). The seven different rotors tested, listed earlier on Table 2.1, will also be referred to as: baseline; TE60; TE40; TE20; LE60; LE40; LE20 - where, for the cases of the serrated ones, the first two letters correspond to the type of serration and the number indicates the percentage of the blade's span that is serrated.

Initially, the interval of rotation speeds intended to test were of $2000 - 5000$ RPM, with steps of 500 RPM, and the BET and the structural analysis were developed considering that same interval. However, during the first experiments, whenever the rotation speed was increased past the 4000 RPM, the whole workbench would vibrate significantly, especially the IT being used. So, to be on the safe side, the interval of rotation speeds to be tested was modified to be of $1000 - 4000$ RPM, again with steps of 500 RPM.

Along this section, only a few of the graphs containing the data from the experimental tests will be shown. The chosen graphs will help explain the observations assessed about the noise. In Appendix A, the graphs containing the totality of the noise data collected will be displayed.

After having changed the interval of rotation speeds, the conclusion is quickly achieved that the speed of 1000 RPM is too low to assess any considerable noise reduction effects, along the frequency range, by the serrated rotors, which is exemplified in Figures 4.1 and 4.2. However, the comparison of the A-weighted Equivalent Continuous Sound Level (LAeq) and the A-weighted total band power, shown in Figure 4.3, presents some differences between the baseline and the other rotors.

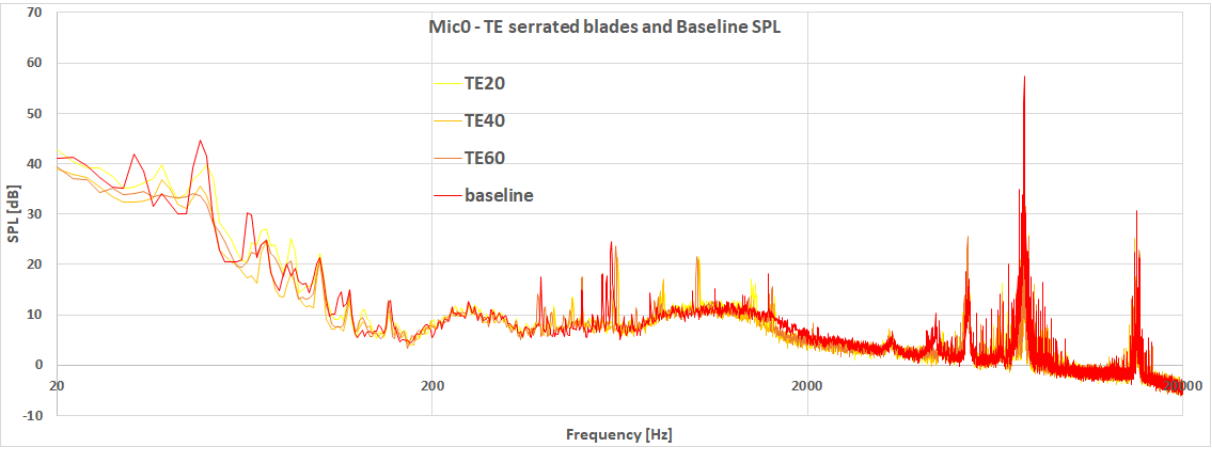

Figure 4.1: SPL of the baseline and the TE rotors at 1000 RPM (captured by Mic0).

In these figures, both the TE as the LE rotors follow approximately the same SPL distribution as the baseline, with the LE rotors presenting only a small noise reduction for the interval of frequencies

$700 - 1900Hz$.

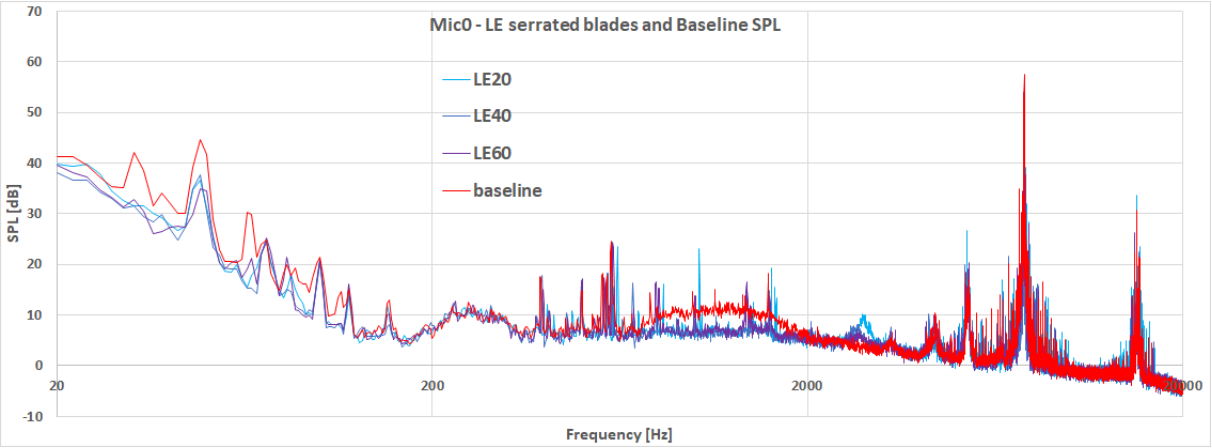

Figure 4.2: SPL of the baseline and the LE rotors at 1000 RPM (captured by Mic0).

There is a recurrent trait noticed when examining Figure 4.3, which is that the LAeq and the A-weighted total band power have values almost equal. In fact, this trait remains for the rest of the rotation speeds tested. Concerning the results for 1000 RPM, there are rotors that decrease considerably the LAeq in comparison to the baseline (mainly the three TE rotors and the LE40 one). On the other hand, the LE20 and the LE60 have values closer to the baseline, with the LE20 even increasing the noise for Mic1 and Mic2. These conclusions taken from the LAeq seem different, at first, from the ones taken from the figures showing the SPL. However, the calculation of the LAeq (and the A-weighted total band power) is mainly influenced by the values of the higher peaks present in the graph (in this case the peak at $7570Hz$), whereas the SPL graphs show its variation with the frequency, thus enabling to assess the noise reduction obtained for different intervals of frequency. In general, this example demonstrates the importance of analysing both the SPL along the frequency and the LAeq.

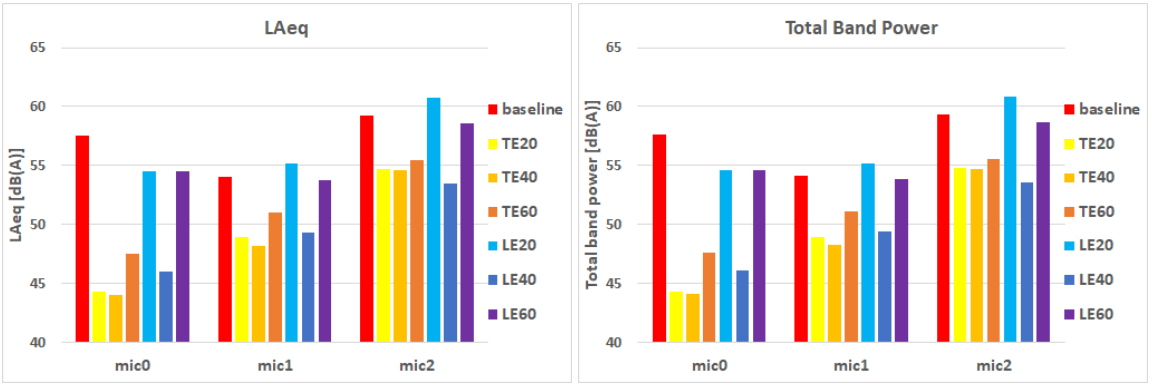

(a) LAeq. **(b)** Total band power.

Figure 4.3: The LAeq and the Total band power measured at 1000 RPM.

Another trait that is noticed is that, for every rotor tested, the SPL varying with the frequency read by Mic1 (in the rotor plane) is smaller than the ones read by Mic 0 and Mic2. Figure 4.4 shows the SPL of the three microphones, measured for the LE40, for three different rotation speeds. This phenomenon starts from $350 - 400Hz$ for the shown velocities, which is also common for the other higher velocities, and it comes to an end at different frequencies, depending on the rotation speed. At 1500 RPM, this difference ends at $5200Hz$; at 2000 RPM, it ends at $14000Hz$; and at 2500 RPM and higher, it occurs until the end of the frequency interval measured. In addition, the difference of the SPL read on the rotor plane, to the other two positions, tends to increase as the rotation speed increases as well.

Overall, the variation of the SPL along the frequency range can be divided into five regions.

First region, at $20 - 200Hz$ - The sound waves are reflected in the chamber's walls, ceiling and floor since the cut-off frequency of the anechoic chamber is $200Hz$. Figures A.1 to A.7 (in appendix) show the SPL of every rotor for every rotation speed, and it can be observed that the SPL decreases as the frequency increases, with the exception of three or four peaks. These peaks appear due to the Blade Passing Frequency (BPF), that is the frequency at which the blades rotate. Noise peaks are known to be produced at this frequency and for the multiples of this value, meaning that consecutive peaks are spaced by $BPF = No.\ of\ blades \times RPM/60\ [Hz]$. Accordingly, as the rotation speed is increased, the values of these peaks are higher (naturally because the noise is louder) and the frequency at which they appear increases as well. This effect is noticed in Figure 4.5 that shows the SPL generated by the TE20 at different rotation speeds. Even so, in these peaks, the noise tends to be reduced by the serrated blades. However, the noise produced in this frequency region is of relatively small importance because the human hearing is not very sensitive to it, which is proven by the A-weighted 1/3 octave band graphs (present in Figures A.8 to A.14) and by the LAeq (present in Figure A.15).

Second region, at $200 - 1900Hz$ - From this region to the following ones the sound is absorbed at the walls, cancelling any sound reflections. Still, similarly to the previous region, there are several peaks in the SPL that, again, are spaced according to the BPF and appear at higher frequencies (and with higher SPL) as the rotation speed increases. This effect is, once more, noticed in Figure 4.5.

In the present region, the LE rotors reduce the noise comparatively to the baseline, and this noise reduction is greater as the rotation speed is increased. On the other hand, the TE rotors present small increases of the noise, but only for Mic0 and Mic2. For Mic1, the tendency is to reduce the baseline noise just a bit. Figure 4.6 shows the A-weighted third-octave bands of the serrated rotors in comparison to the baseline at 3000 RPM, for Mic0.

Third region, at $1900 - 7000Hz$ - In this region the variation of the SPL is continuous and smooth, in opposition to the several peaks that marked the previous region. Plus, most of this region and part

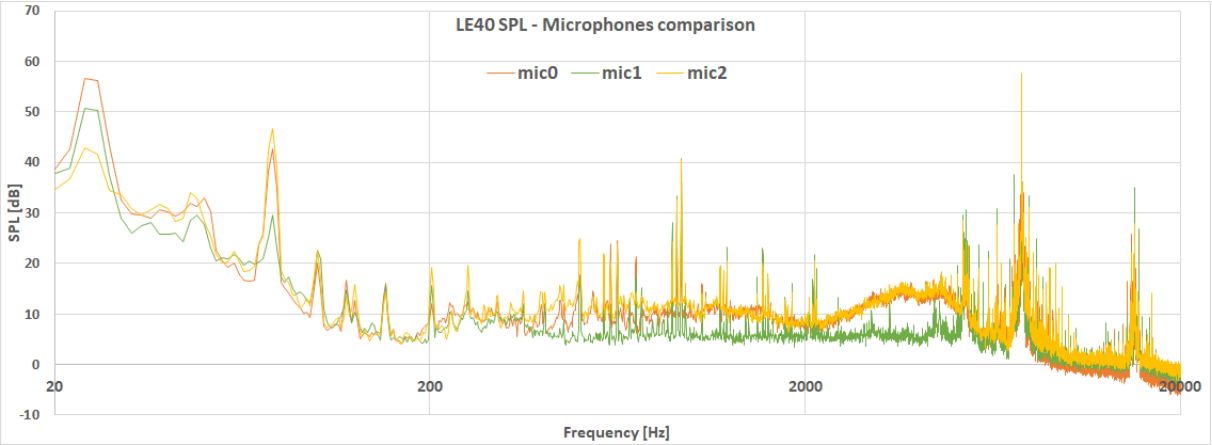

(a) 1500 RPM.

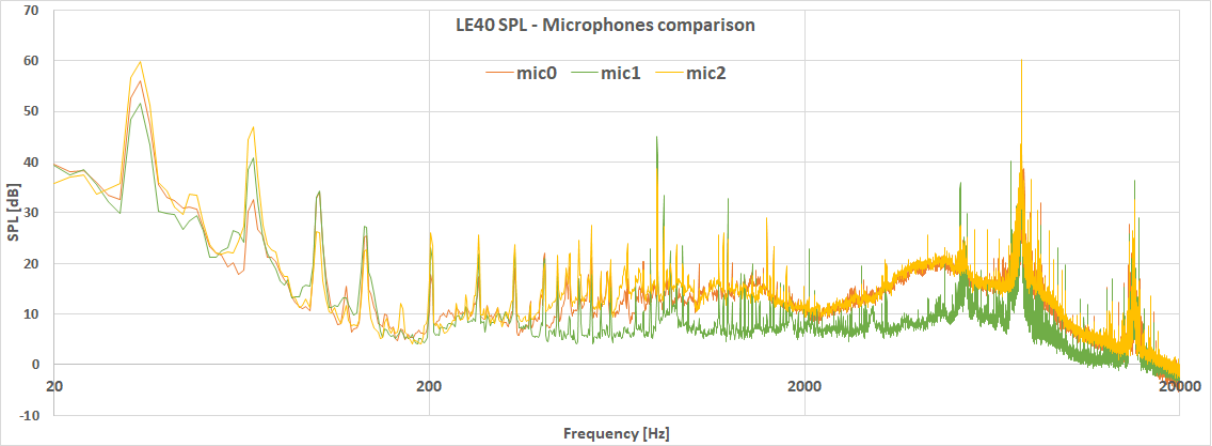

(b) 2000 RPM.

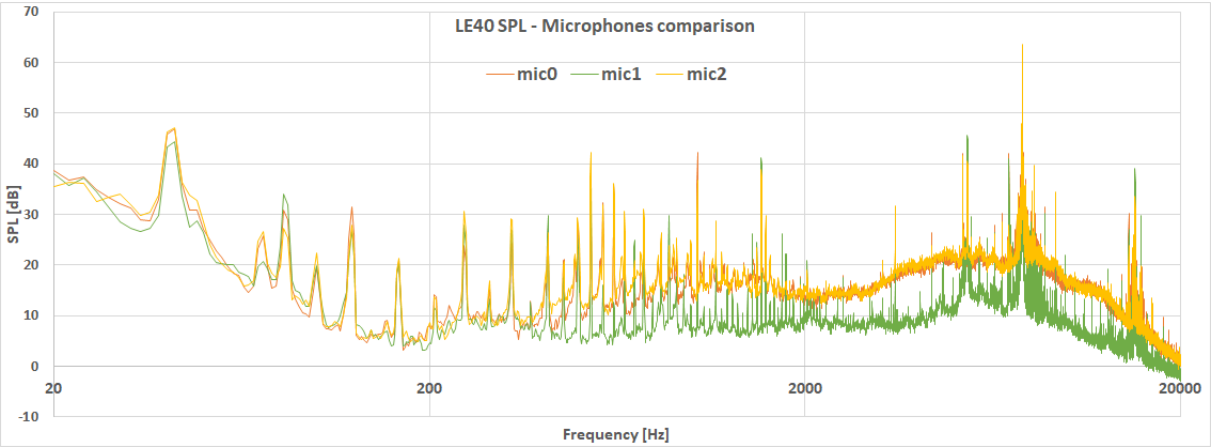

(c) 2500 RPM.

Figure 4.4: The SPL measured from the three microphones for the LE40, at 1500, 2000 and 2500 RPM.

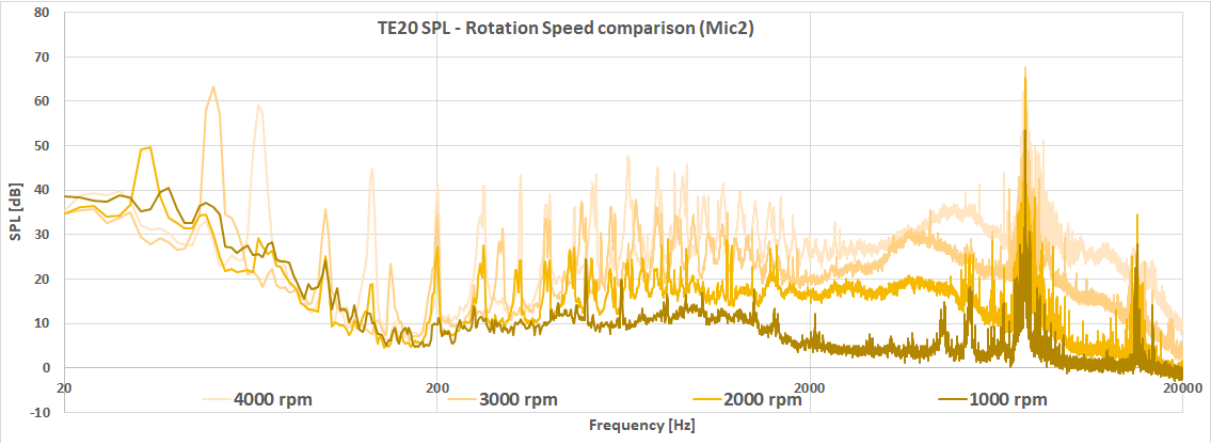

Figure 4.5: SPL of the TE20 at 1000, 2000, 3000 and 4000 RPM (captured by Mic2).

of the previous one correspond to the frequency interval to which the human hearing is most sensitive to, which is from 1000 to $6000Hz$. The A-weighted filter emphasises this interval, which is applied to all third-octave bands graphs all throughout this thesis.

The LE rotors produce less noise, in this region, than the baseline for every rotation speed and microphone position tested. For 2500 RPM and higher, the LE20 and the LE60 are the ones that reduce the noise the most, with the LE20 being the best one for 3500 and 4000 RPM. Figure 4.7 shows the SPL of the LE rotors at 3500 RPM, where the SPL difference between the LE20 and the baseline is always between 5 and $10dB$ throughout this frequency region.

The TE rotors have a distribution of the SPL, relative to the baseline, that varies with the rotation speed. For 1500 RPM, these rotors decrease the noise. However, as the rotation speed is increased (between 2000 and 4000 RPM), the TE rotors produce an ever growing noise increase (in relation to the baseline) in an ever growing frequency interval at the beginning of this frequency region. To simplify this observation, Figure 4.8 is presented, which shows the SPL variation of the TE rotors for 2000, 2500 and 3000 RPM.

For 2000 RPM, the noise is increased between 1900 and $2200Hz$, being reduced for the rest of the region; for 2500 RPM, the noise is again increased between 1900 and $3500Hz$, being reduced for the rest of the region; for 3000 RPM, the noise is increased for the interval $1900 - 4900Hz$, being reduced for the rest of the region; for 3500 RPM, the noise is increased between 1900 and $6100Hz$ and is reduced for the rest of the region; at last, for 4000 RPM, the noise from the TE rotors is bigger than the baseline's in the entire frequency region. In addition, from the indicated figure and also from the SPL graphs in appendix, the noise increase, relative to the baseline, is always bigger as the rotation speed increases.

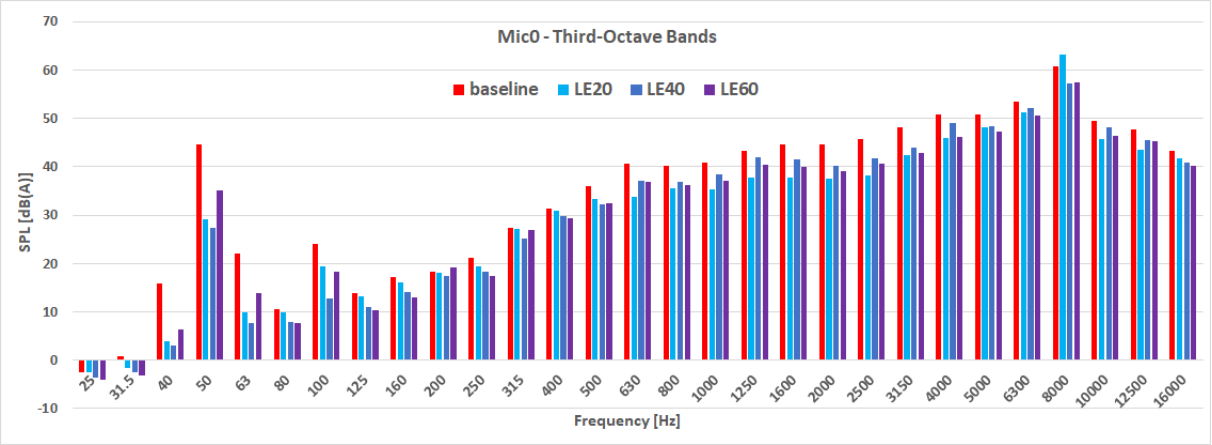

(a) LE rotors.

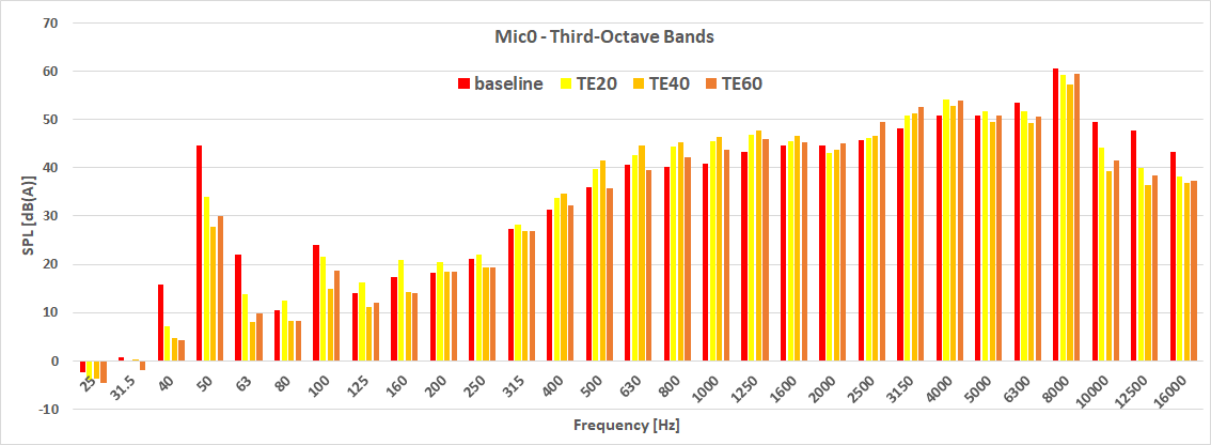

(b) TE rotors.

Figure 4.6: The third-octave bands distribution at 3000 RPM (captured by Mic0).

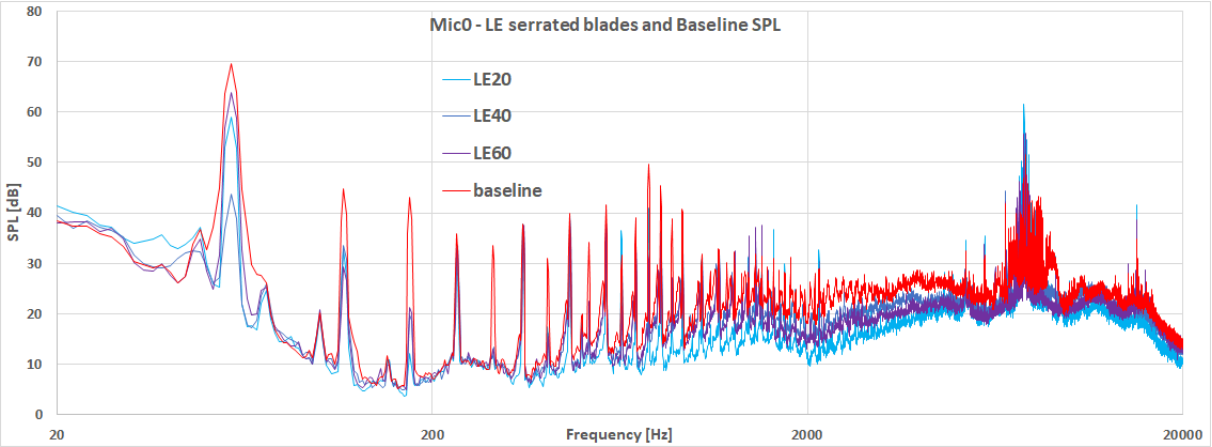

Figure 4.7: SPL of the LE rotors at 3500 RPM (captured by Mic0).

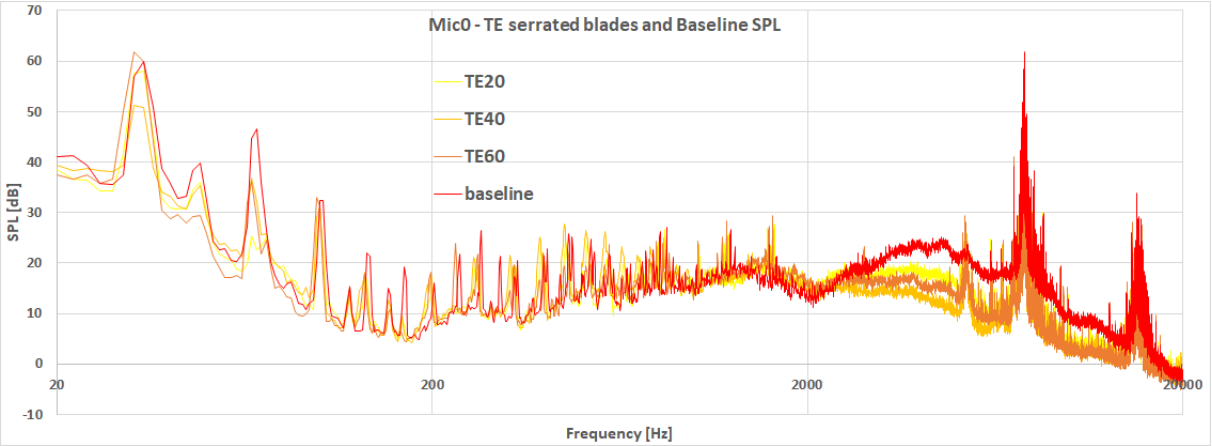

(a) 2000 RPM.

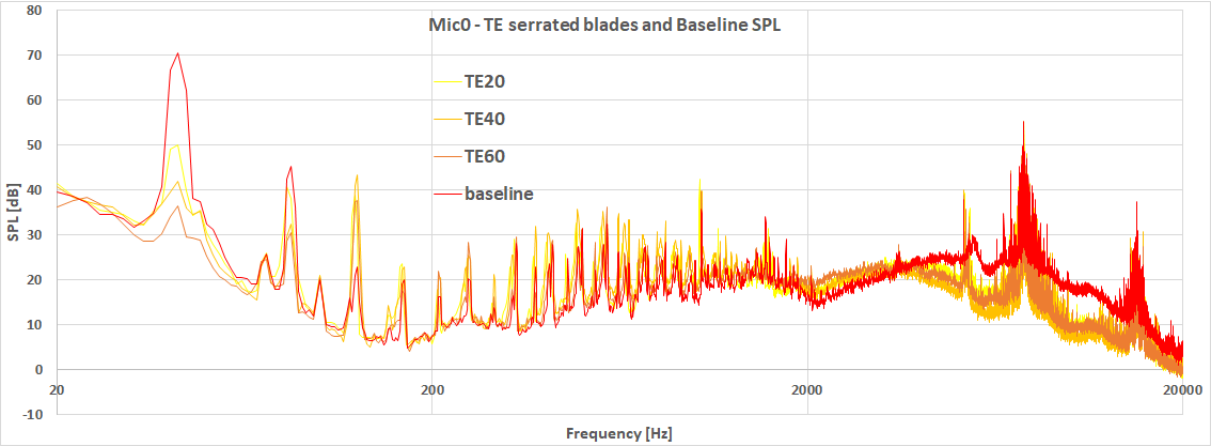

(b) 2500 RPM.

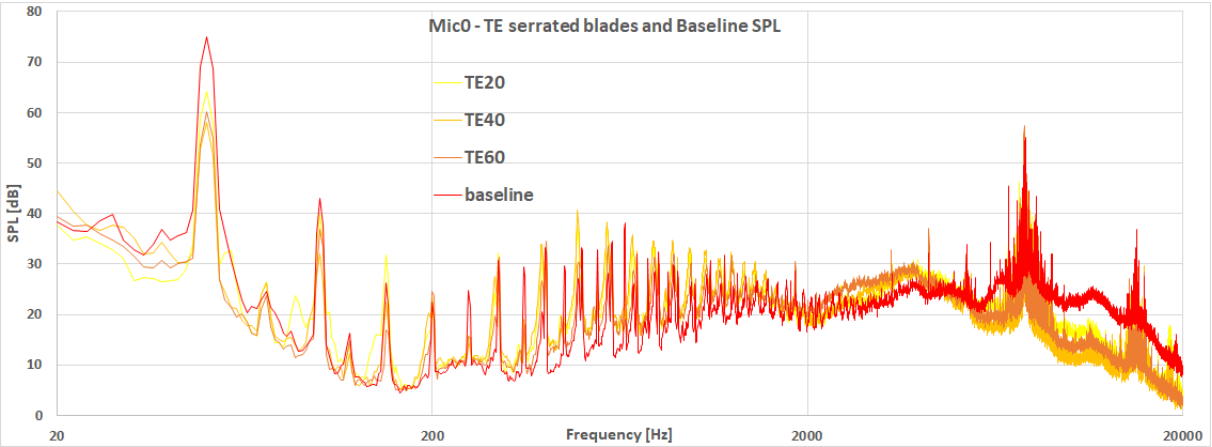

(c) 3000 RPM.

Figure 4.8: SPL of the TE rotors at 2000, 2500 and 3000 RPM (captured by Mic0).

Fourth region, at $7000 - 8400Hz$ **-** This is the region which contains the highest noise peak in the SPL distribution, when the A-weighted filter is applied to consider the human hearing sensitivity. Consequently, the value at this peak will be the most important for the calculation of the LAeq for each test. It always appears between 7560 and $7570Hz$ for every rotor and rotation speed, but it is not produced by the blades themselves. This noise peak is mainly generated by the motor when it is being powered to rotate. Figure 4.9 presents the noise produced by the motor, at 3500 RPM, without any rotor attached.

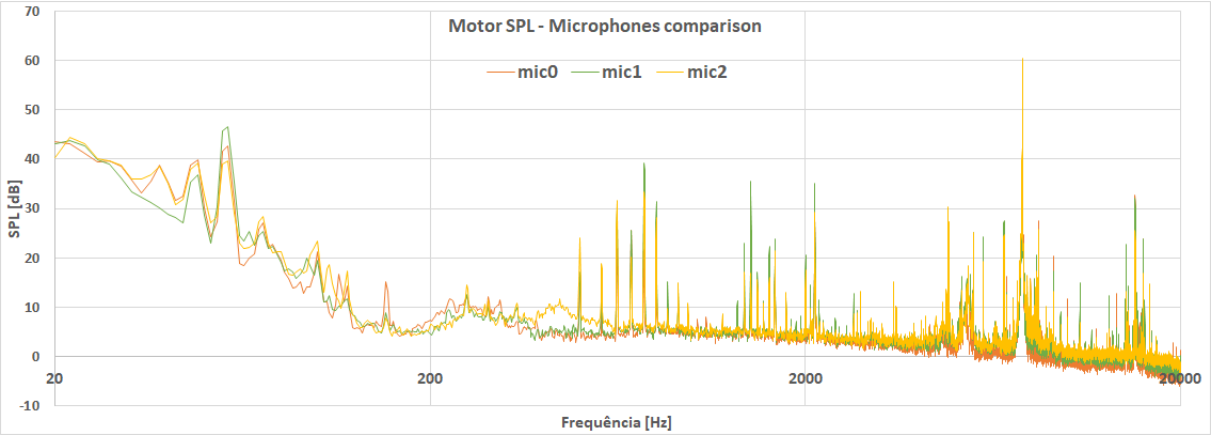

Figure 4.9: The SPL measured from the three microphones for the motor, at 3500 RPM.

For most of the frequency spectrum, the motor noise is similar to the background noise, with the exception of some SPL peaks, including the peak addressed for this frequency region. To understand better the influence of the motor noise on the noise collected from each rotor, Figure 4.10 is presented, which compares the noise produced by the LE20 with the motor noise, at 3500 RPM.

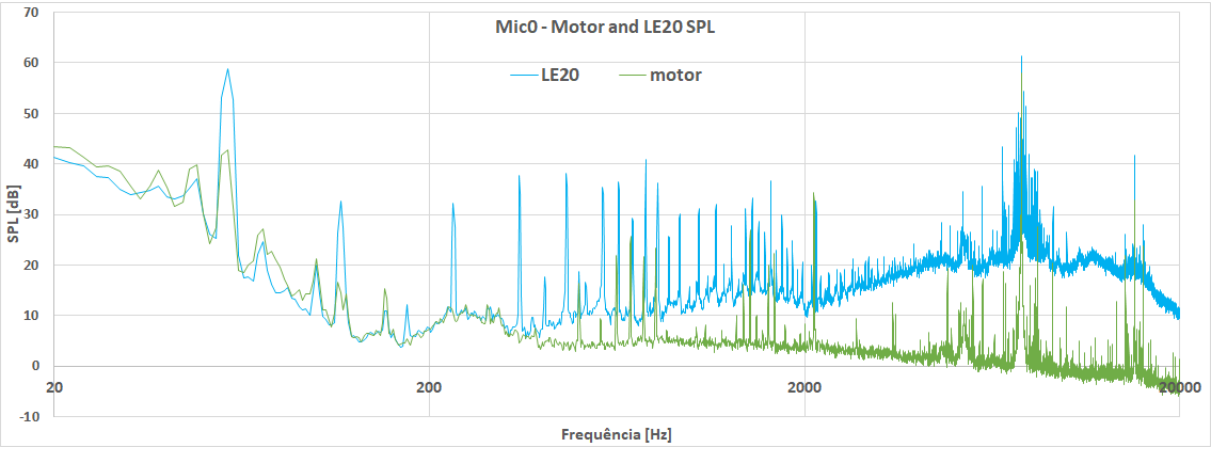

Figure 4.10: SPL of the motor and of the LE20 rotor, at 3500 RPM (captured by Mic0).

The motor noise has some peaks in the second frequency region $(200 - 1900Hz)$, but these peaks only add to the peaks measured from the noise of the rotor, not causing them since the SPL graph for

the LE20 has many more peaks (related to the BPF, as was previously explained) with greater value. In the third frequency region ($1900 - 7000Hz$), the motor noise seems not to influence the noise from the LE20. However, in the present frequency region, the fourth ($7000 - 8400Hz$), the big noise peak created by the motor is the major contributor to the noise peak displayed in the LE20 SPL graph and also to the same peaks in every SPL distribution of every rotor noise presented throughout this thesis. Even so, the different rotors have different values of the SPL at this peak, which means that, although the motor is the main influence to it, the serrated rotors may still obtain noise reduction relative to the baseline noise.

The TE rotors reduce the noise for this region for every speed except for 3500 and 4000 RPM. This observation is confirmed by analysing the third octave bands graphs displayed in Figures A.8 to A.14.

Without counting with the peak, the LE rotors reduce the noise in the whole frequency region, as is seen in Figure 4.11. But the noise in this region is controlled by the peak value, so the analysis is made towards it. The LE20 presents a noise increase for the peak for every rotation speed, which is unfortunate since this rotor is the one that achieves the greatest noise reduction, relatively to the baseline, for the majority of the frequency spectrum analysed (particularly for the frequencies which the human hearing is more sensitive to). Furthermore, since the LAeq is influenced mainly by the value of this peak, the LAeq of the LE20 is higher than the baseline's for most of the rotation speeds tested (from 2000 to 4000 RPM). In contrast, the LE40 is the rotor which normally presents the lowest peak value for every speed tested, except for 4000 RPM where it equals the baseline peak's value. Consequently, the LE40 is the rotor that will most likely present the lowest LAeq values. The LE60 increases the peak noise for the higher rotation speeds, but not as much as the LE20. For the rest of the speeds, the LE60 has a similar peak value as the baseline. Again, these observations can be confirmed by assessing the third octave bands graphs mentioned.

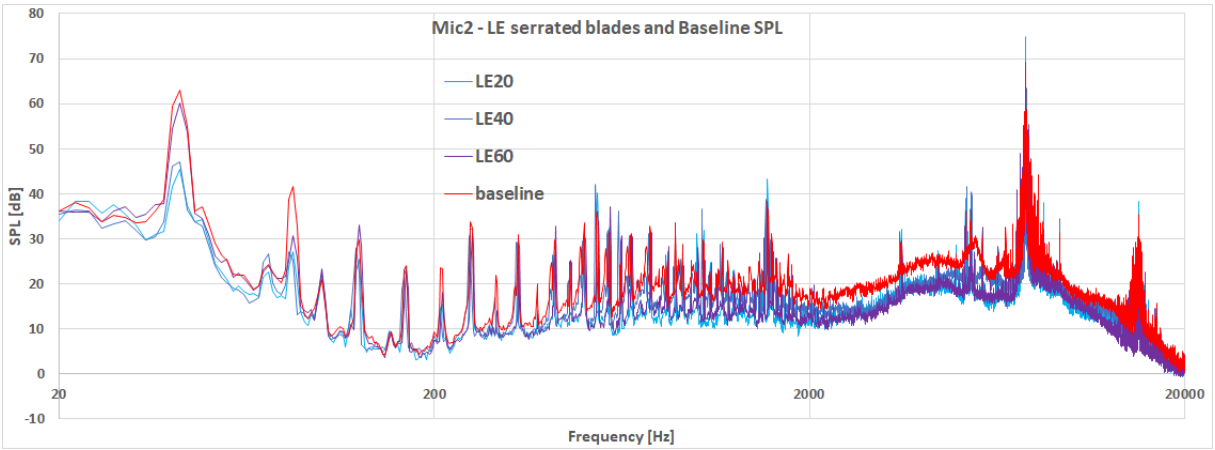

Figure 4.11: SPL of the LE rotors at 2500 RPM (captured by Mic2).

Fifth region, at $8400 - 20000Hz$ - The noise varies, mostly, continuously and decreasing with the increasing of frequency. There is a noise peak at $15140Hz$, that is exactly the double of the frequency at which appears the big noise peak in the previous region.

In this region, at 2000 RPM and higher, the TE rotors reduce the noise significantly (up to $13dB$) with this reduction being greater as the rotation speed is increased. Figure 4.12 shows the SPL variation for the TE rotors, where it can be noticed the TE noise reduction for the region in question. It is worth noticing that the blades with the TE serration applied for longer lengths of the span achieve bigger noise reductions. In this case, it means that the TE60 reduces the noise more than the TE40, which in turn reduces the noise more than the TE20.

These results were expected since the TE serrations target the TE noise, which is predominant in the higher frequencies of the total aerodynamic noise (which was previously approached in Chapter 1).

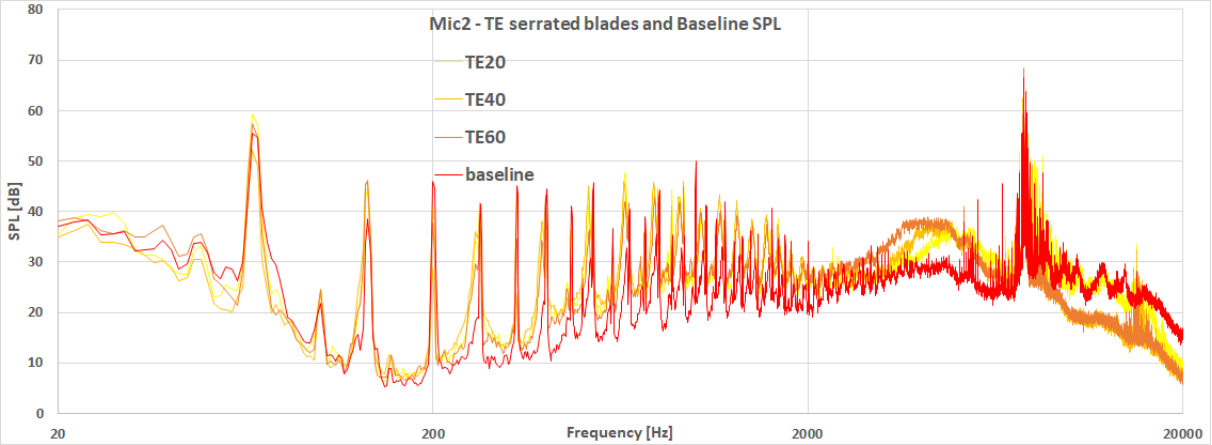

Figure 4.12: SPL of the baseline and the TE rotors at 4000 RPM (captured by Mic2).

The LE rotors reduce the noise in this region as well, although clearly not as much as the TE ones, which can be seen in Figure 4.13, that shows the SPL variation of the LE rotors. This result was also expected because the LE serrations prevent the TE turbulent boundary layer from growing as much as it would if there were no serrations, which leads to weaker noise sources along the TE.

Remembering Soderman's study [30], where it was used a rotor with $1.52m$ of diameter with serrated strips attached to the LE and rotating at a maximum speed of 1440 RPM, it was obtained a maximum noise reduction of $17dB$ in the highest octave band ($16000Hz$). Between 8000 and $16000Hz$, the rotor also achieved noise reductions between 12 and $17dB$, which is considerably bigger than the noise reduction obtained for any of the LE serrated rotors tested. However, between 1000 and $4000Hz$, Soderman's serrated strips reduced the noise between 3 to $6dB$, whereas the present LE serrated blades reached $10dB$ of noise reductions. In addition, Soderman stated to have reached noise reductions of the OASPL between 4 to $8dB$, while in the present study the maximum reduction obtained in the LAeq (and in the total band power) is of $13dB$ with the TE40 at 1500 RPM. Anyway, any comparison of results

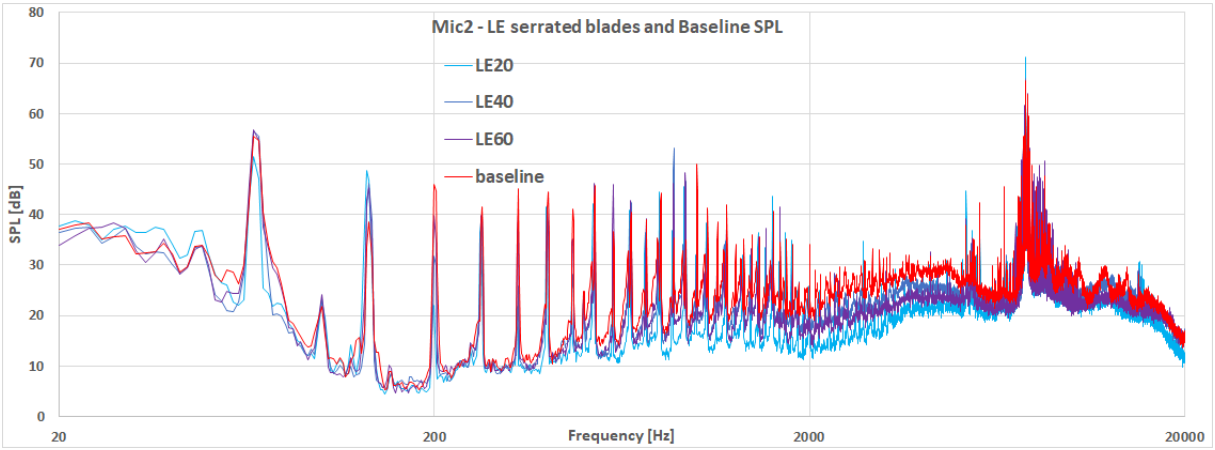

Figure 4.13: SPL of the baseline and the LE rotors at 4000 RPM (captured by Mic2).

with the ones obtained by Soderman is qualitatively incorrect because the dimensions of the rotors and the rotation speeds tested are considerably different. Even so, the comparisons made were considered interesting enough to be pointed out.

Having finished the analysis of the SPL per regions, the LAeq can also be regarded. Figure A.15 presents the LAeq measured for every rotor and rotation speed. The TE rotors have a reduced LAeq, in comparison to the baseline, for the rotation speeds between 1500 and 3000 RPM. However, for the highest tested speeds, the TE rotors have a bigger LAeq than the baseline. In the case of the LE20, it has, mostly, a bigger LAeq than the baseline due to the SPL peak at $7570Hz$ mentioned before. The LE40 has, in general, a lower LAeq than any other rotor. The LE60 has a lower LAeq than the baseline in most cases, but it is not as reduced as the one produced by the LE40.

4.2 Aerodynamic Assessment

The tests conducted to assess the aerodynamic performance followed the same conditions as the tests addressing the noise. And, just like the noise tests, separate measurements were taken of the seven rotors at the seven different rotation speeds, from 1000 to 4000 RPM. The measurements taken were of the thrust T, which is equal to $-F_x$ in the coordinate system of the IT, and of the torque Q that, in turn, is equal to the moment M_x. Knowing that the power is calculated through equation 4.1, the results of the thrust and the power are obtained for every test.

$$P = Q \times \Omega \tag{4.1}$$

The first blades tested were the baseline ones, whose experimental results were compared to the results estimated by the BET. Figure 4.14 shows the thrust and the power of the baseline obtained

experimentally and theoretically. Following Figure 4.14(a), the measured thrust is considerably close to the estimated one, noting that the latter is always slightly higher than the experimental one, with the difference between both increasing as the rotation speed increases. This graph proves that the BET is a fairly good method to estimate the thrust of the rotor, with very close results between 1000 and 2500 RPM, despite being quite simplistic. Consequently, the bending moment in the root of the blade, calculated in Chapter 2, over-estimates just a bit the real value, which was intended due to safety reasons. And for that reason, the estimated value is quite adequate.

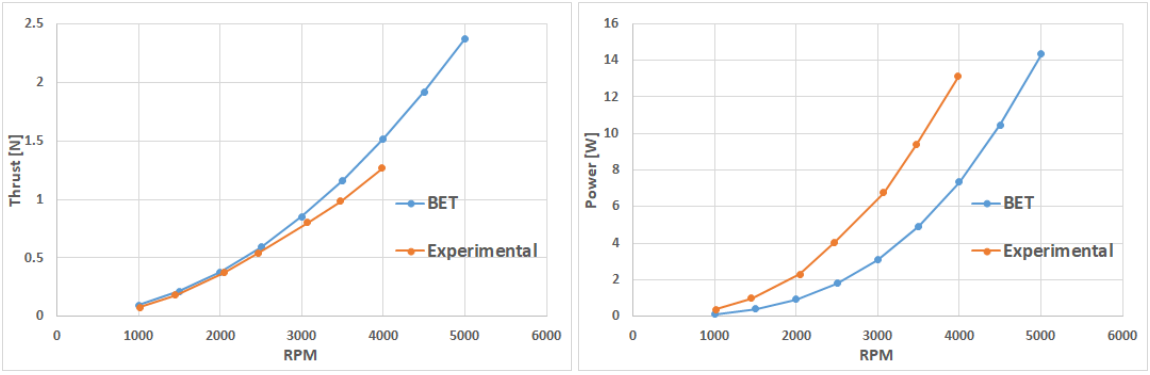

(a) Thrust. **(b)** Power.

Figure 4.14: The baseline rotor thrust and power, estimated by the BET and measured experimentally.

The experimental aerodynamic power, shown in Figure 4.14(b), is higher than the one computed through the BET. However, this result had already been expected when the theoretical model was applied, because the rotor used is relatively small and operates at very high rotation speeds in opposition to helicopter blades, which are considerably bigger and operate at lower speeds (to whom the BET is normally applied). Smaller blades at higher rotation speeds have an increased interaction with vortexes, which increases the drag and the tridimensional effects of the flow (that are neglected by the BET).

The FM calculated with the BET is constant and equal to 0.515, whereas the FM obtained experimentally is much lower, due to the high values of the power. Experimentally, the FM has the lowest values for 1000 and 1500 RPM (0.11 and 0.16, respectively), with the tendency to increase by increasing the rotation speed and reaching values between 0.20 and 0.22 for rotation speeds between 2000 and 4000 RPM. This just demonstrates that, for the baseline, the rotation speeds 1000 and 1500 RPM are too low to obtain any desirable aerodynamic performance. Furthermore, in the figures that will be presented along this section, it is noticeable that every rotor has a very poor performance for these two rotation speeds, meaning that any typical rotor of similar dimensions to the ones presented in this thesis will unlikely operate at these lowest rotation speeds. Therefore, the aerodynamic assessment presented in this section will, to some extent, overlook the results obtained for these rotation speeds.

Figure 4.15 presents the thrust measured for the different rotors. Analysing first the TE ones, these rotors are the ones that generate the lowest propulsive force for every rotation speed tested. This observation was expected since the TE serrations applied to these rotors not only reduce the blade surface area, but they also modify and deteriorate the smoothness of the TE, creating edges and forcing a more abrupt reunion between the flows of the upper surface and the lower surface of the blade.

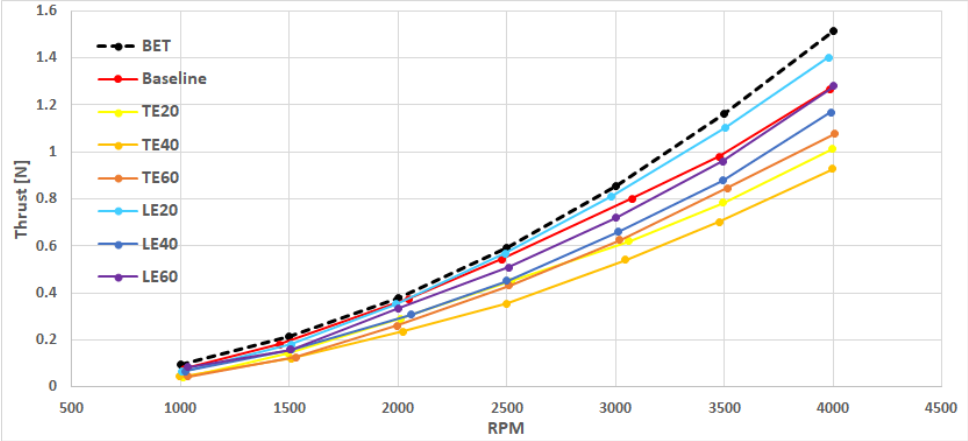

Figure 4.15: The thrust measured for all rotors and estimated by the BET.

Figure 4.16 shows the percentage of C_T of each serrated rotor in relation to the C_T of the baseline. The worst rotor in terms of thrust generated is the TE40, for rotation speeds 1500 RPM and higher. The TE20 has a percentage of thrust between 50% and 75% for the lowest rotation speeds, but then this value remains steady around 80% for speeds between 2000 and 4000 RPM. The TE60 shows a percentage of C_T constantly increasing with the rotation speed and reaching a value higher than the TE20 for speeds equal and higher than 3000 RPM, which is quite surprising since the blades of this rotor are the ones that have the TE serration applied for the longer span of the blade. Noting also that comparing the TE40 with the TE60 (with a difference of 20% of the span of the blades serrated), the latter has always a percentage of C_T higher by around 10% for rotation speeds of 2000 RPM and higher. Lee *et al.* [20] presented a percentage of thrust loss around 15% for TE serrated blades over 25% of the span, tested for rotation speeds between 1500 and 3000 RPM. For blades serrated over 50% of the span, the thrust loss decreased between 27% and 22% as the rotation speed increased, similar to the results here presented.

The LE rotors experienced smooth modifications to the surface in the LE. Consequently, their thrust is closer to the one generated by the baseline in comparison to the TE rotors. In general, and evaluating only between 2000 and 4000 RPM, the percentage of thrust relative to the baseline increases as the rotation speed increases. The LE40 is the rotor which generates the lowest thrust, of the three LE rotors, with a percentage of C_T between 81% and 91%. The LE60 generates between 91% and 100% of the baseline's thrust, whereas the LE20 surpasses the baseline with values between 100% and 111%

and becoming the rotor which generates the highest thrust. Chong *et al.* [34] studied wings with sinusoidal LE and concluded that higher values of the serration amplitude led to higher losses to the C_L and C_{L_α} coefficients. However, for small serration amplitudes and large serration wavelengths, the C_L showed almost neglectable losses, but the stall angle would become considerably higher, which could be considered as an improvement to the overall aerodynamic qualities of the wing. Considering another study, Roger *et al.* [37] studied a NACA-0012 wing with sinusoidal LE serrations, stating that this type of serrations delayed (or even prevented) the separation of the flow, but in turn, it also contributed to the formation of a thicker boundary layer on the suction side of the wing, leading to an increase in drag.

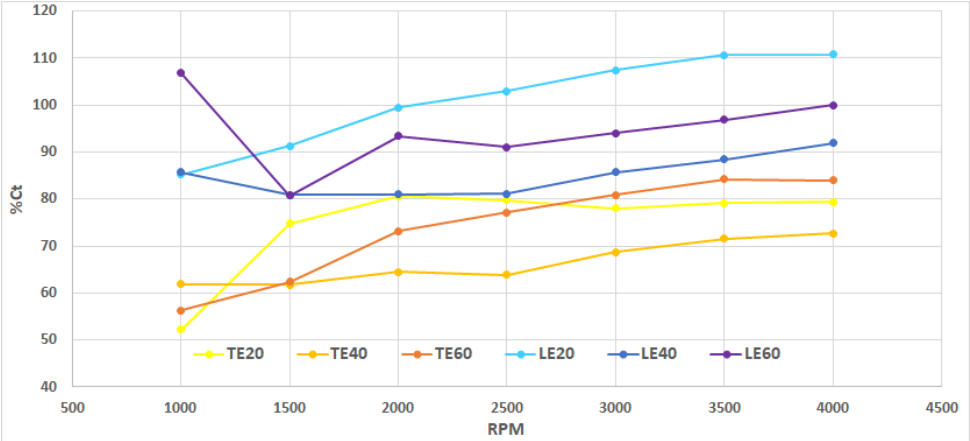

Figure 4.16: Percentage of C_T in relation to the baseline.

Figure 4.17 presents the power measured for the rotors. As this graph may seem a bit confusing, the percentage of the C_P in relation to the baseline was calculated and is displayed in Figure 4.18.

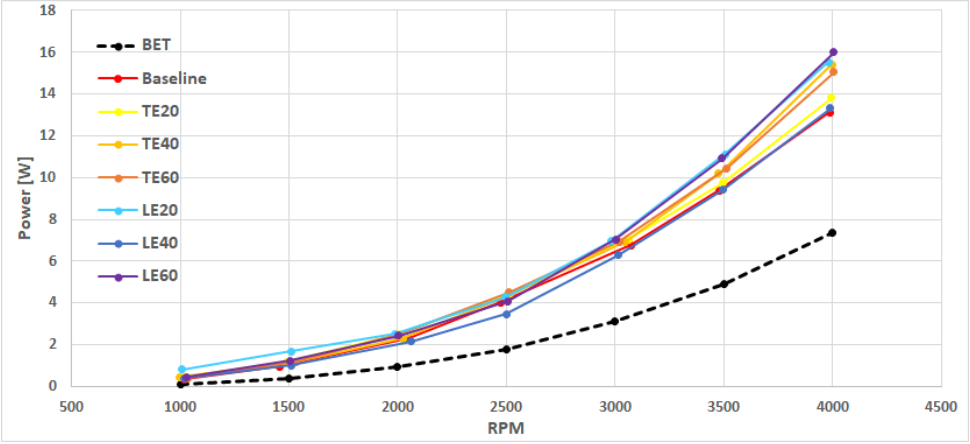

Figure 4.17: The power measured for all rotors and estimated by the BET.

From the graphs, every rotor has a higher power than the baseline, except the LE40. This rotor has lower power for rotation speeds between 1000 and 3000 RPM, reaching a minimum value of percentage

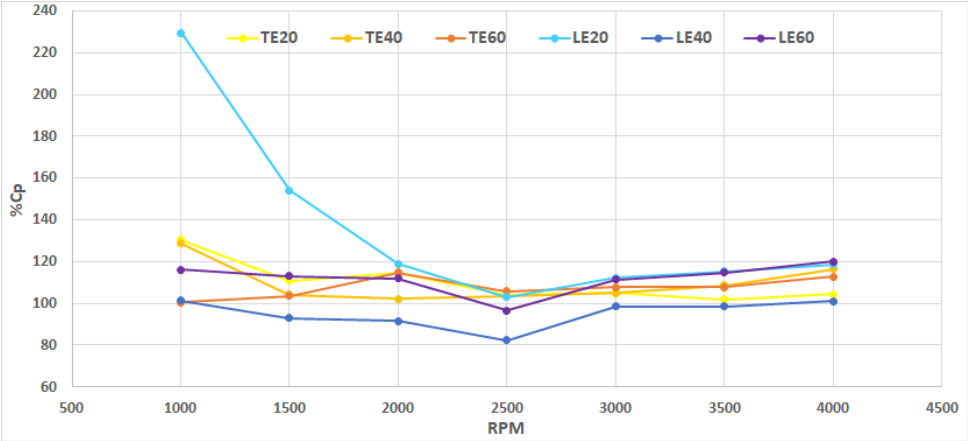

Figure 4.18: Percentage of C_P in relation to the baseline.

of C_P of 82% at 2500 RPM, and a value close to 100% for at 3000, 3500 and 4000 RPM. The other five serrated rotors have a percentage of C_P between 100% and 120% for the most relevant rotation speeds ($2000 - 4000$ RPM). The three LE rotors present all a minimum for 2500 RPM, while the three TE rotors present a very small variation of the percentage of C_P with the rotation speed. Curiously, although the LE40 is the rotor with the lowest percentage of C_P for rotation speeds between 3000 and 4000 RPM, the LE20 and LE60 have the higher values. For the mentioned speeds, the TE20 presents almost the same C_P as the baseline.

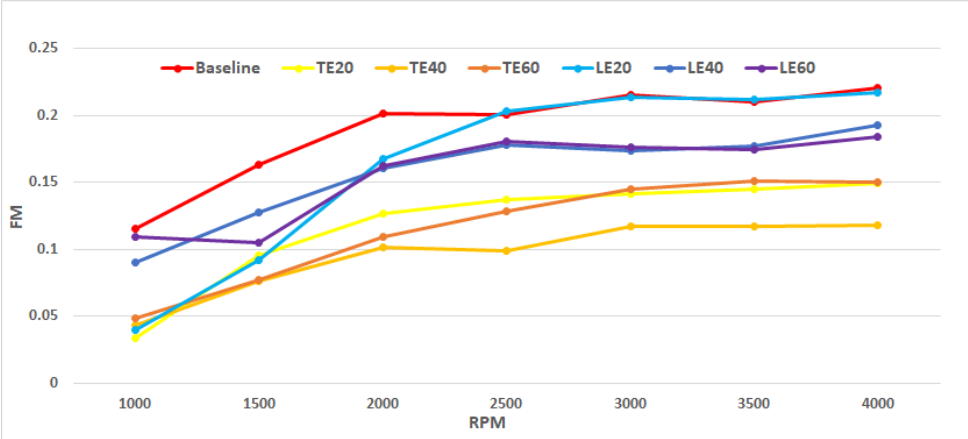

Figure 4.19: The FM obtained for all the rotors.

Figure 4.19 shows the FM obtained from the experiments, and there are four remarks to mention. First, the FM tends to increase as the rotation speed increases. Second, the TE rotors consistently present the lowest values, with TE40 being the worst with a maximum FM of 0.117 and both TE20 an TE60 with maximums of 0.15. Third, taking only into account the speeds equal and higher than 2000 RPM, the LE40 and the LE60 have an almost identical variation, which are clearly more efficient than

the TE rotors but still worse than the baseline. Fourth, the LE20 has relatively low values of FM at lower rotation speeds. However, it reaches similar values as the baseline between 2500 and 4000 RPM. The same LE20 rotor generated a higher thrust than the baseline, but also a higher power. Therefore, concerning the aerodynamic performance, the LE20 is, in the bare minimum, as interesting as the baseline.

The different serrated blades have a different surface area from the baseline, due to the serrations applied. So, in order to evaluate the thrust generated weighted by the different surface areas, the term C_T/σ was calculated, where $\sigma = 2 \times A_p/A$ is the rotor solidity, and A_p is the blade planform area. Figure 4.20 shows the variation of the FM and the C_T/σ for the tested rotors and rotation speeds. Once again, the LE20 shows an aerodynamic performance quite interesting for the higher rotation speeds. On the other hand, the TE serrations degrade considerably the aerodynamic performance of the blades.

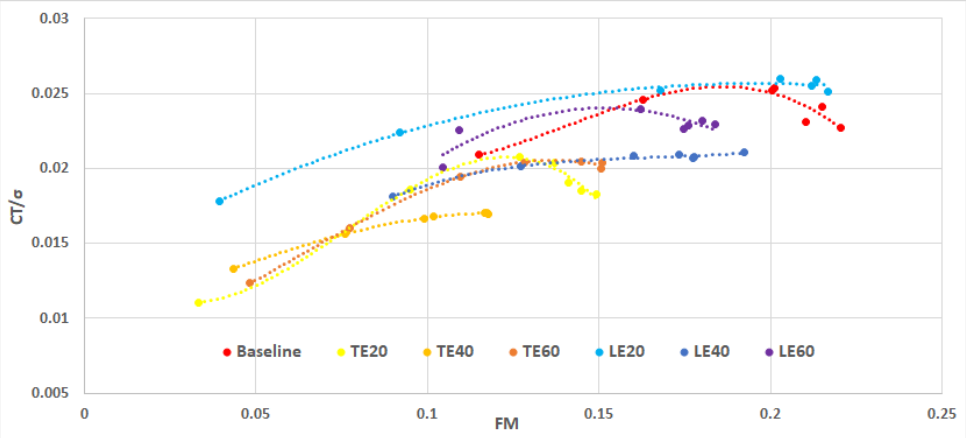

Figure 4.20: Comparison of the C_T/σ versus the FM.

Considering the satisfactory characteristics of the LE20, the LE40 has a far worse performance in terms of both C_T/σ and FM. However, with 60% of the LE serrated (LE60), there is an improvement of the aerodynamic characteristics, which leads to the conclusion that there are, at least, two optimum configurations concerning this kind of LE modifications: one close to the 20% of the serrated LE, and the other close to the 60%. This conclusion does not solely apply to sinusoidal LE, for there might be other types of curved and smooth geometries that, while implemented to the LE, might provide results as interesting as these ones.

5

Conclusions and Recommendations

Contents

Three TE serrated rotors and three LE serrated rotors were designed, produced by additive manufacturing, and tested against a typical baseline rotor. The noise generation and the aerodynamic performance were assessed, leading now to the final remarks of this thesis. These final remarks are only applied for the tested rotors and for the operating conditions that they were submitted to.

5.1 Conclusions

The noise generated by an operating rotor is not directionally uniform, for it is clear that the noise in the rotor plane is lower than at 45° to either the suction side or to the wake side. Even so, for any of the directions, the serrated rotors can achieve noise reductions, in comparison to the baseline, for at least some intervals of the frequency spectrum. However, the noise reductions are highly dependant on the rotation speed, and the same rotor can reduce the noise for some speeds and increase for others.

The TE serrated blades are effective in reducing the high frequency noise for any rotation speed, but the LAeq measured increases significantly for the higher tested speeds. So, acoustically, these blades are only worth using for the lower-to-moderate speeds. However, considering the aerodynamic performance, the TE serrated rotors are never worth being used for any rotation speed because they clearly degrade the aerodynamic qualities. Comparing to the baseline, these rotors generate considerably less thrust and require more power, which leads to a very low efficiency. Overall, and comparing with the LE serrated rotors, the TE serrations do not seem a viable feature to implement in real rotors of small UAVs.

The LE serrated blades proved to reduce the noise in the mid-range frequencies, which correspond to the noise frequencies that the human hearing is most sensitive to. In addition, these blades also achieved small noise reductions for the high frequency noise. However, they presented, as well, increases in the measured LAeq for some rotation speeds, specially the LE20 rotor. This rotor was the one to obtain the best reductions in the SPL, in comparison to the baseline, but it also obtained, consistently, the bigger LAeq values due to increasing the noise in the frequency at which the motor noise was higher. In opposition, the LE40 rotor reduced the LAeq for every rotation speed, even though it did not reduce the mid-frequencies SPL as much as the LE20. Furthermore, regarding the aerodynamic performance, the LE serrated rotors presented quite interesting results, with the LE20 over-performing the baseline for the mid-to-high rotation speeds in terms of thrust and of Figure of Merit. The other two LE serrated rotors did not perform so well, but still they had higher thrust and efficiency than the TE serrated rotors. All in all, the LE serrations are an interesting option to implement on rotating blades, for both acoustical and aerodynamic reasons, and, in the present thesis, one could say that the best compromise is found either in the LE20 or in the LE60 rotors.

This thesis focused, partly, on sinusoidal LE modifications, but hopefully it suggests that the use of other types of curved and smooth LE modifications on blades are worth studying because they could be

beneficial for both aerodynamic and acoustic purposes, as it was found to be during this study.

5.2 Future Work

As it was stated in the conclusions, the TE serrated blades do not seem a viable option to implement on real UAV rotors due to the significant degradation of the aerodynamic performance. On the other hand, LE modifications implemented on blades could improve the overall aerodynamic and aeroacoustic performances. So, for future work, it would be interesting to continue and to deepen the study of aerodynamic noise produced by rotors with a modified LE, either with a smooth sinusoidal LE or with other type of smooth and curved modification. Furthermore, to better understand the influence of these modifications, the use of computational tools, as Computational Fluid Dynamics and Computational Aeroacoustics, is recommended to assess the aerodynamic performance and the noise generated.

In the beginning of this thesis it was mentioned that the first rotors designed were smaller than the ones that were used in the experiments. Also, the profile chosen from the beginning for all designs was the NACA-0018 due to its relatively high thickness, which was kept after increasing the dimensions of the designs. While for the blades with smaller dimensions the NACA-0018 seemed to suit well (apart from the bad quality of the printed parts), for the blades after increasing the dimensions the NACA-0018 seemed to have an excessive thickness. However, it was only after printing and testing the rotors that it was noticed that the rotors might had had more mass than intended, due to the high thickness of the profile, which made it difficult to test the rotors for higher rotation speeds. So, for future studies, it would be interesting to use profiles with smaller thicknesses in order to study higher rotation speeds. Moreover, it would also be interesting to study rotors with LE modifications using cambered profiles because those profiles are the ones typically used for both UAVs and helicopters.

In the present thesis, the angle of attack is always constant for all tests and the twist is the same between all rotors. So, another feature that is interesting to explore is the behavior of the blades' serrations, in terms of noise generation, to different variations of twist and to different angles of attack.

The workbench used to test the rotors imposed a constraint to the maximum blade radius, due to the height of the IT. Plus, the printer that was used also imposed a constraint to the dimensions of each part printed. However, by using a bigger printer (for example, the Ultimaker 5s which is available at the Laboratório para Desenvolvimento do Produto in IST) and dividing the rotor at the hub so that each blade is a separate part, bigger rotors could be printed. If the workbench was modified, or even built anew, bigger rotors could be tested. This way, the use of serrations to both leading and trailing edges could be studied on bigger rotors.

Bibliography

[1] M. Barone, "Survey of techniques for reduction of wind turbine blade trailing edge noise," *SandiaTechnical Report*, pp. 1–26, August 2011.

[2] S. Oerlemans and J. G. Schepers, "Prediction of wind turbine noise and validation against experiment," *International Journal of Aeroacoustics*, vol. 8, no. 6, pp. 555–584, 2009.

[3] R. K. Amiet, "Acoustic radiation from an airfoil in a turbulent stream," *Journal of Sound and Vibration*, vol. 41, no. 4, pp. 407–420, 1975.

[4] ——, "Noise due to turbulent flow past a trailing edge," *Journal of Sound and Vibration*, vol. 47, no. 3, pp. 387–393, 1976.

[5] M. S. Howe, "Aerodynamic noise of a serrated trailing edge," *Journal of Fluids and Structures*, vol. 5, no. 1, pp. 33–45, 1991.

[6] ——, "Noise produced by a sawtooth trailing edge," *Journal of the Acoustical Society of America*, vol. 90, no. 1, pp. 482–487, 1991.

[7] S. Sinayoko, M. Azarpeyvand, and B. Lyu, "Trailing edge noise prediction for rotating serrated blades," *20th AIAA/CEAS Aeroacoustics Conference*, pp. 1–20, June 2014.

[8] B. Lyu, M. Azarpeyvand, and S. Sinayoko, "Noise prediction for serrated leading-edges," *22nd AIAA/CEAS Aeroacoustics Conference, 2016*, 2016.

[9] M. Gruber, P. F. Joseph, and T. P. Chong, "On the mechanisms of serrated airfoil trailing edge noise reduction," *17th AIAA/CEAS Aeroacoustics Conference 2011 (32nd AIAA Aeroacoustics Conference)*, pp. 5–8, June 2011.

[10] D. J. Moreau and C. J. Doolan, "Noise-reduction mechanism of a flat-plate serrated trailing edge," *AIAA Journal*, vol. 51, no. 10, pp. 2513–2522, 2013.

[11] T. P. Chong and A. Vathylakis, "On the aeroacoustic and flow structures developed on a flat plate with a serrated sawtooth trailing edge," *Journal of Sound and Vibration*, vol. 354, pp. 65–90, 2015. [Online]. Available: http://dx.doi.org/10.1016/j.jsv.2015.05.019

[12] T. P. Chong, P. F. Joseph, and M. Gruber, “Airfoil self noise reduction by non-flat plate type trailing edge serrations,” *Applied Acoustics*, vol. 74, no. 4, pp. 607–613, 2013. [Online]. Available: http://dx.doi.org/10.1016/j.apacoust.2012.11.003

[13] A. Vathylakis, T. P. Chong, and P. F. Joseph, “Poro-serrated trailing-edge devices for airfoil self-noise reduction,” *AIAA Journal*, vol. 52, no. 11, pp. 3379–3394, 2015.

[14] T. P. Chong and E. Dubois, “Optimization of the poro-serrated trailing edges for airfoil broadband noise reduction,” *The Journal of the Acoustical Society of America*, vol. 140, no. 2, pp. 1361–1373, 2016.

[15] C. Arce León, D. Ragni, S. Pröbsting, F. Scarano, and J. Madsen, “Flow topology and acoustic emissions of trailing edge serrations at incidence,” *Experiments in Fluids*, vol. 57, no. 5, pp. 1–17, 2016.

[16] C. Arce León, R. Merino-Martínez, D. Ragni, F. Avallone, and M. Snellen, “Boundary layer characterization and acoustic measurements of flow-aligned trailing edge serrations,” *Experiments in Fluids*, vol. 57, no. 12, pp. 1–22, 2016.

[17] C. Arce León, R. Merino-Martínez, D. Ragni, F. Avallone, F. Scarano, S. Pröbsting, M. Snellen, D. G. Simons, and J. Madsen, “Effect of trailing edge serration-flow misalignment on airfoil noise emissions,” *Journal of Sound and Vibration*, vol. 405, pp. 19–33, 2017. [Online]. Available: http://dx.doi.org/10.1016/j.jsv.2017.05.035

[18] F. Avallone, W. C. van der Velden, and D. Ragni, “Benefits of curved serrations on broadband trailing-edge noise reduction,” *Journal of Sound and Vibration*, vol. 400, pp. 167–177, 2017. [Online]. Available: http://dx.doi.org/10.1016/j.jsv.2017.04.007

[19] A. Halimi, B. G. Marinus, and S. Larbi, “Analytical prediction of broadband noise from mini-RPA propellers with serrated edges,” *International Journal of Aeroacoustics*, vol. 18, no. 4-5, pp. 517–535, 2019.

[20] H. M. Lee, Z. Lu, K. M. Lim, J. Xie, and H. P. Lee, “Quieter propeller with serrated trailing edge,” *Applied Acoustics*, vol. 146, pp. 227–236, 2019. [Online]. Available: https://doi.org/10.1016/j.apacoust.2018.11.020

[21] Y. Li, Y. Yang, Y. Liu, Y. Wang, B. Huang, and W. Li, “Aerodynamic and aeroacoustic analyses of a UAV propeller with trailing edge serrations,” *Australian Acoustical Society Annual Conference, AAS 2018*, pp. 12–21, November 2019.

[22] J. M. Nies, M. A. Gageik, I. Klioutchnikov, and H. Olivier, “Investigation of wave phenomena on a blunt airfoil with straight and serrated trailing edges,” *Experiments in Fluids*, vol. 56, no. 7, pp. 1–14, 2015.

[23] T. Bachmann, S. Klän, W. Baumgartner, M. Klaas, W. Schröder, and H. Wagner, “Morphometric characterisation of wing feathers of the barn owl Tyto alba pratincola and the pigeon Columba livia,” *Frontiers in Zoology*, vol. 4, pp. 1–15, 2007.

[24] A. Juknevicius and T. P. Chong, “On the leading edge noise and aerodynamics of thin aerofoil subjected to the straight and curved serrations,” *Journal of Sound and Vibration*, vol. 425, pp. 324–343, 2018. [Online]. Available: https://doi.org/10.1016/j.jsv.2018.02.038

[25] S. Ito, “Aerodynamic influence of leading-edge serrations on an airfoil in a low Reynolds number: A study of an owl wing with leading edge serrations,” *Journal of Biomechanical Science and Engineering*, vol. 4, no. 1, pp. 117–122, 2009.

[26] G.-q. LIANG, J.-c. WANG, Y. CHEN, C.-h. ZHOU, J. LIANG, and L.-q. REN, “The Study of Owl’s Silent Flight and Noise Reduction on Fan Vane with Bionic Structure,” *Advances in Natural Science*, vol. 3, no. 2, pp. 192–198, 2010.

[27] F. G. Collins, “Boundary-layer control on wings using sound and leading-edge serrations,” *AIAA Journal*, vol. 19, no. 2, pp. 129–130, 1981.

[28] A. S. Hersh and R. E. Hayden, “Aerodynamic sound radiation from lifting surfaces with and without leading-edge serrations,” *Report CR-114370, NASA*, September 1972.

[29] P. T. Soderman, “Aerodynamic effects of leading-edge serrations on a two-dimensional airfoil,” *NASA Technical Memorandum TM X-2643*, September 1972.

[30] ——, “Leading edge serrations which reduce the noise of low-speed rotors,” *NASA Technical Note TN D-7371*, August 1973.

[31] A. S. Hersh, P. T. Soderman, and R. E. Hayden, “Investigation of acoustic effects of leading-edge serrations on airfoils,” *Journal of Aircraft*, vol. 11, no. 4, pp. 197–202, 1974.

[32] S. Narayanan, P. Chaitanya, S. Haeri, P. Joseph, J. W. Kim, and C. Polacsek, “Airfoil noise reductions through leading edge serrations,” *Physics of Fluids*, vol. 27, no. 2, 2015.

[33] S. Narayanan, P. Joseph, S. Haeri, J. W. Kim, P. Chaitanya, and C. Polacsek, “Noise reduction studies from the leading edge of serrated flat plates,” *20th AIAA/CEAS Aeroacoustics Conference*, pp. 1–14, June 2014.

[34] T. P. Chong, A. Vathylakis, A. Mcewen, F. Kemsley, C. Muhammad, and S. Siddiqi, "Aeroacoustic and aerodynamic performances of an aerofoil subjected to sinusoidal leading edges," *21st AIAA/CEAS Aeroacoustics Conference*, 2015.

[35] P. Chaitanya, S. Narayanan, P. Joseph, C. Vanderwel, J. Turner, J. W. Kim, and B. Ganapathisubramani, "Broadband noise reduction through leading edge serrations on realistic aerofoils," *21st AIAA/CEAS Aeroacoustics Conference*, pp. 1–29, June 2016.

[36] P. Chaitanya, P. Joseph, S. Narayanan, C. Vanderwel, J. Turner, J. W. Kim, and B. Ganapathisubramani, "Performance and mechanism of sinusoidal leading edge serrations for the reduction of turbulence-aerofoil interaction noise," *Journal of Fluid Mechanics*, vol. 818, pp. 435–464, 2017.

[37] M. Roger, C. Schram, and L. de Santana, "Reduction of airfoil turbulence-impingement noise by means of leading-edge serrations and/or porous materials," *19th AIAA/CEAS Aeroacoustics Conference*, p. 105, 2013.

[38] T. M. Biedermann, T. P. Chong, F. Kameier, and C. O. Paschereit, "Statistical-empirical modeling of airfoil noise subjected to leading-edge serrations," *AIAA Journal*, vol. 55, no. 9, pp. 3128–3142, 2017.

[39] V. Clair, C. Polacsek, T. Le Garrec, G. Reboul, M. Gruber, and P. Joseph, "Experimental and numerical investigation of turbulence-airfoil noise reduction using wavy edges," *AIAA Journal*, vol. 51, no. 11, pp. 2695–2713, 2013.

[40] S. Haeri, J. W. Kim, S. Narayanan, and P. Joseph, "3D calculations of aerofoil-turbulence interaction noise and the effect of wavy leading edges," *20th AIAA/CEAS Aeroacoustics Conference*, pp. 1–15, June 2014.

[41] J. W. Kim, S. Haeri, and P. F. Joseph, "On the reduction of aerofoil-turbulence interaction noise associated with wavy leading edges," *Journal of Fluid Mechanics*, vol. 792, pp. 526–552, 2016.

[42] F. Gea-Aguilera, J. Gill, D. Angland, and X. Zhang, "Wavy leading edge airfoils interacting with anisotropic turbulence," *23rd AIAA/CEAS Aeroacoustics Conference, 2017*, pp. 1–16, June 2017.

[43] P. Chaitanya and P. Joseph, "Slitted leading edge profiles for the reduction of turbulence-aerofoil interaction noise," *The Journal of the Acoustical Society of America*, vol. 143, no. 6, pp. 3494–3504, 2018.

[44] P. Chaitanya, S. Narayanan, P. Joseph, and J. W. Kim, "Leading edge serration geometries for significantly enhanced leading edge noise reductions," *22nd AIAA/CEAS Aeroacoustics Conference, 2016*, May 2016.

[45] I. S. Amado, "Experimental Comparison of Planar and Coaxial Rotor Configurations in Multi-rotors," *Master Thesis, Instituto Superior Técnico*, September 2017.

[46] J. G. Leishman, *Principles of Helicopter Aerodynamics*. Cambridge University Press, 2006.

[47] "Airfoil tools," http://airfoiltools.com/airfoil/details?airfoil=naca0018-il#polars, [Online. Accessed on 16/04/2020].

[48] "Properties table," https://www.simplify3d.com/support/materials-guide/properties-table/, [Online. Accessed on 02/04/2020].

[49] *NI USB-9237 User Guide And Specifications*. National Instruments, 2007.

[50] *NI 6353 Device Specifications*. National Instruments, 2016.

[51] *NI CB-68LP/CB-68LPR User Guide*. National Instruments, 2013.

[52] *Model 482C15 Four-Channel, ICP Sensor Signal Conditioner Installation and Operating Manual*. PCB Piezotronics, 2017.

[53] "Current and voltage sensor specifications," https://www.pitlab.com/fpv-system/current-sensor.html, [Online. Accessed on 13/06/2020].

[54] "Current transducer ltsr 25-np," http://docs-europe.electrocomponents.com/webdocs/06c4/0900766b806c43de.pdf, [Online. Accessed on 13/06/2020].

[55] "Lm35 precision centigrade temperature sensors," https://www.engineersgarage.com/sites/default/files/LM35.PDF, [Online. Accessed on 13/06/2020].

[56] "Reflective optical sensor with transistor output," https://www.vishay.com/docs/83751/cny70.pdf, [Online. Accessed on 13/06/2020].

[57] *Brüel & Kjær 20 kHz Precision Array Microphone — Type 4958*. Product Manual Data, 2011.

[58] F. Pereira, "Development and testing of an acoustic measurement system for the IST Aeroacoustic Wind Tunnel," *Master Thesis, Instituto Superior Técnico*, November 2017.

[59] R. Oshana, *DSP Software Development Techniques for Embedded and Real-Time Systems*. Elsevier Ltd, 2006. [Online]. Available: https://doi.org/10.1016/B978-0-7506-7759-2.X5000-5

[60] S. F. Leung and Y. Link, "Comparison and analysis of strain gauge balance calibration matrix mathematical models," *Report DST-TR-0857, Defense Science and Technology Organization*, August 1999.

A

Noise Results

In this section the noise results are displayed. Figures A.1 to A.7 contain the SPL distribution of the seven rotors and the background noise, for the three microphones at the different rotation speeds tested. Figures A.8 to A.14 show the A-weighted Third-Octave bands distribution of the noise. Figure A.15 presents the LAeq measured for every test, and Figure A.16 the A-weighted Total Band Power. Figure A.17 shows the A-weighted filter applied throughout this thesis.

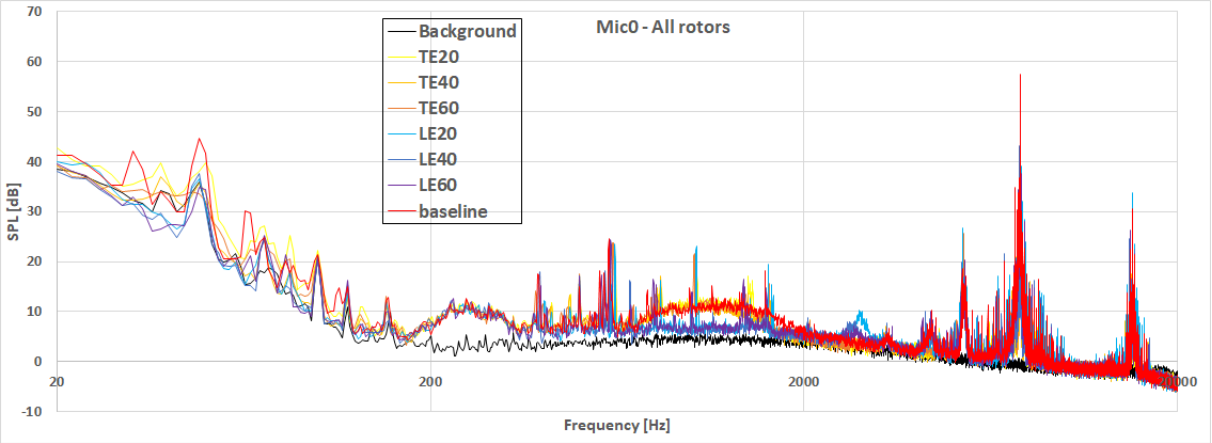

(a) Microphone 0.

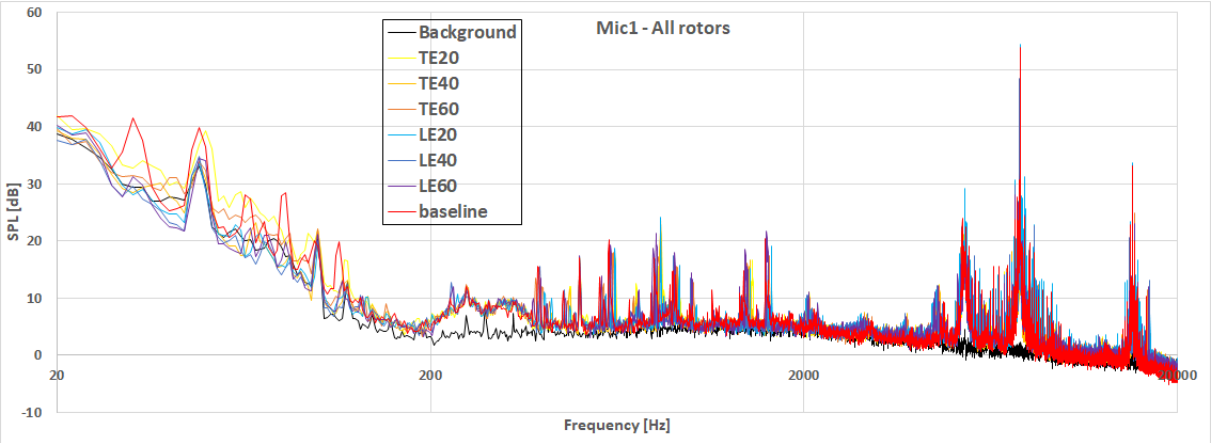

(b) Microphone 1.

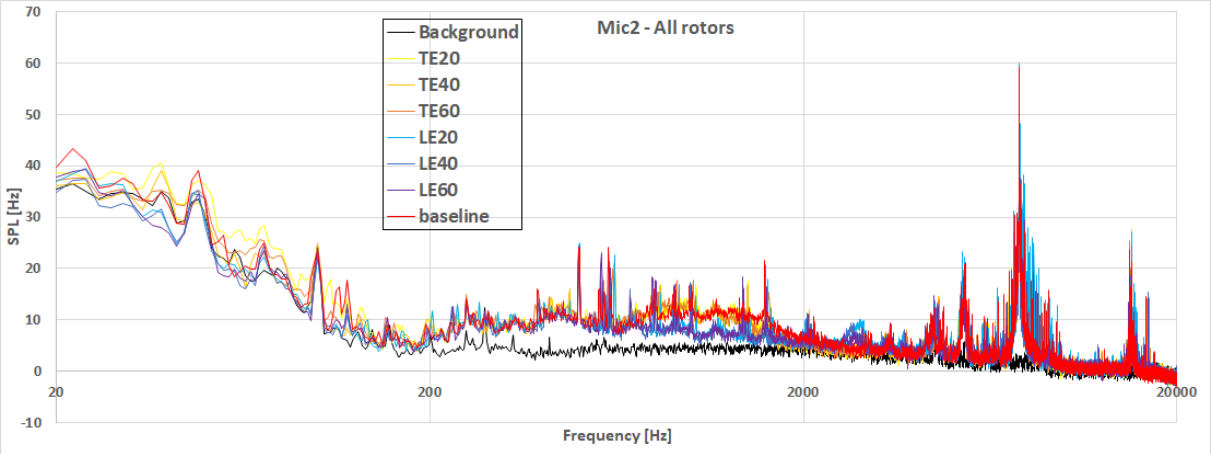

(c) Microphone 2.

Figure A.1: SPL measured at 1000 RPM.

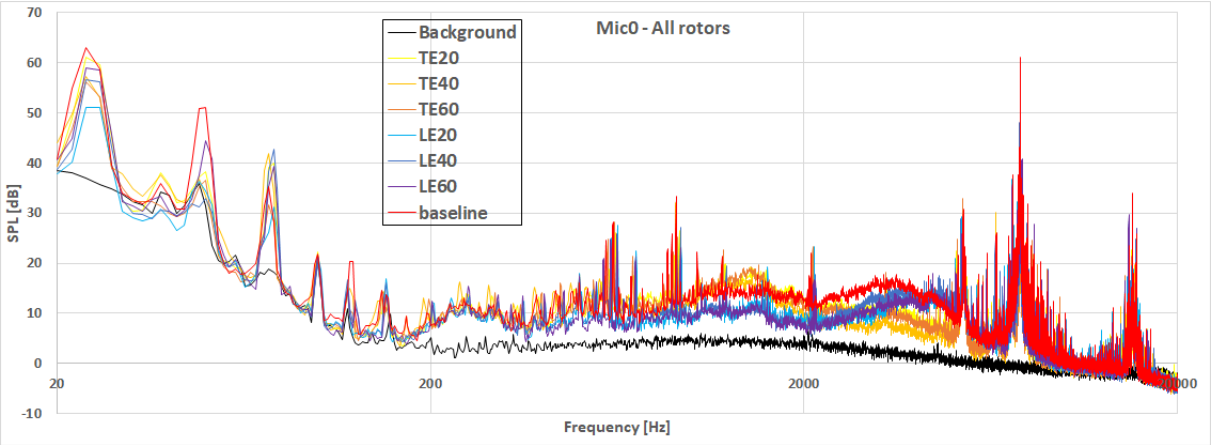

(a) Microphone 0.

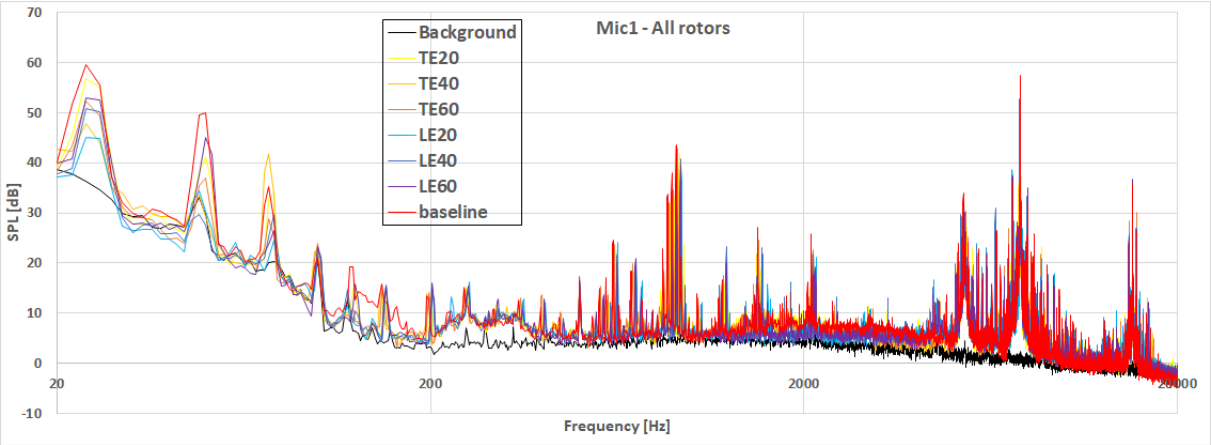

(b) Microphone 1.

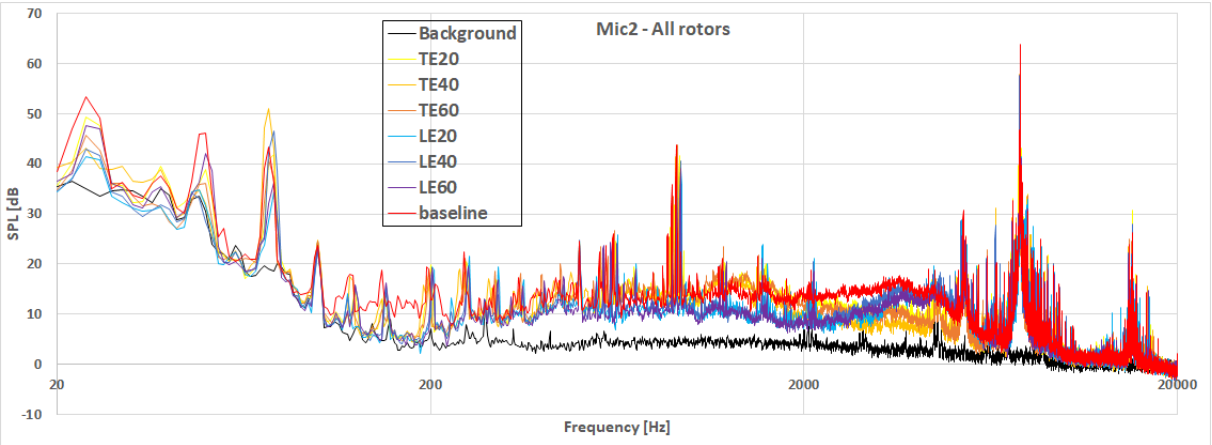

(c) Microphone 2.

Figure A.2: SPL measured at 1500 RPM.

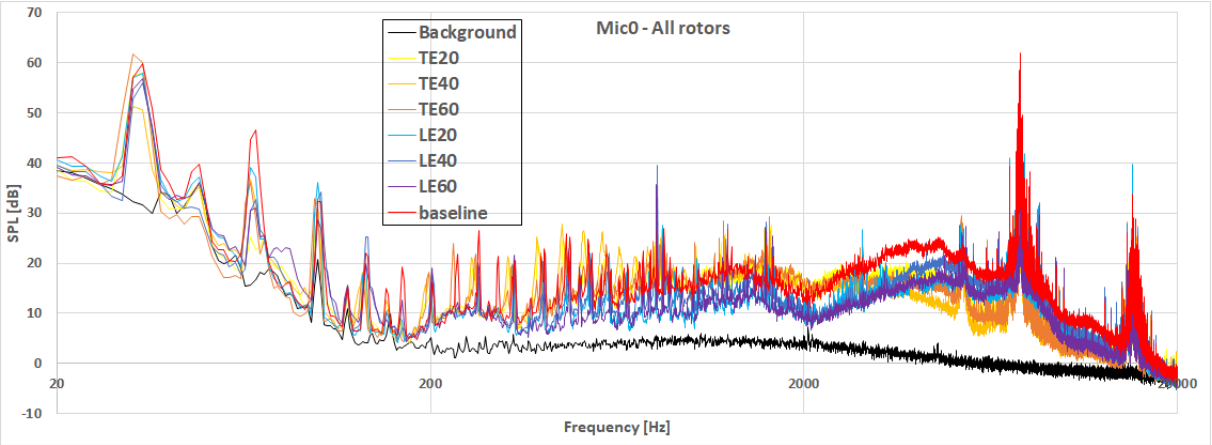

(a) Microphone 0.

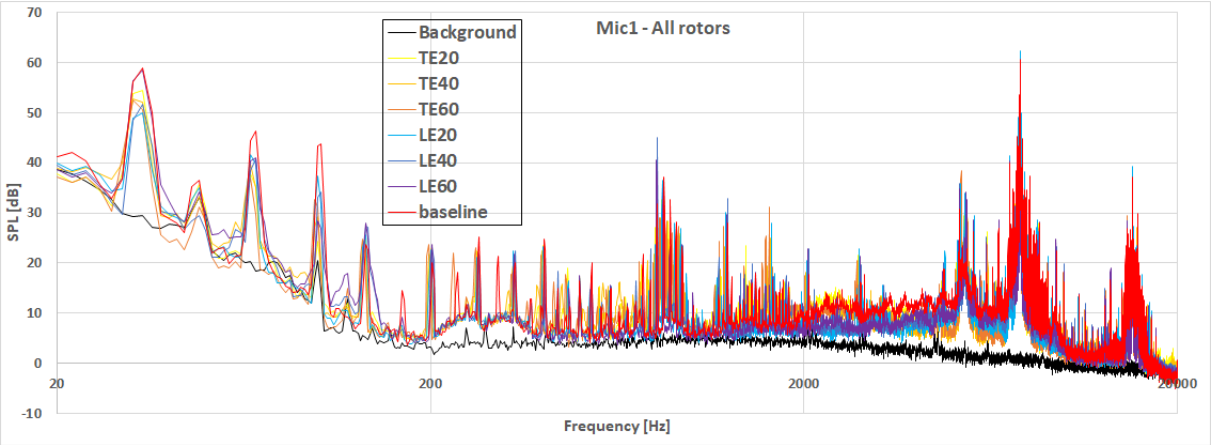

(b) Microphone 1.

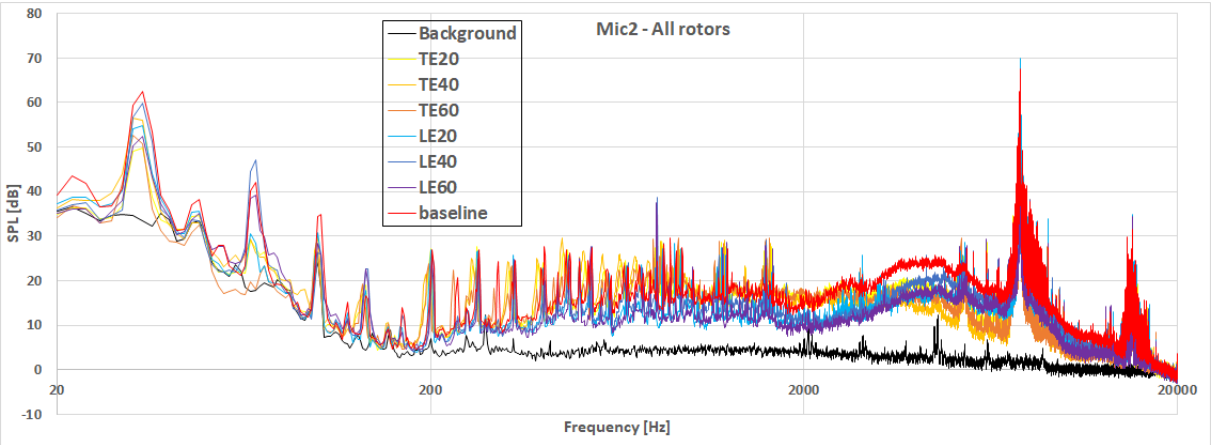

(c) Microphone 2.

Figure A.3: SPL measured at 2000 RPM.

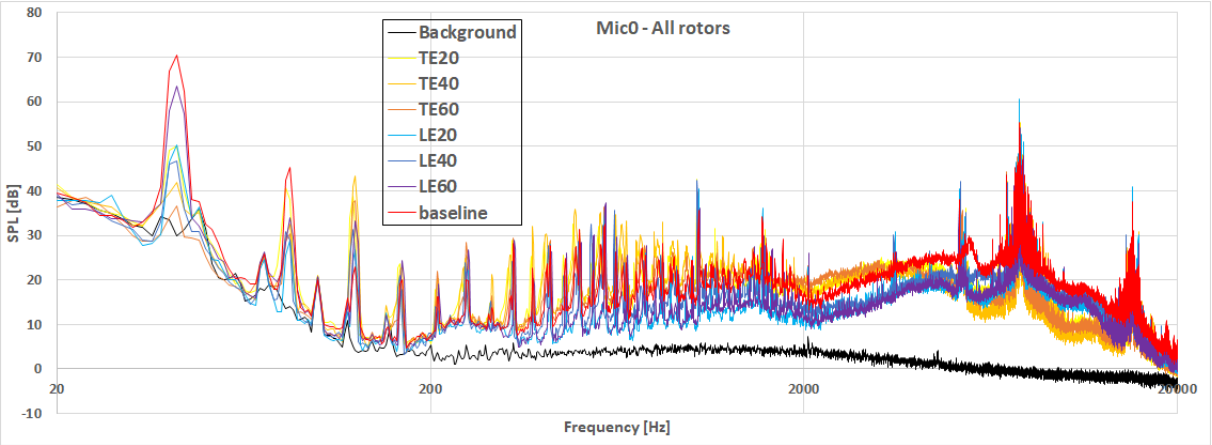

(a) Microphone 0.

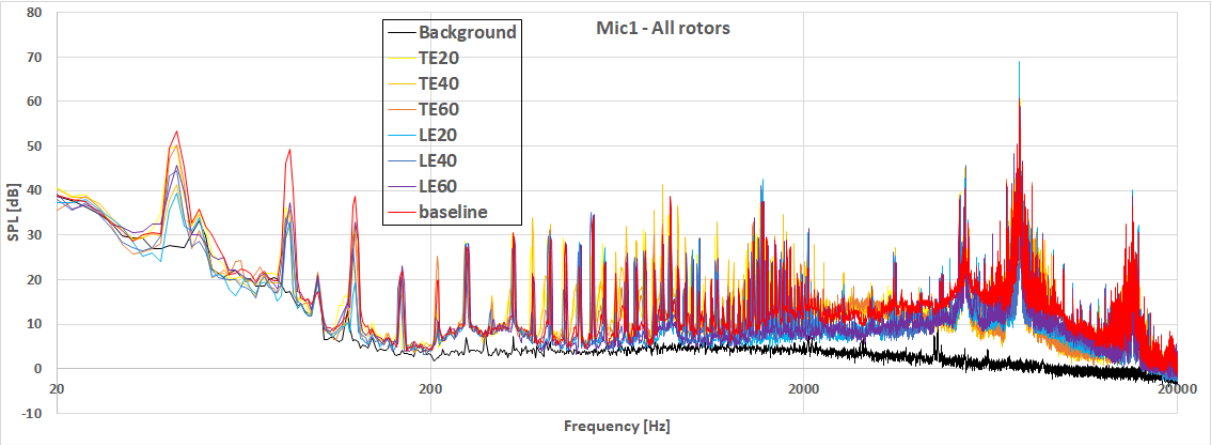

(b) Microphone 1.

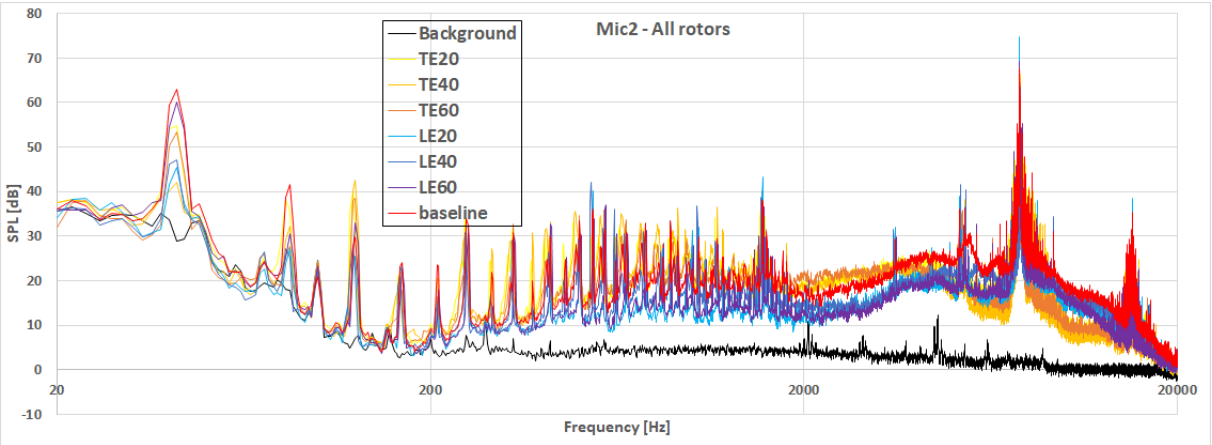

(c) Microphone 2.

Figure A.4: SPL measured at 2500 RPM.

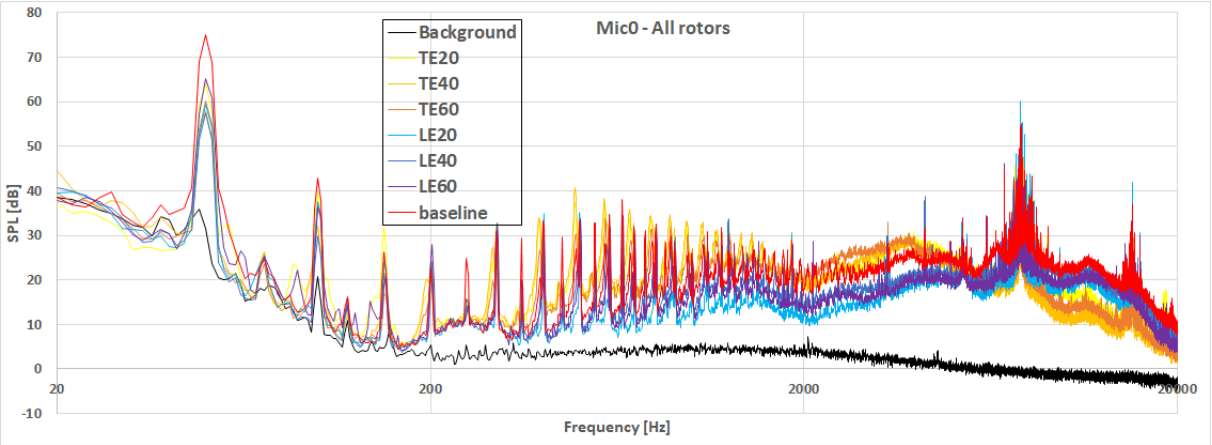

(a) Microphone 0.

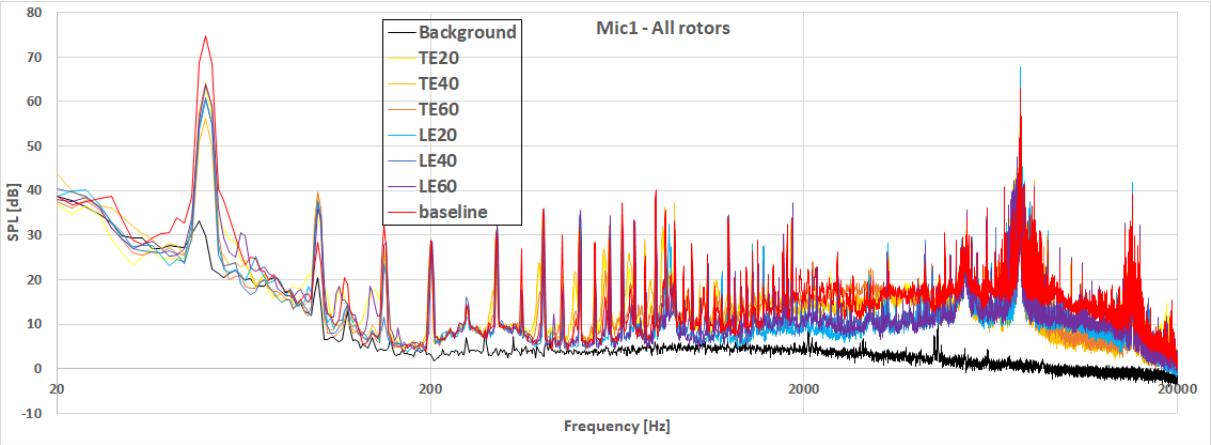

(b) Microphone 1.

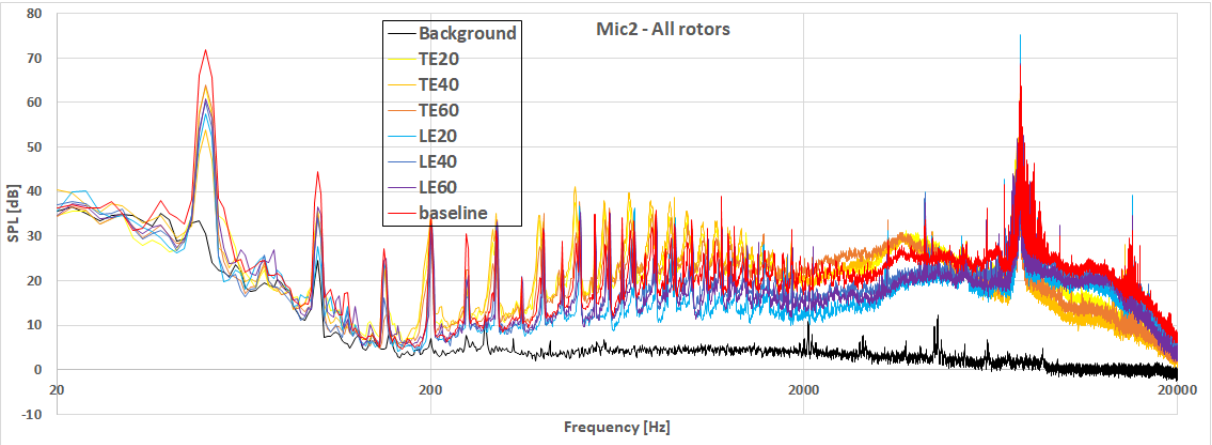

(c) Microphone 2.

Figure A.5: SPL measured at 3000 RPM.

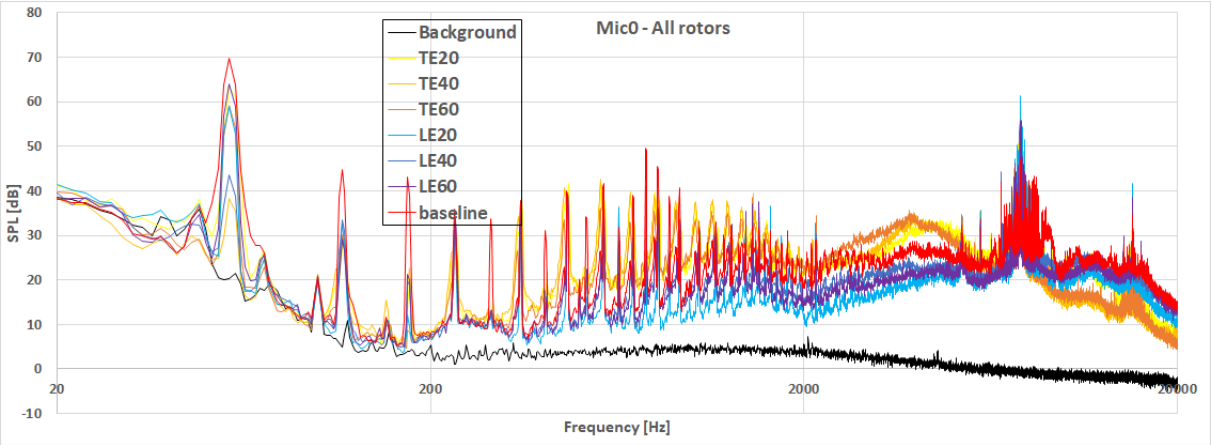

(a) Microphone 0.

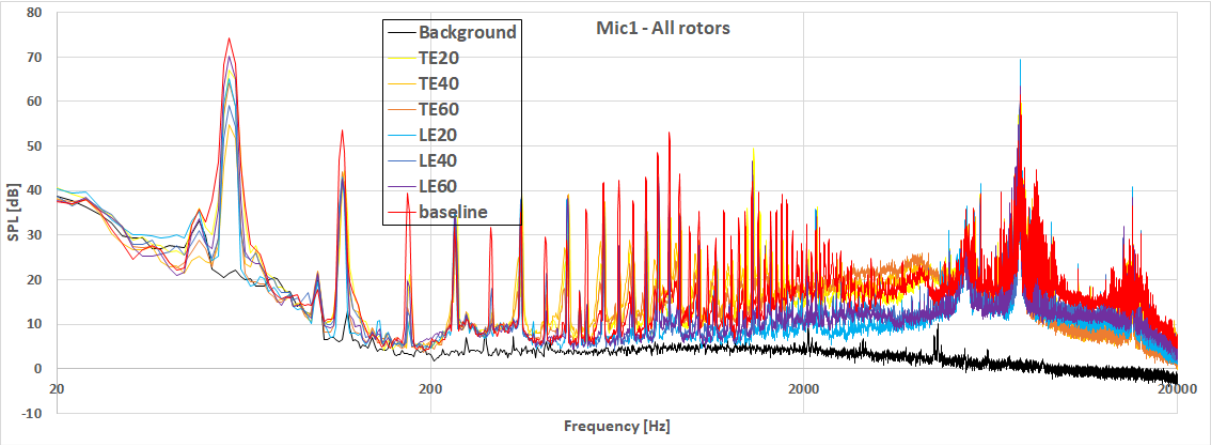

(b) Microphone 1.

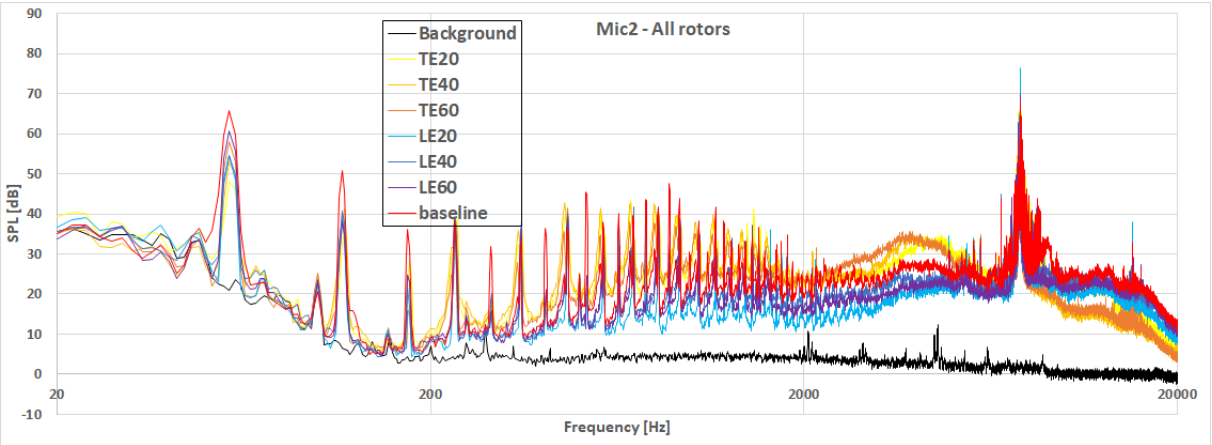

(c) Microphone 2.

Figure A.6: SPL measured at 3500 RPM.

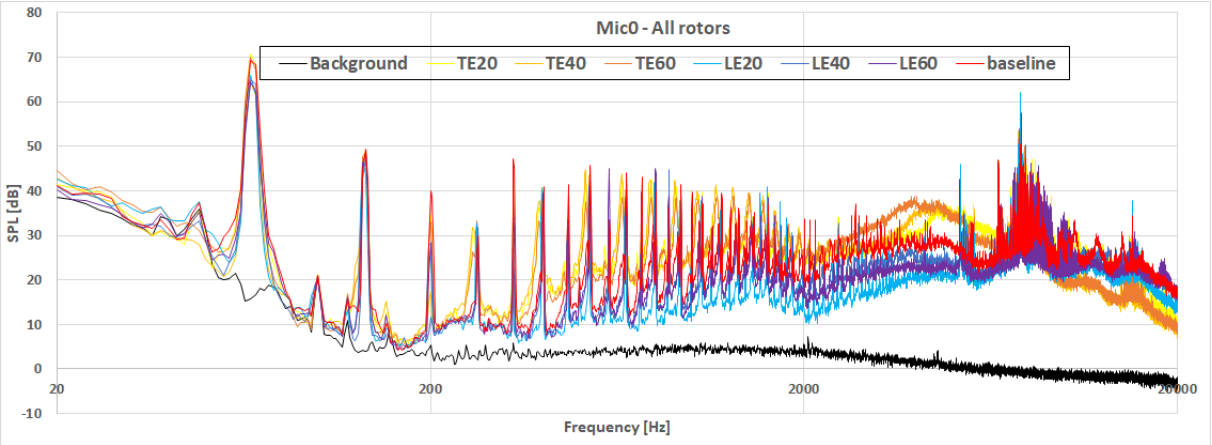

(a) Microphone 0.

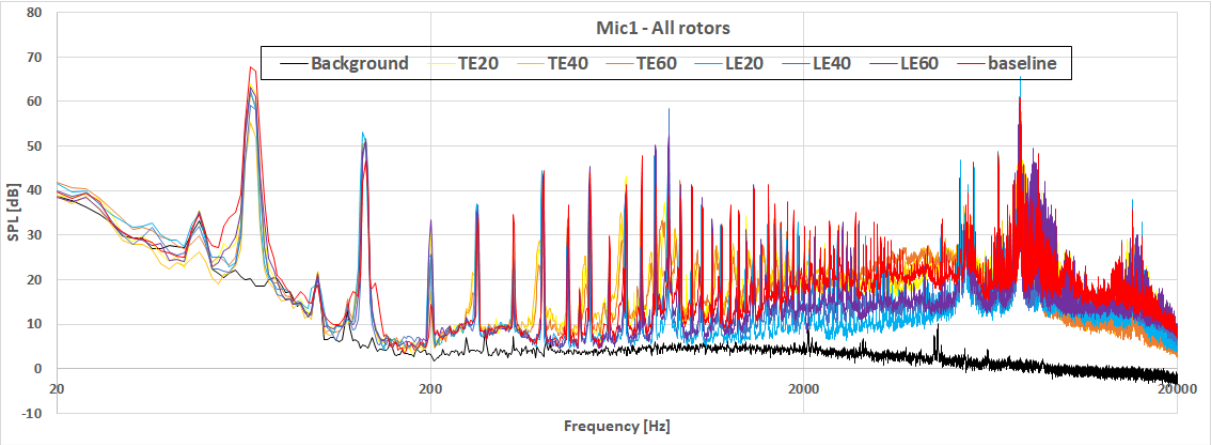

(b) Microphone 1.

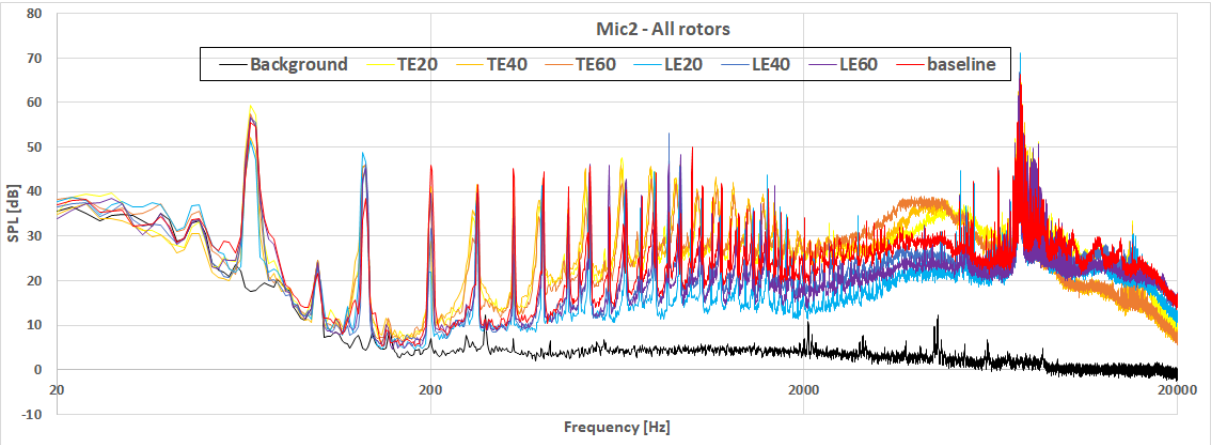

(c) Microphone 2.

Figure A.7: SPL measured at 4000 RPM.

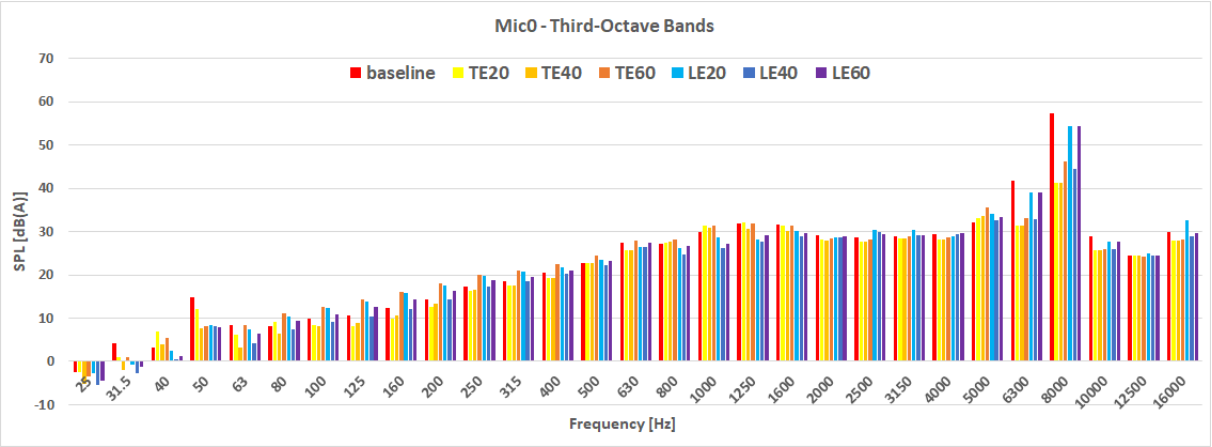

(a) Microphone 0.

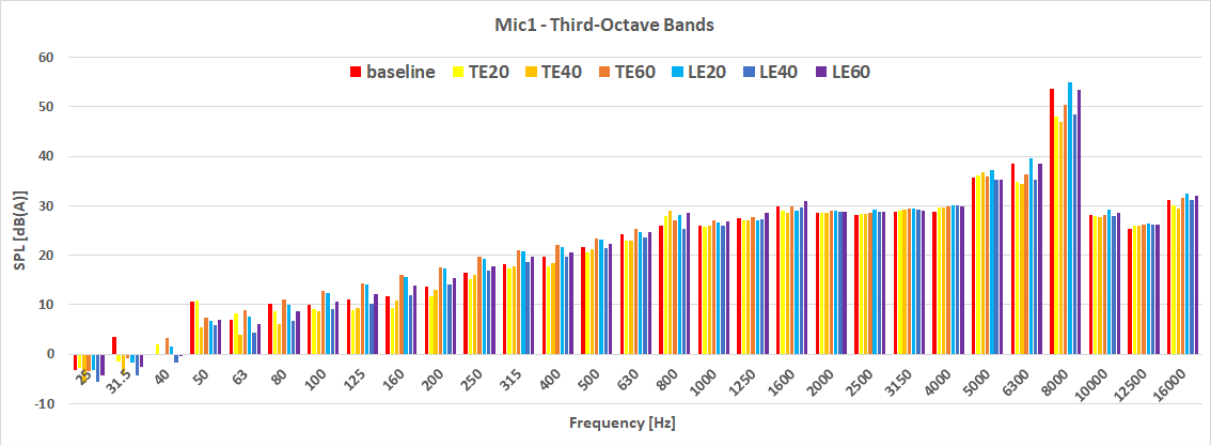

(b) Microphone 1.

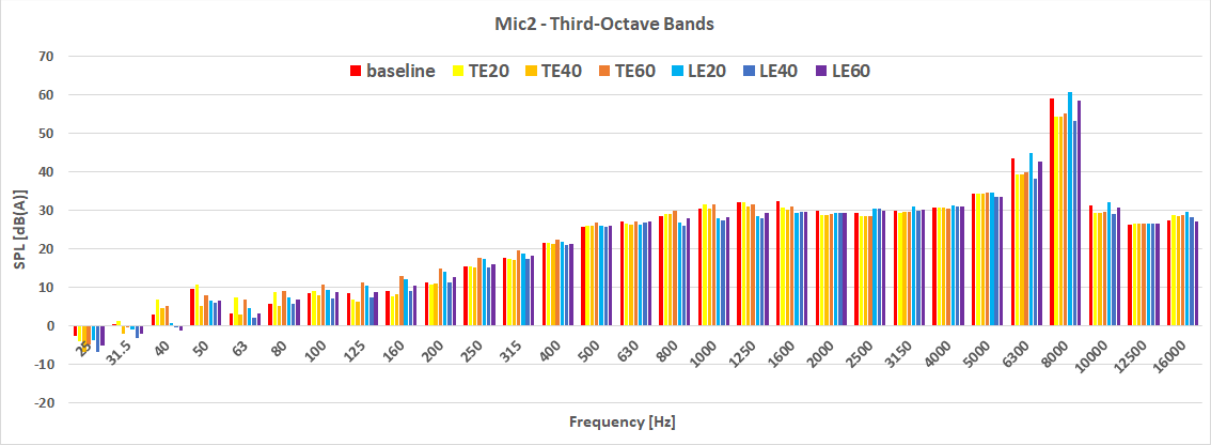

(c) Microphone 2.

Figure A.8: 1/3 Octave bands measured at 1000 RPM.

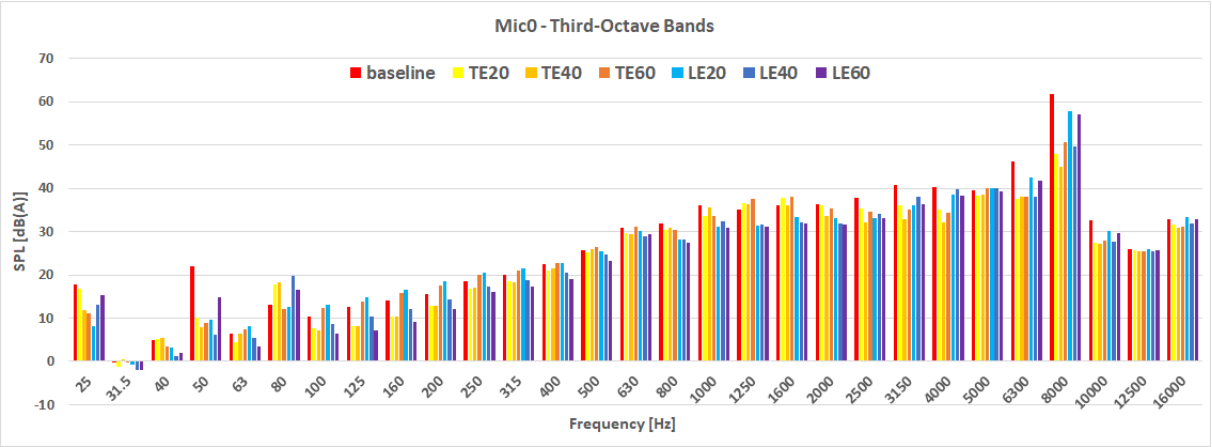

(a) Microphone 0.

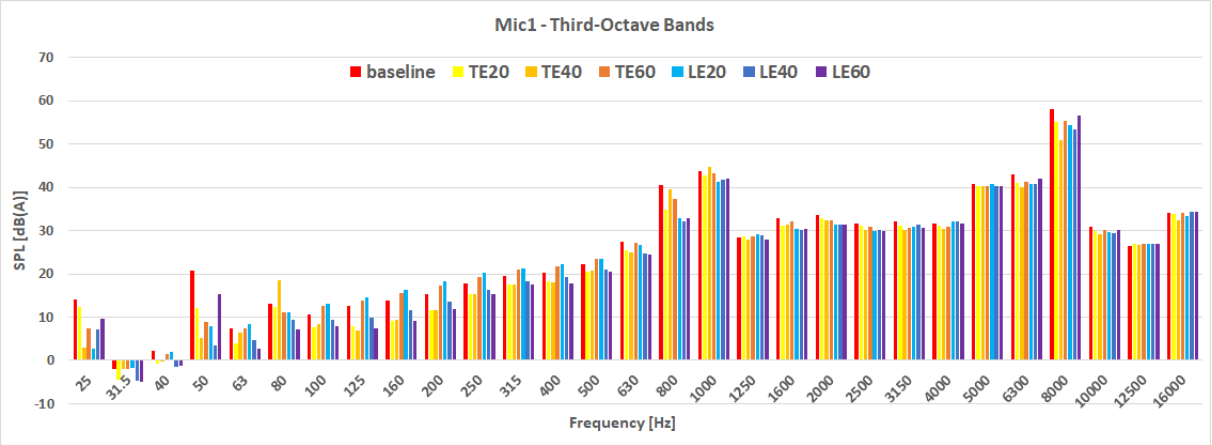

(b) Microphone 1.

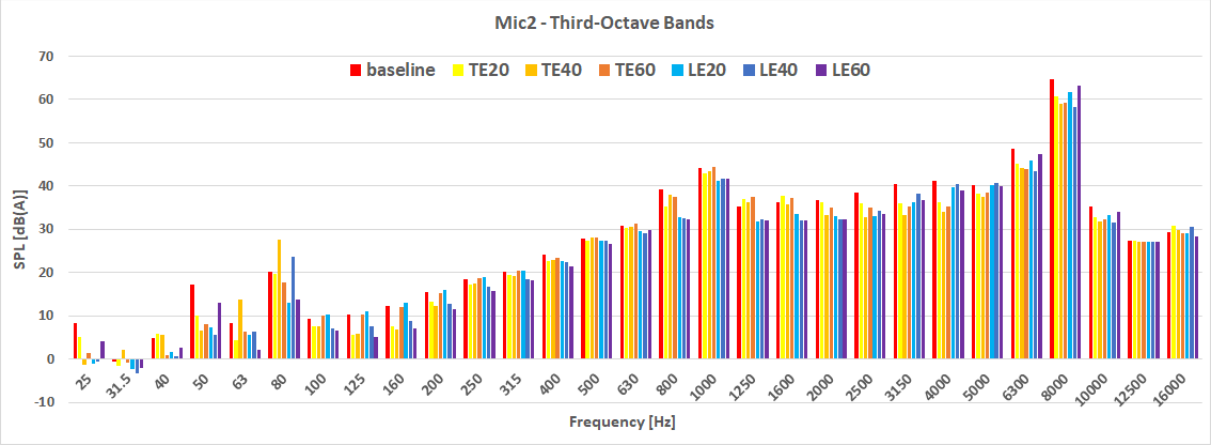

(c) Microphone 2.

Figure A.9: 1/3 Octave bands measured at 1500 RPM.

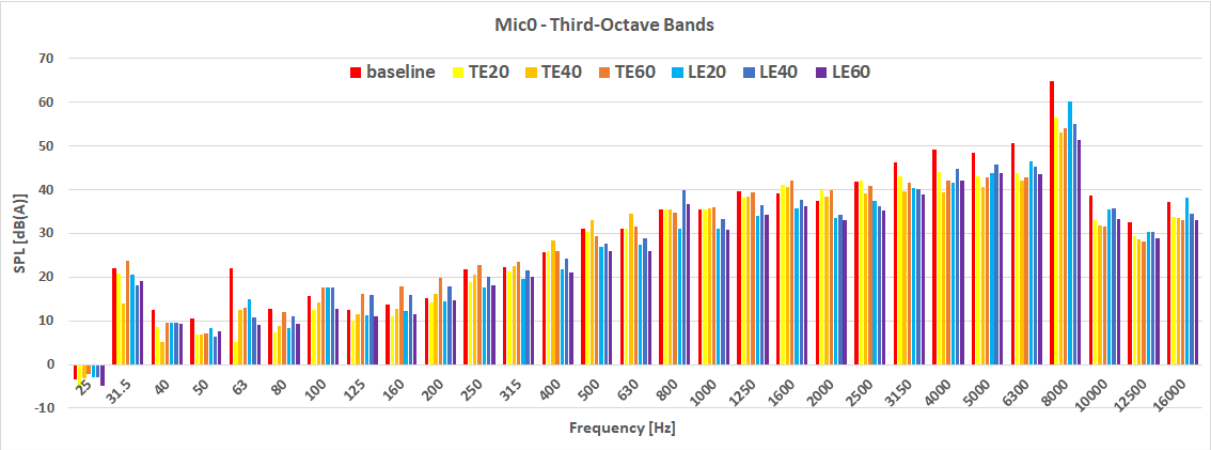

(a) Microphone 0.

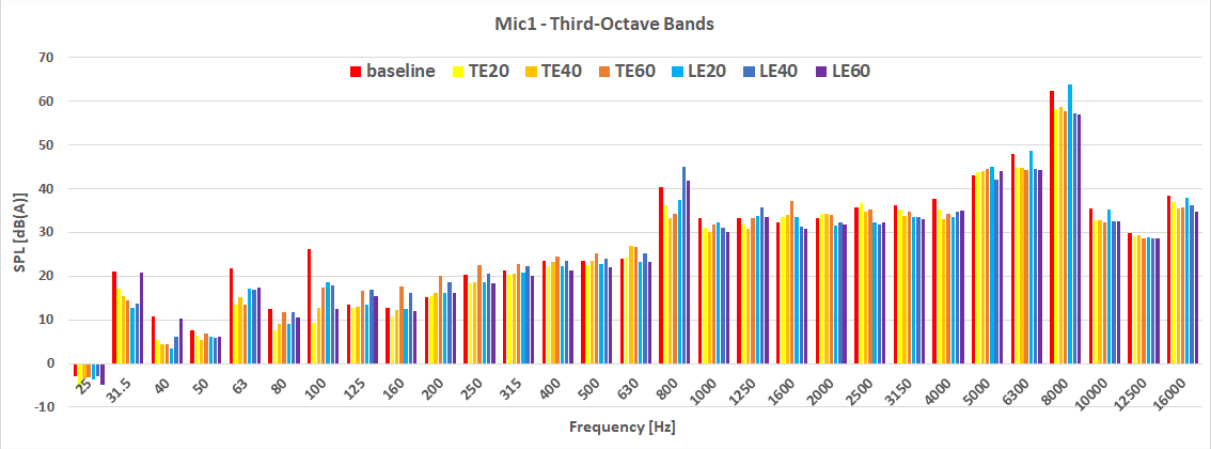

(b) Microphone 1.

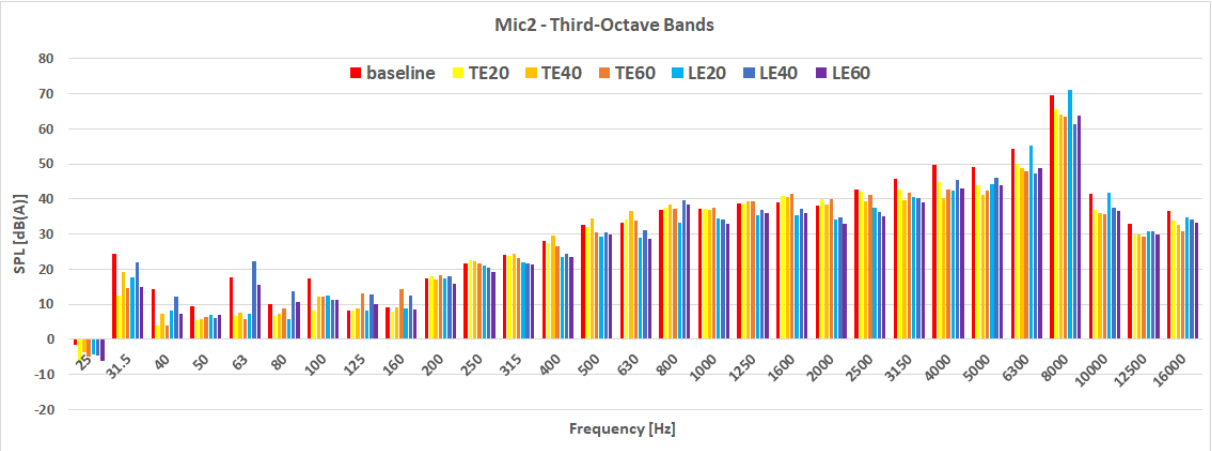

(c) Microphone 2.

Figure A.10: 1/3 Octave bands measured at 2000 RPM.

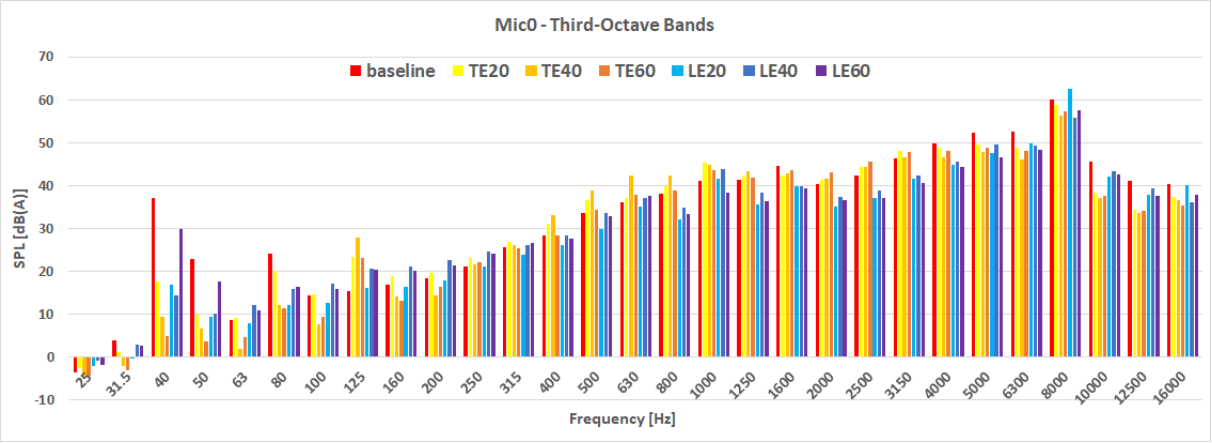

(a) Microphone 0.

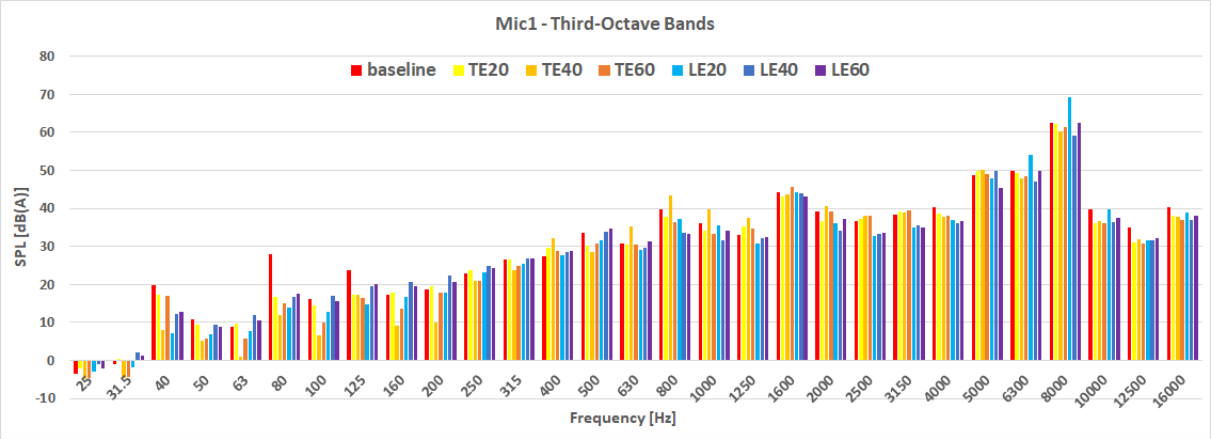

(b) Microphone 1.

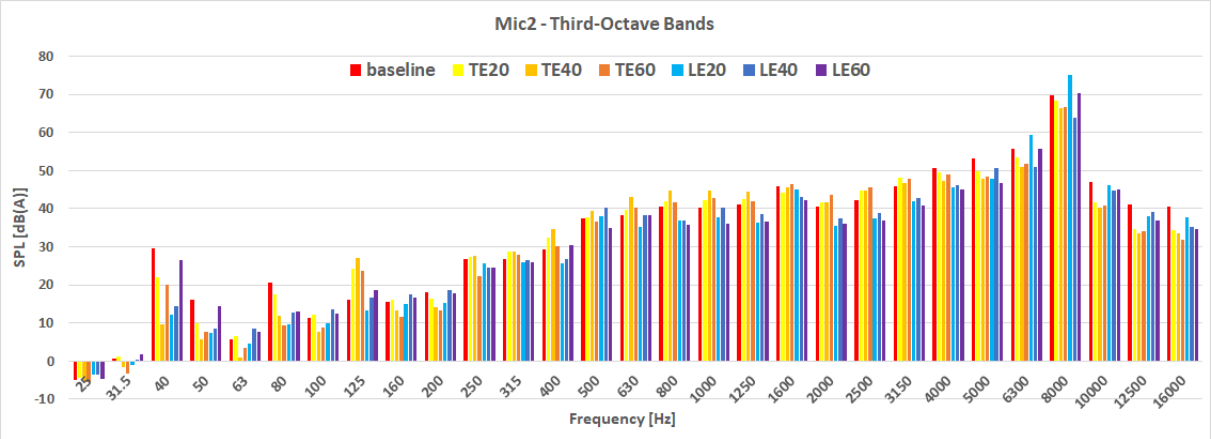

(c) Microphone 2.

Figure A.11: 1/3 Octave bands measured at 2500 RPM.

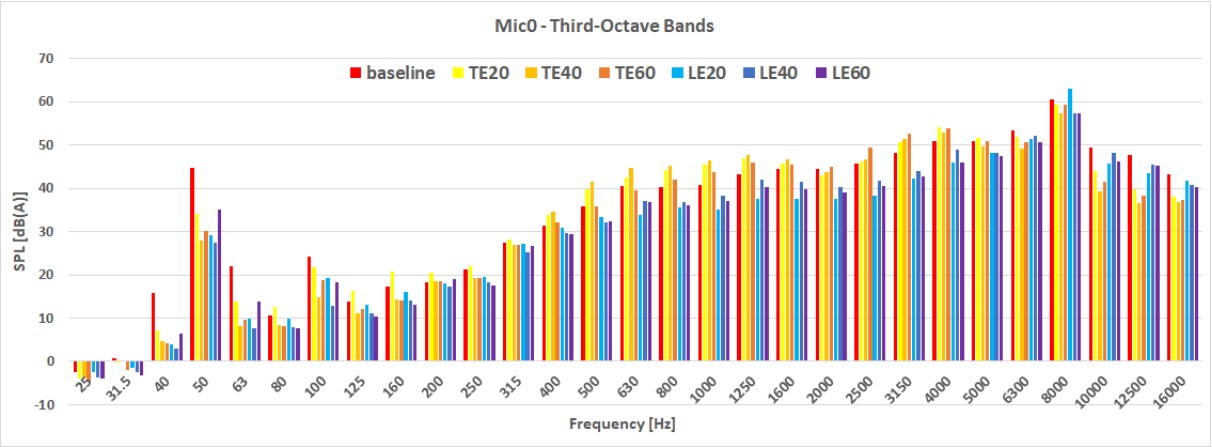

(a) Microphone 0.

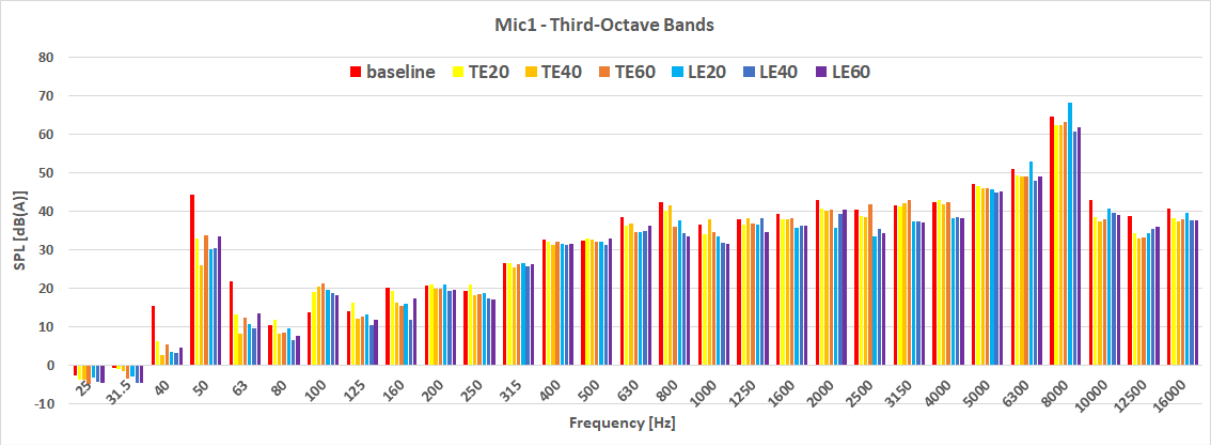

(b) Microphone 1.

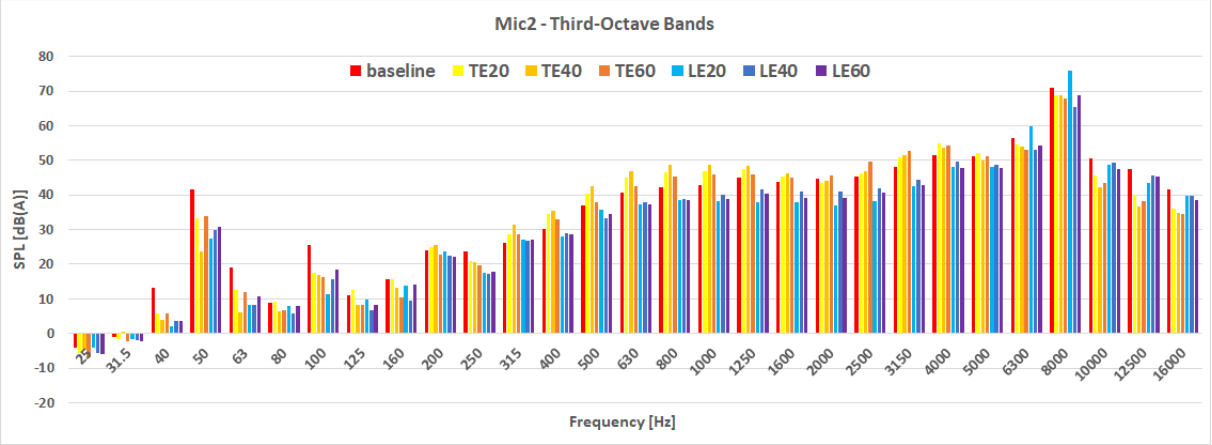

(c) Microphone 2.

Figure A.12: 1/3 Octave bands measured at 3000 RPM.

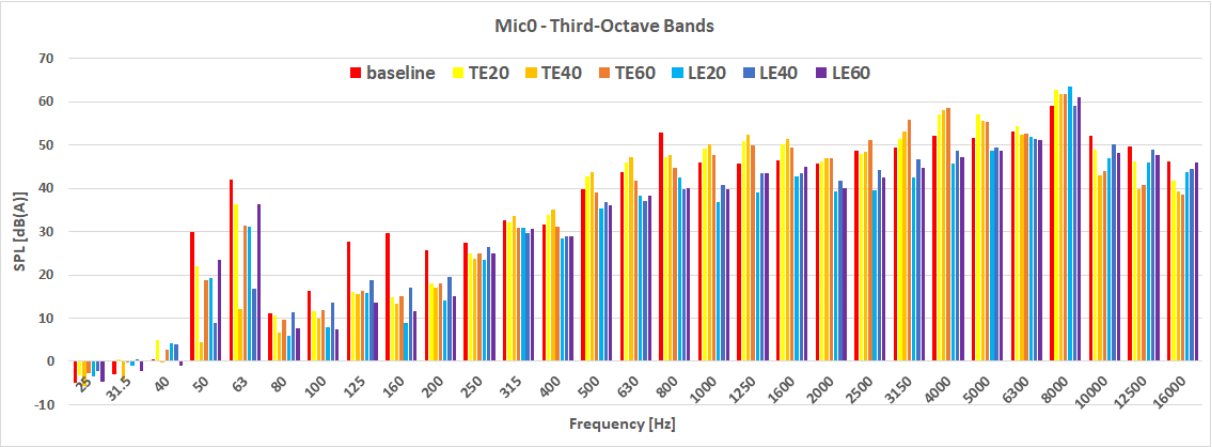

(a) Microphone 0.

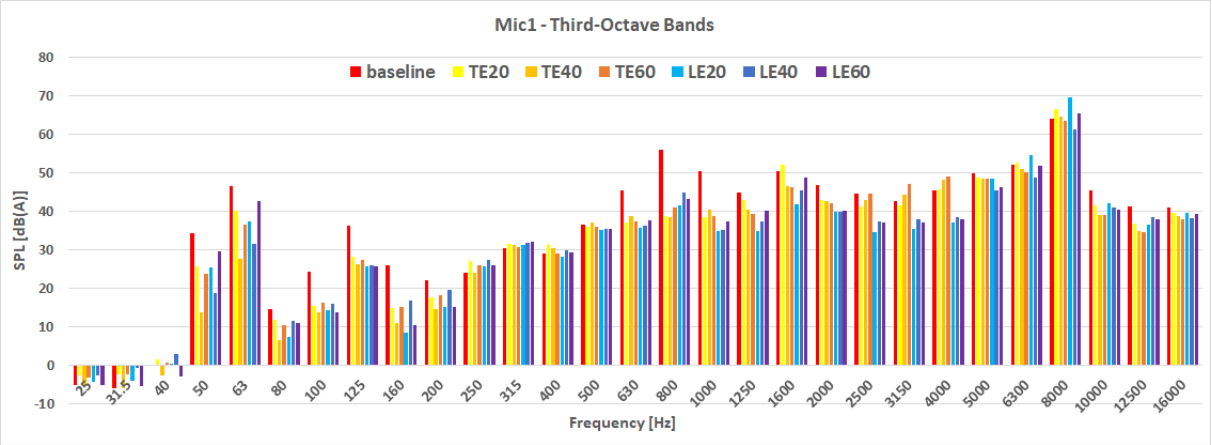

(b) Microphone 1.

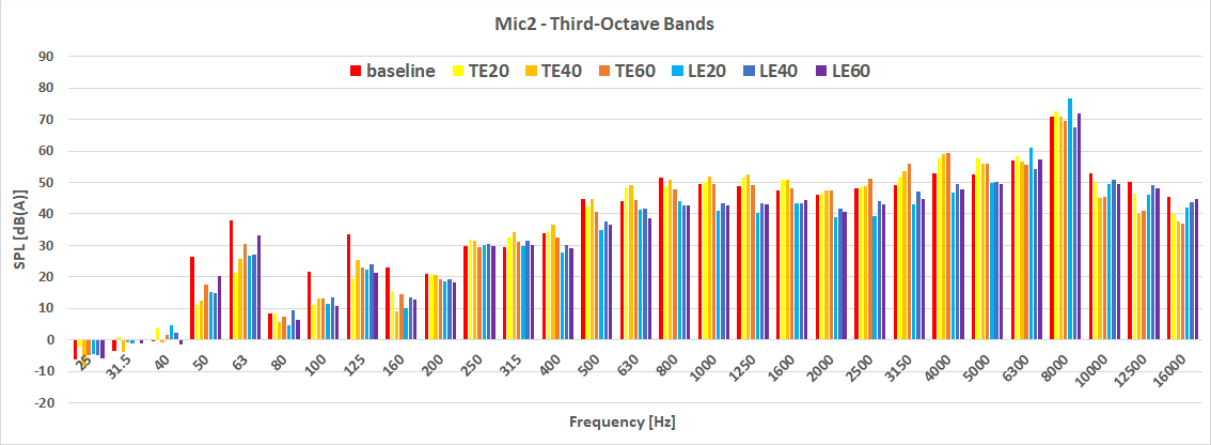

(c) Microphone 2.

Figure A.13: 1/3 Octave bands measured at 3500 RPM.

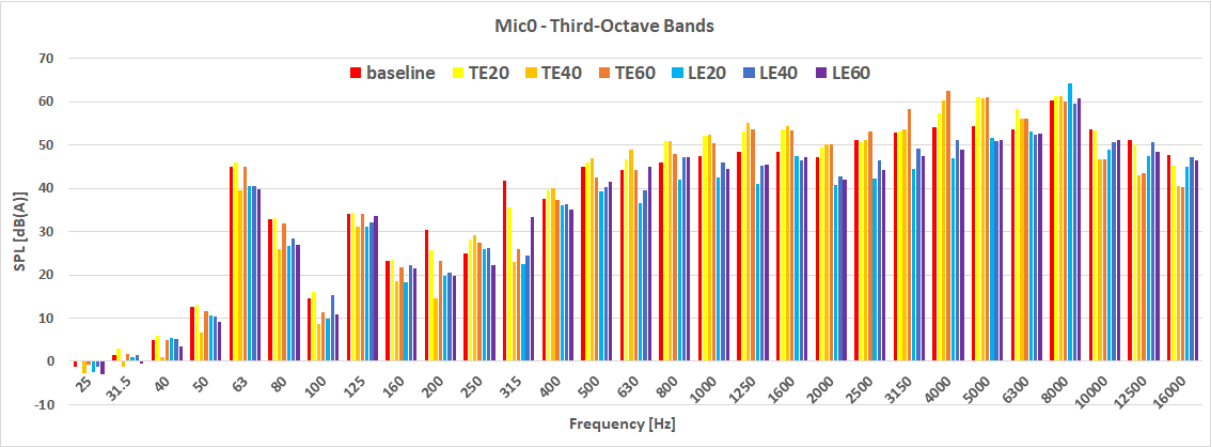

(a) Microphone 0.

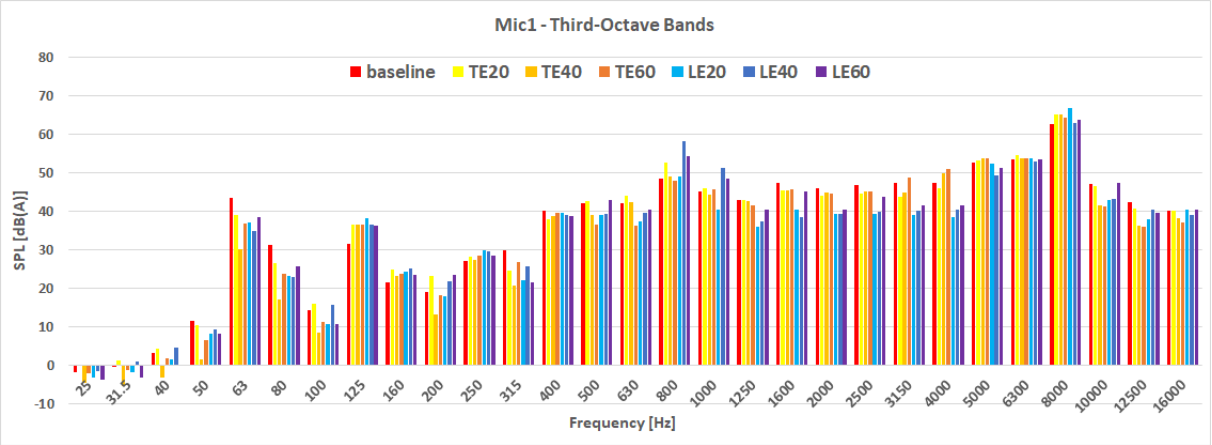

(b) Microphone 1.

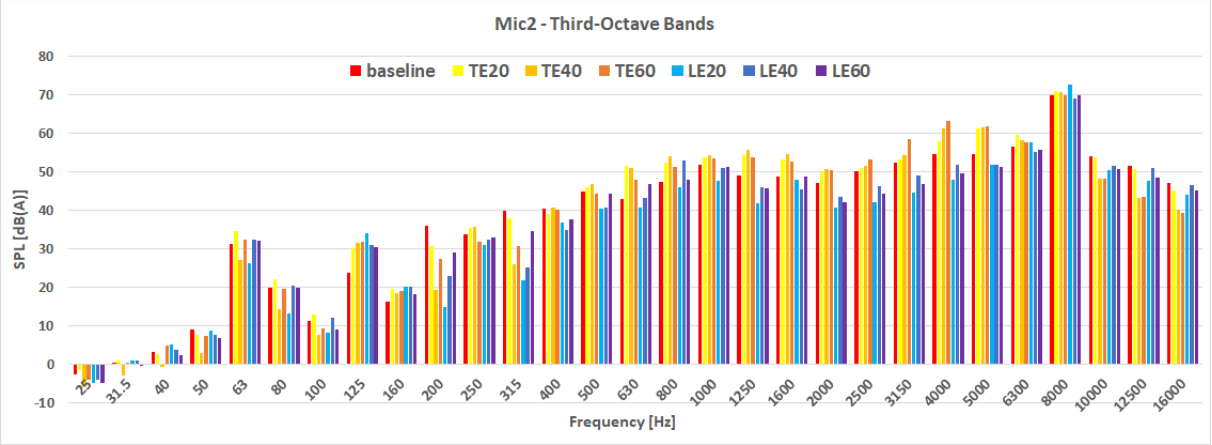

(c) Microphone 2.

Figure A.14: 1/3 Octave bands measured at 4000 RPM.

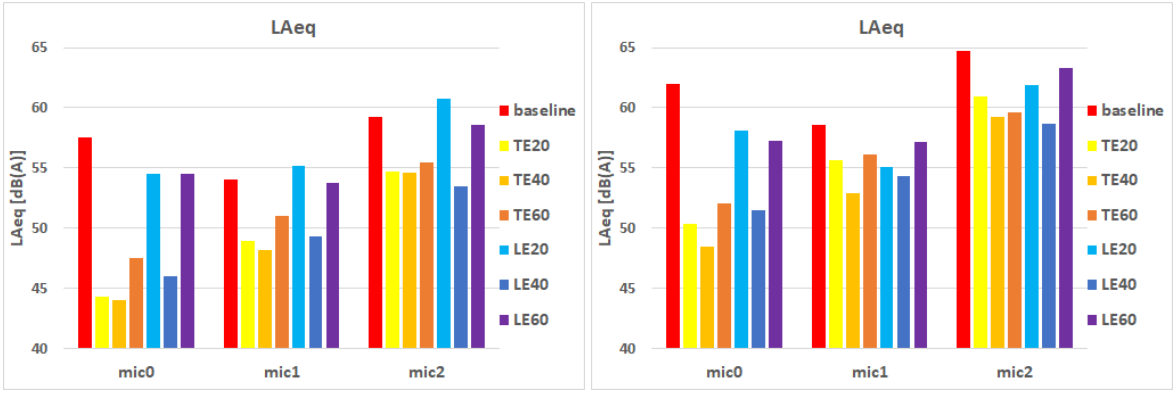

(a) 1000 RPM. **(b)** 1500 RPM.

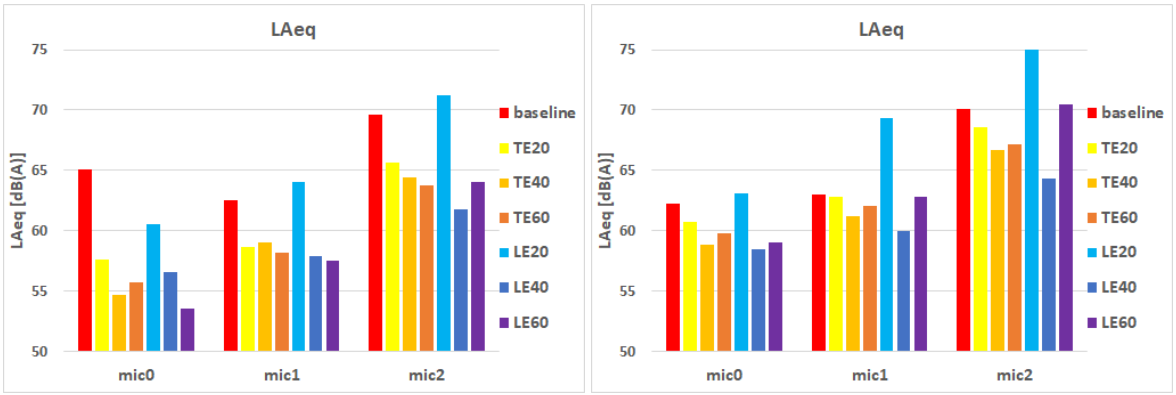

(c) 2000 RPM. **(d)** 2500 RPM.

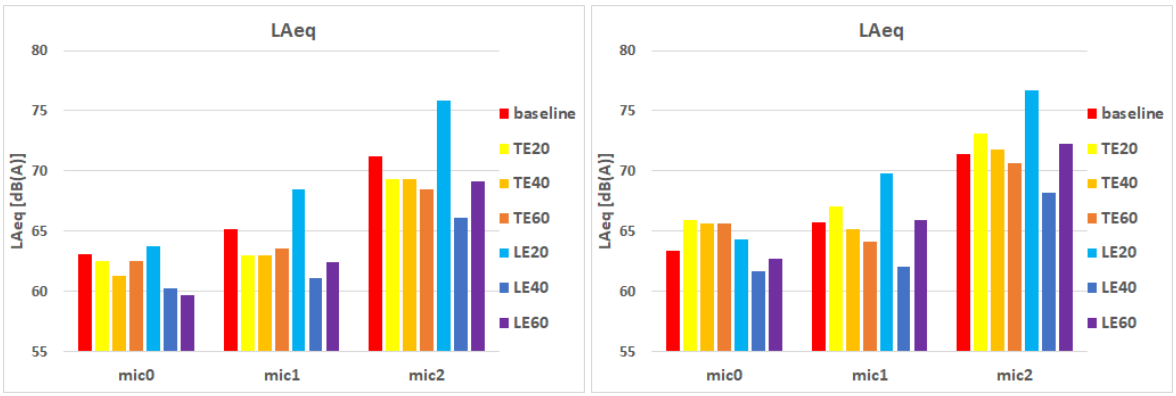

(e) 3000 RPM. **(f)** 3500 RPM.

Figure A.15: LAeq measured for every rotation speed.

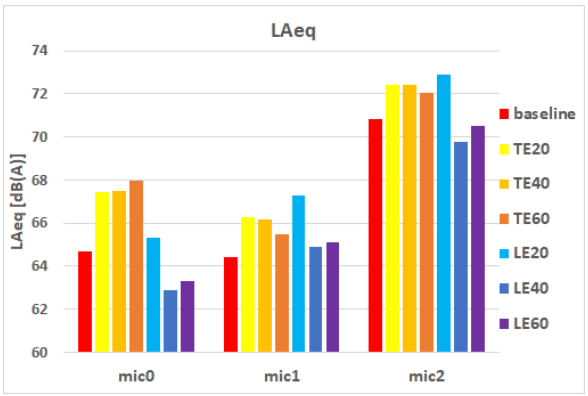

(g) 4000 RPM.

Figure A.15: LAeq measured for every rotation speed (cont.).

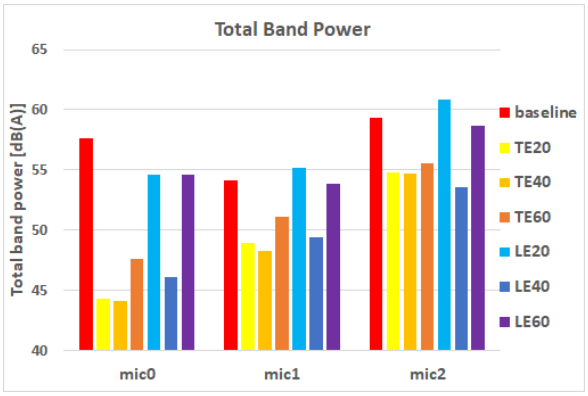

(a) 1000 RPM.

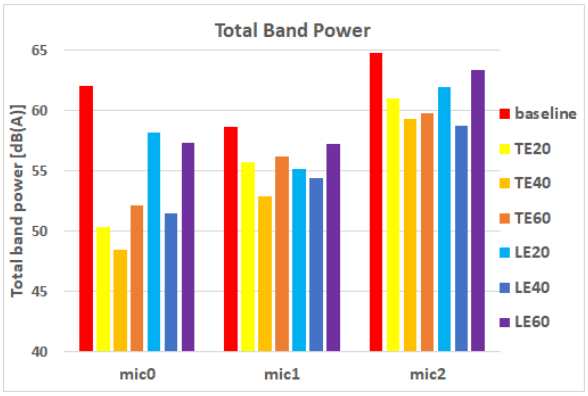

(b) 1500 RPM.

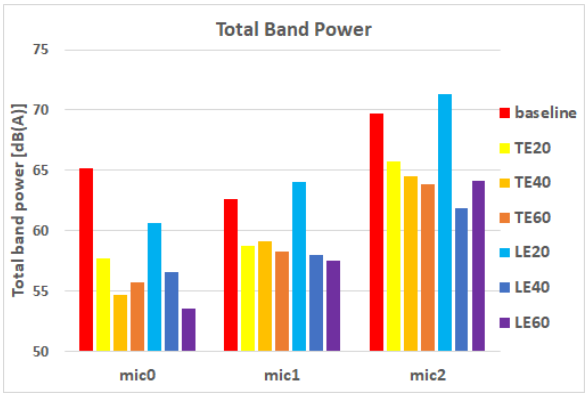

(c) 2000 RPM.

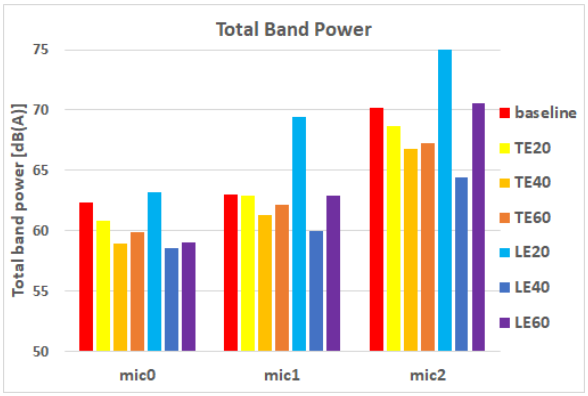

(d) 2500 RPM.

Figure A.16: Total band power measured for every rotation speed.

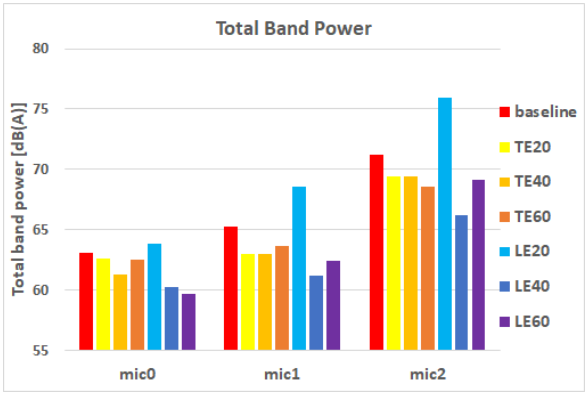

(e) 3000 RPM.

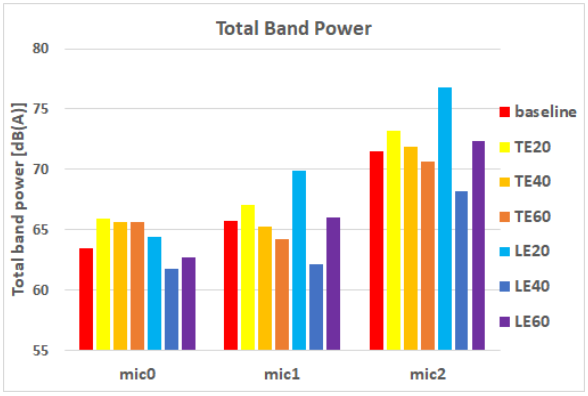

(f) 3500 RPM.

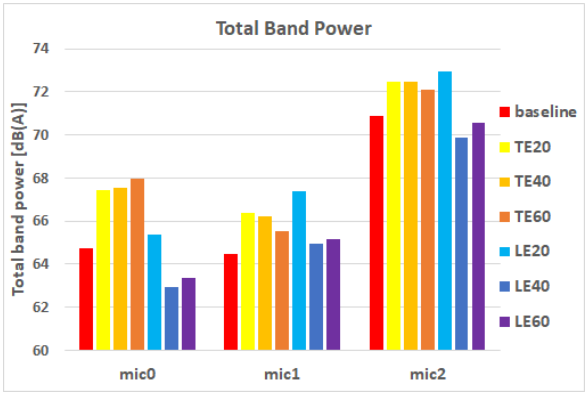

(g) 4000 RPM.

Figure A.16: Total band power measured for every rotation speed (cont.).

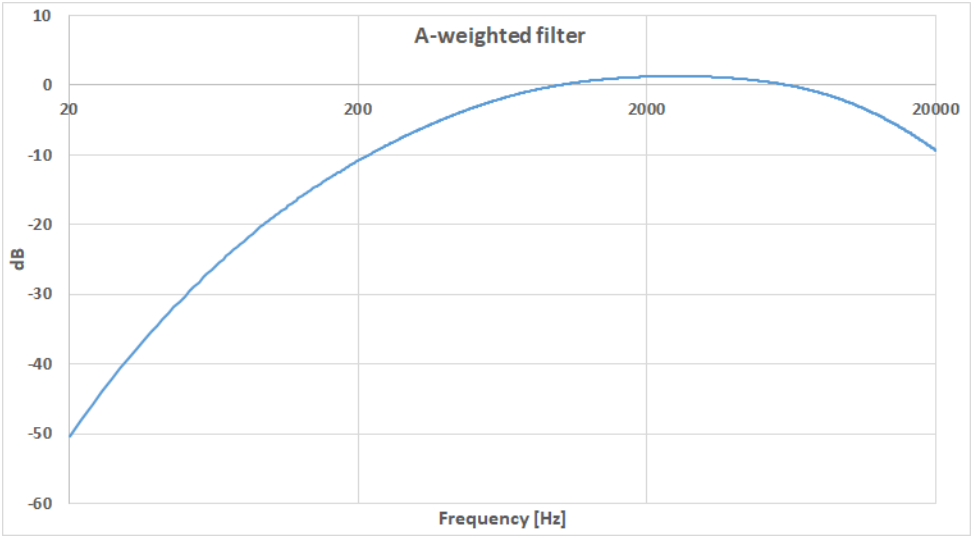

Figure A.17: The A-Weighted filter.

B

Procedure for using the Signal Conditioner

The functioning of the signal conditioner was first checked before being incorporated in the experimental setup. With the help of Professor Agostinho Fonseca, both signal conditioners available in the laboratory were tested, using an oscilloscope, a signal generator and one microphone.

The signal conditioner gets a voltage signal from the microphone and sends an amplified signal to the DAQ board. The signal conditioners used, the PCB Piezotronics 482C15 Sensor ICP, have two amplifying modes: the ICP mode and the Voltage mode. The ICP mode is the one chosen because it is the one that amplifies the microphone signal. Then, there are three different signal gains available: $\times 1$, $\times 10$ and $\times 100$. For the experiments, the gain was set to $\times 100$ for it was the setting recommended by the microphones and also it made the signal easier and clearer to be read in the LabVIEW program.

B.1 The signal from the Signal Conditioner

The signal transmitted by the signal conditioners was verified for the four channels of both signal conditioners, 1 and 2, and every channel behaved (in the sense of what was measured from the exiting signal) equally to one another, as it will now be described.

The voltage signal transmitted has two components, a continuous one and an alternating one, where the alternating signal is the one transmitted by the microphones. So, the objective is to amplify only the alternating component and to have a neglectable continuous component. When the signal conditioner is first powered on there is a voltage overflow, and the oscilloscope could only read the continuous component, with no signal from the alternating one. For gains of $\times 10$, this overflow reached voltages of $\pm 15V$, whereas for gains of $\times 100$ the values reached were up to $\pm 20V$.

After 1 minute and 12 seconds of powering the signal conditioner, the microphones signal can be detected. However, the continuous component will still be the dominant one.

After 2 minutes and 30 seconds, the continuous component has values fluctuating up to $\pm 1V$. This component is lower than $\pm 0.1V$ only after 5 minutes of having powered on the signal conditioner, with the alternating signal being clearly bigger than the continuous one.

To conclude, to use the signal conditioner, one needs to wait at least 5 minutes before taking any measurements. To be on safe side, for the experimental tests of this thesis, it was waited at least 10 to 15 minutes after powering on the signal conditioner.